



UiT The Arctic University of Norway

Faculty of Science and Technology
Department of Physics and Technology

**Novel Method for Estimating Joule Heating Rates
based on EISCAT Measurements**

Andrea Dahlmo Løkke

FYS-3931 Master's Thesis in Space Physics December 2025



Contents

List of Figures	E
List of Tables	M
1 Abstract	1
2 Introduction	5
3 Theoretical background	9
3.1 The Sun and the Near Earth Space Environment	9
3.1.1 The Sun and the Solar Wind	9
3.1.2 Earth's Magnetosphere	10
3.1.3 Earth's Ionosphere	12
3.2 Ionospheric Physics	16
3.2.1 Conductivity and Conductance	16
3.2.2 Joule Heating	20
3.3 Incoherent Scatter Radar Theory	21
3.3.1 Historical Overview and Significance	21
3.3.2 Fundamentals of Electromagnetic Scattering	22
3.3.3 ISR Spectrum and Its Interpretation	24
3.4 Machine Learning and Deep Neural Networks	25
3.4.1 Machine Learning	25
3.4.2 Multilayer Perceptrons	26
3.4.3 Loss Functions	27
3.4.4 Optimization	28
3.4.5 Regularization	29
4 Methodology	31
4.1 Datasets	31
4.1.1 The UHF Dataset	33
4.1.2 The VHF Dataset	33
4.1.3 Geophysical State Parameters	34
4.2 Exploratory Data Analysis and Preprocessing	34
4.2.1 Data Cleaning and Filtering	35

4.2.2	Data Processing	35
4.2.3	Transformation and Normalization	36
4.2.4	Data Splitting	36
4.3	Model	37
4.3.1	Model Architecture	37
4.3.2	Loss Function Development	38
4.3.3	Training and Evaluation	43
4.4	Joule Heating Prediction	43
4.4.1	Electron Density Profile Predictions	43
4.4.2	Calculation of Ionospheric Pedersen Conductance . .	43
4.4.3	Calculation of Joule Heating	45
5	Results	51
5.1	Model Selection and Training	51
5.1.1	Electron Density Prediction	52
5.2	Pedersen Conductance Comparison	55
6	Discussion	59
6.1	VHF Case Studies	59
6.1.1	Quiet Time Case Study	60
6.1.2	Stormy Time Case Study	68
6.2	Methodology Evaluation	75
6.3	Future Work	77
6.3.1	Model Explainability	77
6.3.2	Extension of framework	77
6.3.3	Extension using ESR	78
7	Conclusion	79
	Bibliography	83
A	Exploratory Data Analysis	91
A.0.1	UHF Analysis	91
A.0.2	VHF Analysis	99
A.0.3	Geo Analysis	104
A.0.4	Dataset Merging	106
B	Collision Frequency	109

List of Figures

2.1	Conceptual illustration of the power spectral density of the electric field $ E ^2$ vs. wavenumber k . The shaded regions represent the observational capabilities of different instruments, highlighting the gap in resolving high-wavenumber structures.	6
2.2	Visualization of radar beam geometries. The dark teal and light teal lines represent the pointing directions of the UHF (elevation 78°, azimuth 185°) and VHF (elevation 30°, azimuth 0°) radars, respectively. The grey hexagon indicates the EISCAT site at Ramfjordmoen [69°35' N, 19°14' E]. Dark blue dashed lines illustrate the local geomagnetic field lines.	7
3.1	A simplified visualization of the Dungey cycle, where the annotated numbers can be viewed as sequential stages in the motion for a single magnetic field line. The interplanetary magnetic field lines approach Earth from the left, and couple with the geomagnetic field at the magnetopause (1'). The resulting open field lines convect over the polar caps (2-5), before they reconnect once again on the nightside (6). Once reconnected, the closed field lines convect back to the day-side at lower latitudes (7-9), and the cycle continues. Adapted from (Russell et al., 2016) with permission from Cambridge University Press.	11
3.2	Difference in atmospheric parameters over the diurnal and 11-year solar cycle. The upper left and right plots show the electron density N_e and electron temperature T_e , respectively, and the lower left and right plots show the ion and neutral temperatures T_i and T_n , respectively. Data for solar minimum and maximum was retrieved from dates 01.01.2019 and 01.01.2014, respectively, with the day- and night time data from 12:00 and 00:00 LT. All values are obtained from the International Reference Ionosphere (IRI) model.	13
3.3	Ionospheric composition of ions, electrons and neutral constituents. Adopted from (Kelley, M.C., 1989) with the permission of Elsevier Books Limited.	14

3.4 Schematic of the ionospheric large-scale two-cell plasma convection pattern associated with the Dungey cycle. Solid arrowed lines are plasma streamlines, while the dashed line is the open-closed field line boundary. Arrows indicate ionospheric electrical fields, with X's and dots indicating the field aligned currents flowing into and out of the ionosphere, closing the current system. Hall currents flow oppositely directed to the plasma streamlines, while Pedersen currents flow along the ionospheric E-fields. The ambient geomagnetic field points into the plane. Adopted from (Cowley, 2000).	15
3.5 The figure shows a plot of the ion and electron mobility coefficients k_i and k_e above EISCAT Ramfjordmoen January 21st 2012 10:24 UT. The orange dashed line indicates where the mobility coefficient k becomes 1. The magnetic field data was obtained from the IGRF model using the Github repository ppigrf (Laundal, 2025). Neutral and ion constituents are obtained from NRLMSISE-00 (Picone et al., 2002) and IRI model (Ilma, 2024), respectively.	17
3.6 The plot shows the coefficients contributing to ion drift parallel to ionospheric E -fields (blue) and in the direction orthogonal to E - and B -fields (orange) for ions (solid) and electrons (dashed).	18
3.7 Plots showing multiple configurations of the ion line. The left plot visualizes transition of the ion line ISR spectrum for different temperature ratios T_e/T_i . The right plot shows how the ion line (using $T_e/T_i = 1.5$) is Doppler shifted in frequency domain due to ion velocity. Here we consider only O^+ -ions and electrons as the constituent particles, with $N_e = 2 \times 10^{11} m^{-3}$, $T_i = 1000K$ and a radar frequency $f_R = 930$ MHz, similar to that of the EISCAT UHF. The figure was made using supervisor Juha Vierinen's Github repository isr_spec (Vierinen, 2025).	24
3.8 Schematic of a single neuron's architecture. The input features, x_1 and x_2 , are multiplied by their corresponding weights, w_1 and w_2 , and added to the bias term b to form the weighted sum Σ . This sum is passed through an activation function σ to generate the neuron's final output.	27
3.9 Visualization of a 3D loss surface. Adapted from Li et al. (2018).	28
3.10 Schematic showing idealized training (orange) and validation (green) loss curves. The dashed pink line indicates the epoch at which the validation loss reaches its minimum.	30

4.1 Schematic of EISCAT radar scan patterns CP1 through CP6. L and T denote the EISCAT radar sites near Longyearbyen and Tromsø, respectively. The blue and orange frames indicate the scan patterns associated with the UHF and VHF datasets used in this thesis, respectively. Figure adapted from (Tjulin, 2025).	32
4.2 Schematic of the Fully Connected Neural Network (FCNN) architecture. The input vector (left), derived from plasma parameters at a single altitude i combined with geophysical indices, is mapped to a complete predicted electron density profile \hat{N}_e (right). The network comprises three hidden layers (ℓ_1, ℓ_2, ℓ_3), each utilizing Batch Normalization (BN), ReLU activation, and Dropout (DO).	37
4.3 The figure shows random samples of electron density profiles, from no filtering on the upper left, to increasing temporal median filtering kernel $k \in [3, 5, 7]$, respectively.	39
4.4 The figure shows random samples of electron density profiles, from no smoothing on the upper left, with increasing smoothing parameters towards right.	40
4.5 Comparison of raw UHF electron density profiles (teal) and the reconstructed profiles from the Autoencoder (orange).	42
4.6 Comparative plot illustrating the variation in atmospheric and ionospheric parameters between Tromsø (solid lines) and Svalbard (dashed lines) latitudes. The upper left plot shows IRI ion, electron and neutral temperatures T_n , T_e and T_i , the upper right shows MSIS neutral constituent densities n_O , n_{O_2} and n_{N_2} , the lower left show IRI ion constituent densities n_{O^+} , $n_{O_2^+}$ and n_{NO^+} (scaled by N_e), and, finally, the lower right shows IGRF magnetic field flux density $ B $. Note that $n_{N_2^+}$ is not included in the lower left plot as its density is negligible.	44

4.7	The figure shows plots in relation to conductivity calculations. The upper left plot shows the difference between the Pedersen conductivity σ_P with and without electron contribution. The upper right plot shows the comparison of the total electron-neutral and ion-neutral collision frequencies ν_e and ν_i , respectively. The second row shows the electron contribution, with the plot on the left being a neural network smoothed electron density N_e profile. The plot on the right shows a comparison of the electron-neutral collision frequencies ν_{en} compared to the electron gyrofrequency ω_{ce} . The lower row shows the ion contribution, with the leftmost plot showing the ion density profiles for O^+ , O_2^+ and NO^+ . The rightmost plot shows the comparison of ion-neutral collision frequencies ν_{in} and ion gyrofrequencies ω_{ci} . Note that the conductivity is maximised where the ion gyro- and collision frequency coincide. Also note that the largest discrepancy in the upper left plot occurs when electron-neutral collision frequencies and electron gyrofrequency are similar in magnitude.	46
4.8	Schematic of how the radar measures the ion velocity, with the pink dot as the radar site. The grey arrowed line indicates the geomagnetic field \mathbf{B} , the green arrow is the ion velocity vector \mathbf{V}_i , the yellow arrow is the Bragg vector \mathbf{k}_B , and θ is the angle between the two. The two blue dashed lines indicate the volume and radar vector from the center of the Earth, denoted \mathbf{r}_v and \mathbf{r}_R , respectively.	47
5.1	Training (blue) and validation (orange) loss curves for the model configuration with $\alpha = 50$ and $p = 0.20$. The model was trained for 50 epochs, but reached its minimum at epoch 32. The remaining 18 epochs are not shown.	52
5.3	Field aligned profile of the WMSE (computed with $\beta = 1$) calculated over the test set. The model shows highest accuracy in the F-region (150-500 km), and reduced performance in the low-altitude E-region and high-altitude topside ionosphere.	53
5.2	Comparison of the measured (blue) and predicted (orange) electron density profiles. The grey scatter point on each plot indicates the single electron density point that the model is fed during prediction.	54
5.4	Histogram of Pedersen conductance Σ_P computed using FCNN-predicted profiles (dark blue), raw ISR ground truth profiles (orange), and Autoencoder-smoothed electron density profiles (light blue).	55

5.5 Correlation plots of conductances computed using FCNN predicted, autoencoder smoothed and ground truth electron density profiles. From left to right, the plots show the correlation of the FCNN and the ground truth, the FCNN and the autoencoder, and the ground truth and autoencoder. The light orange line is the linear fit of the correlation scatter plot. Vertical structures can be seen in the center and leftmost plot. This is caused by our label architecture, as each label is used 42 times.	57
6.1 Overview of the quiet time case study (January 24–25, 2017). Panel 1–4: Measured Electron Density N_e and Temperature T_e , Ion Temperature T_i and LOS Velocity V_{LOS} from the EISCAT VHF radar. Panel 5: Field-Line Integrated Electron Density \hat{N}_e predicted by the FCNN. Panel 6: Derived Field-Line Integrated Pedersen Conductance Σ_P . Panel 7: Lower Bound Biased Joule Heating Rate Q_L . Panel 8: Standard Deviation of the ion LOS velocity measurement $\sigma_{V_{\text{LOS}}}$. Panel 9: Lower Bound Joule Heating Rate Q_{UL} calculated using $\beta = 30$. Note that for panels 5–9, the y-axis represents the altitude, and corresponding latitude, of the <i>input</i> measurement along the oblique VHF beam.	61
6.2 Cross-section of the ionosphere at 02:32:29 UT. The panels display from top to bottom: Predicted Electron Density Profiles \hat{N}_e , Pedersen Conductivity σ_P , Lower Bound Biased Joule Heating Rate q_L , and Lower Bound Unbiased Joule Heating Rate q_{UL} . The white scatter points indicate the altitude and Magnetic Latitude (MLAT) of the input VHF measurements used to generate each field-aligned profile. The blue line overlay on the bottom two plots represents the estimated perpendicular lower bound electric field magnitude $ E'_{\perp L} $. Laundal et al. (2024)'s dipole Github package was used for the computation of MLAT.	64
6.3 Polar projection of the mean Pedersen conductance Σ_P as a function of Magnetic Local Time (MLT) and Magnetic Latitude (MLAT). The color scale indicates the conductance. The greyshaded area bounded by the grey line indicates the temporal variation within each MLT bin. Numerical bounds are indicated on the top left.	65

6.4	Polar projection of the mean lower bound Joule heating rate Q_L as a function of Magnetic Local Time (MLT) and Magnetic Latitude (MLAT). The color scale indicates the heating rate. The greyshaded area bounded by the grey line indicates the temporal variation within each MLT bin. Numerical bounds are indicated on the top left.	67
6.5	Polar projection of the mean unbiased lower bound Joule heating rate Q_{UL} as a function of Magnetic Local Time (MLT) and Magnetic Latitude (MLAT). The color scale indicates the heating rate. The greyshaded area bounded by the grey line indicates the temporal variation within each MLT bin. Numerical bounds are indicated on the top left.	68
6.6	Overview of the stormy time case study (September 7–8, 2017). Panel 1–4: Measured Electron Density N_e and Temperature T_e , Ion Temperature T_i and LOS Velocity V_{LOS} from the EISCAT VHF radar. Panel 5: Field-Line Integrated Electron Density \hat{N}_e predicted by the FCNN. Panel 6: Derived Field-Line Integrated Pedersen Conductance Σ_P . Panel 7: Lower Bound Biased Joule Heating Rate Q_L . Panel 8: Standard Deviation of the ion LOS velocity measurement $\sigma_{V_{\text{LOS}}}$. Panel 9: Lower Bound Joule Heating Rate Q_{UL} calculated using $\beta = 30$. Note that for panels 5–9, the y-axis represents the altitude, and corresponding latitude, of the <i>input</i> measurement along the oblique VHF beam.	70
6.7	Cross-section of the ionosphere at 22:41:29 UT. The panels display from top to bottom: Predicted Electron Density Profiles \hat{N}_e , Pedersen Conductivity σ_P , Lower Bound Biased Joule Heating Rate q_L , and Lower Bound Unbiased Joule Heating Rate q_{UL} . The white scatter points indicate the altitude and Magnetic Latitude (MLAT) of the input VHF measurements used to generate each field-aligned profile. The blue line overlay on the bottom two plots represents the estimated perpendicular lower bound electric field magnitude $ E'_{\perp L} $. Laundal et al. (2024)'s dipole Github package was used for the computation of MLATs.	71
6.8	Polar projection of the mean Pedersen conductance Σ_P as a function of Magnetic Local Time (MLT) and Magnetic Latitude (MLAT). The color scale indicates the conductance. The greyshaded area bounded by the grey line indicates the temporal variation within each MLT bin. Numerical bounds are indicated on the top left.	73

6.9	Polar projection of the mean lower bound Joule heating rate Q_L as a function of Magnetic Local Time (MLT) and Magnetic Latitude (MLAT). The color scale indicates the heating rate. The greyshaded area bounded by the grey line indicates the temporal variation within each MLT bin. Numerical bounds are indicated on the top left.	74
6.10	Polar projection of the mean unbiased lower bound Joule heating rate Q_{UL} as a function of Magnetic Local Time (MLT) and Magnetic Latitude (MLAT). The color scale indicates the heating rate. The greyshaded area bounded by the grey line indicates the temporal variation within each MLT bin. Numerical bounds are indicated on the top left.	75
A.1	Scatterplot visualizing the timeline of available ISR data and the number of range gates (profile length) per measurement.	92
A.2	Distribution of altitude counts (profile lengths) per timestamp. The x-axis represents the number of range gates in a single measurement, while the y-axis shows the frequency of such occurrences.	93
A.3	Scatterplot showing the mean and standard deviation of altitude for each of the 42 range gates in the standard ISR profile.	94
A.4	Timeline of ISR data availability showing the number of individual profiles per day. The orange line indicates 1440 samples, the theoretical maximum for 1-minute resolution data in a 24-hour period. Note the absence of data from the <i>beata</i> program prior to 2007.	95
A.5	Heatmap visualizing data availability per Day of Year (DOY) over the period 2007-2024.	96
A.6	Heatmap visualizing data availability per Time of Day (TOD) over the period 2007-2024.	96
A.7	Distribution of radar azimuth angles. Values are binned into 50 intervals, with the top 5 bins annotated.	97
A.8	Distribution of radar elevation angles. Values are binned into 50 intervals, with the top 5 bins annotated.	97
A.9	Scatterplot showing the secular variation of magnetic azimuth and zenith angles for EISCAT Ramfjordmoen at 300 km altitude, 2007-2024.	98
A.10	Heatmap displaying the frequency of NaN values in N_e , T_e , and T_i as a function of time of day and altitude.	99
A.11	Distribution of ISR parameters NE, TE and TI.	100
A.12	Standard deviation distribution of ISR parameters NE, TE and TI.	100
A.13	Scatterplot visualizing the timeline of available VHF data and the profile length per measurement.	101

A.14 Distribution of altitude counts for VHF measurements.	102
A.15 Mean and standard deviation of altitude for each of the 39 range gates in the standard VHF profile.	102
A.16 Distribution of VHF radar azimuth (blue, left axis) and elevation (orange, right axis) angles.	103
A.17 Heatmap of NaN-value frequency for VHF parameters (N_e , T_e , T_i , V_{LOS}) vs. Hour of Day and Binned Altitude.	104
A.18 Plot of the time series of the geophysical parameters. From top to bottom: AE , AL , SYM/H , PCN , A_p and $F10.7$ indices.	105
A.19 Distribution of the geophysical parameters, with mean, median and standard deviation.	106
A.20 Correlation heatmap of the input features in the merged dataset.	107

List of Tables

4.1	Train, test and validation dataset split by year.	36
4.2	Parameter breakdown for the FCNN architecture.	38
B.1	Ion-neutral collision frequency coefficients C_{in} , in units of $10^{-10} \text{ cm}^3 \text{ s}^{-1}$, for ions O^+ , O_2^+ , N_2^+ and NO^+ . R indicates resonant interaction. Coefficients obtained from table 4.4 in (Schunk and Nagy, 2009a).	109
B.2	Resonant ion-neutral momentum transfer collision frequencies ν_{in} for ions O^+ , O_2^+ , N_2^+ and NO^+ . Densities are in cm^{-3} . Reduced temperature $T_r = \frac{T_i + T_n}{2}$. Expressions obtained from table 4.5 in (Schunk and Nagy, 2009a).	110
B.3	Momentum transfer collision frequencies ν_{en} for electron-neutral interactions. Densities are in cm^{-3} . Expressions obtained from table 4.6 in (Schunk and Nagy, 2009a).	110



1

Abstract

High-latitude ionospheric Joule heating poses a major challenge to the operation of satellites in low-Earth orbit. Heating events drive the vertical expansion of the neutral atmosphere, effectively increasing atmospheric drag on satellites. Accurate estimation of this energy dissipation requires knowledge about ionospheric electric fields and Pedersen conductance. However, current observational infrastructure is limited, forcing a trade-off between wide spatial coverage and the vertical resolution needed to calculate the conductance. This thesis addresses these limitations by constructing a Deep Learning framework capable of predicting field-aligned electron density profiles from sparse Incoherent Scatter Radar (ISR) data.

By leveraging the physical property that magnetic field lines act as electric equipotentials, we hypothesize that the local plasma parameters measured at a single altitude, supplemented by global geophysical indices, contain sufficient information to reconstruct the entire field-aligned profile. A Fully Connected Neural Network was trained on a curated dataset of field-aligned EISCAT Ultra High Frequency UHF measurements from the time interval 2007–2024. The model utilizes local plasma parameters electron density N_e , electron T_e and ion T_i temperature along with global geophysical indices to predict full field-aligned electron density profiles.

Validation against unseen test data demonstrates that the model accurately reproduces the altitude distribution of electron density, resolving dynamic behaviour that statistical models, such as Hardy et al. (1987), fail to capture. The

model is then applied to oblique EISCAT Very High Frequency (VHF) data to predict electron density profiles and subsequently infer field line integrated Pedersen conductance at each point of measurement. This further enables the estimation of high-resolution lower bound Joule heating rates. The results indicate that this data-driven approach is capable of constructing a mapping from local plasma and global geophysical parameters to the full field-aligned electron density profile. This approach offers a novel method of estimating Joule heating rates with high spatial and temporal resolution, which improves the current state of knowledge in energy coupling of the high-latitude atmosphere.

Acknowledgments

My deepest gratitude goes to my supervisors Juha Vierinen, Andreas Kvammen, Andres Spicher, and Kristoffer Wickstrøm. Together, you have facilitated an environment where I have been able to explore our collective ideas. You have provided insights and knowledge I'd otherwise would have remained ignorant to, significantly improving the final outcome of this thesis. I am immensely grateful to your support. Thank you.

To my friends at the Space Physics Group, especially Etienne. I don't think I've ever had as productive procrastination sessions in my life as the ones we've shared. You've changed my life for the better.

To my friend Oda. Thank you for your support over the last five years. I am so grateful to our friendship. I hope our paths intertwine in the future.

To my late Hauke and Bestemor. Every auroral display I watch reminds me of you. I wish you were here.

To my mom Kristin and sister Lise. The relationship and history we share is invaluable to me. I cannot express my gratitude towards you enough. You are the pillars of my life.

To my Håkon. Thank you for your everlasting support and the life we share. I cannot imagine my life without you.

Finally, a warm thought goes to the greek letter σ , which, throughout this thesis, has sustained a great amount of notational abuse.

/2

Introduction

The exponential increase in satellite launches and near-Earth space activity in recent years necessitates precise characterization of the physical processes governing the upper atmosphere, particularly ionospheric Joule heating (European Space Agency, 2025). Joule heating is the dissipation of electromagnetic energy into thermal energy, a process that drives the vertical expansion of the neutral atmosphere and increases particle density at low-Earth orbit altitudes (Tenfjord and Østgaard, 2013; Koskinen and Tanskanen, 2002; Bates, 1974). The risks posed by this phenomenon were starkly demonstrated in February 2022, when a geomagnetic storm induced atmospheric drag sufficient to deorbit 38 of 49 newly launched SpaceX satellites (Fang et al., 2022).

Joule heating rates (Q) are locally defined as the product of the Pedersen conductance (Σ_P) and the square of the electric field magnitude ($|E|^2$), given by $Q = \Sigma_P |E|^2$ (Zhu et al., 2005). While conductance is conventionally defined as the vertical height integral of ionospheric Pedersen conductivity σ_P (Brekke, 2012), this thesis calculates σ_P integrated along geomagnetic field lines. This approach is motivated by the electrodynamics of the high-latitude ionosphere, where magnetic field lines are often approximated as electric equipotentials due to high parallel conductivity (Kelley, M.C., 1989; Brekke, 2012). As a consequence, plasma dynamics and parameters are far more strongly correlated along the magnetic field lines than along a strictly vertical profile. At the EISCAT Ramfjordmoen site, the geomagnetic field is inclined approximately 12° off zenith. Accounting for this geometry is essential, as the field-aligned perspective provides a more physically consistent basis for modeling than a

vertical column.

Despite the critical importance of this quantity, Joule heating rates remain poorly specified due to fundamental measurement limitations. Figure 2.1 illustrates the power spectral density of $|E|^2$ as a function of wavenumber k . Standard observation instruments, such as SuperDARN or ground-based magnetometers, are generally restricted to capturing low-frequency, large-scale phenomena (indicated in green). Thus, they often miss the high-wavenumber contributions, i.e., the orange part of the spectrum, that can dominate localized heating events. In contrast, Incoherent Scatter Radars (ISR) offer high spatial resolution capable of resolving high-wavenumber contributions (indicated in orange), alongside the low-frequency components. However, ISRs are typically limited to narrow-beam geometries and lack wide spatial coverage. This measurement gap is critical; by failing to resolve the high-frequency portion of the spectrum, standard instrumentation systematically misses significant energy contributions entering the atmospheric system, leading to underestimations of total heating (Palmroth et al., 2021).

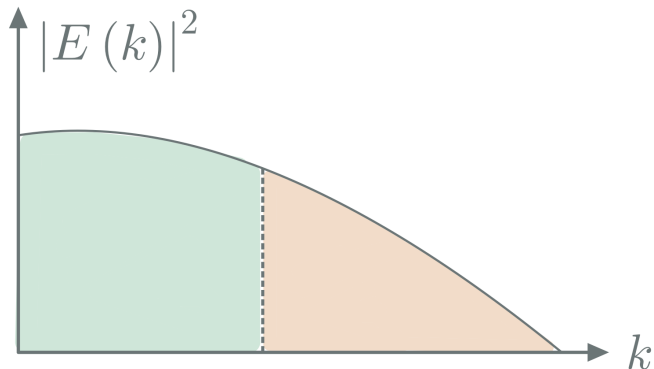


Figure 2.1: Conceptual illustration of the power spectral density of the electric field $|E|^2$ vs. wavenumber k . The shaded regions represent the observational capabilities of different instruments, highlighting the gap in resolving high-wavenumber structures.

The work of this thesis aims to bridge the gap between high-resolution point measurements and broad spatial coverage. While the upcoming EISCAT_3D system will eventually provide volumetric imaging of the ionosphere, current limitations require alternative approaches to infer field aligned structures from sparse data. A promising solution lies in Deep Learning. Recent work by Sartipzadeh et al. (2025) has demonstrated that Deep Neural Networks (DNNs) can effectively model complex ionospheric relationships, performing with high efficacy even during dynamic auroral precipitation events.

In this thesis, we employ a DNN as the analytical framework to reconstruct the missing field aligned dimension in radar scans. We utilize data from the EISCAT Ultra High Frequency (UHF) and Very High Frequency (VHF) radars. The EISCAT VHF radar provides valuable latitudinal coverage (see Figure 2.2), but because its beam intersects magnetic field lines at an angle, it lacks a complete altitude profile for any given field line. To solve this, we design a model trained on field-aligned UHF data to predict a complete field-aligned electron density profile based on input parameters from a single altitude and global geophysical indices. This strategy exploits the equipotential nature of the field lines to "fill in" the vertical plasma structure along the VHF beam path, effectively creating a 2D slice of the ionosphere.

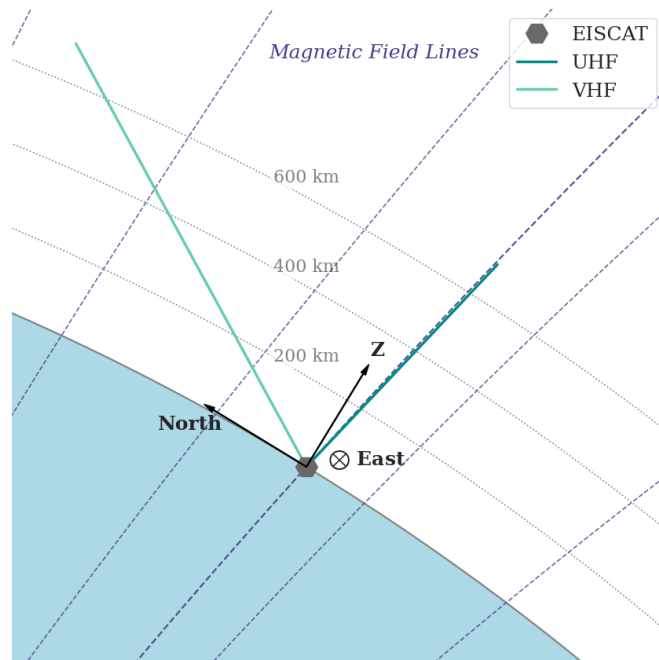


Figure 2.2: Visualization of radar beam geometries. The dark teal and light teal lines represent the pointing directions of the UHF (elevation 78° , azimuth 185°) and VHF (elevation 30° , azimuth 0°) radars, respectively. The grey hexagon indicates the EISCAT site at Ramfjordmoen [$69^\circ 35' \text{N}$, $19^\circ 14' \text{E}$]. Dark blue dashed lines illustrate the local geomagnetic field lines.

The specific goals of this thesis project are to:

1. Describe the scientific rationale for creating an ionospheric model capable of estimating magnetic field-aligned electron density profiles, emphasizing the physical correlation of parameters along equipotential field lines.

2. Establish whether the complex non-linear relationship between ionospheric plasma parameters, geophysical indices, and field-aligned electron density profiles can be effectively modeled by a deep neural network.
3. Evaluate the performance of the proposed Deep Learning model by comparing its conductance estimates against ground truth EISCAT UHF field-aligned measurements and the statistical model provided by Hardy et al. (1987).
4. Compute conductivity estimates based on predicted electron density profiles from EISCAT VHF data.
5. Estimate Joule heating rates from EISCAT VHF using the derived conductances.
6. Discuss the potential applications and limitations of the model.

We hypothesize that the Deep Learning model developed in this thesis will outperform existing empirical models, such as Hardy et al. (1987). By leveraging instantaneous spatial information and the strong physical correlation along magnetic field lines, our model aims to capture dynamic variations that statistical averages fail to resolve.

Thesis Structure

The thesis is organized into seven chapters. **Chapter 3** establishes the theoretical foundation, encompassing the relevant solar-terrestrial physics, the principles of ISRs, and the fundamentals of Deep Neural Networks. **Chapter 4** details the methodology, including the curation of EISCAT data, the preprocessing pipeline, and the specific architecture of the neural network, followed by the derivation of Joule heating rates. **Chapter 5** presents the validation results, evaluating the model's accuracy in predicting electron density profiles and Pedersen conductance against ground truth measurements. **Chapter 6** discusses the broader implications of the model through specific case studies applied to EISCAT VHF data, alongside a critical evaluation of the methodology and suggestions for future work. Finally, **Chapter 7** summarizes the main findings and concludes the thesis.

/3

Theoretical background

This chapter establishes the theoretical foundation for the thesis, beginning with the dynamic relationship between the Sun and Earth. We describe the magnetosphere-ionosphere system, emphasizing the electromagnetic coupling between them. We then discuss ionospheric conductivity, explaining how this property facilitates the dissipation of energy via Joule heating. Furthermore, we outline the ISR theory used to observe these phenomena. Finally, we introduce the fundamental concepts of machine learning and deep neural networks, which serve as the analytical framework for this work.

3.1 The Sun and the Near Earth Space Environment

3.1.1 The Sun and the Solar Wind

At the center of our Solar System lies the Sun, a massive sphere of energetic, radiating plasma (Lissauer, J. and de Pater, I., 2019). The Sun generates energy through thermonuclear fusion of hydrogen in its core, a process sustained by the immense pressure from its own gravity (Lissauer, J. and de Pater, I., 2019). This energy is transported to the surface, where it is emitted as electromagnetic radiation. The Sun's differential rotation causes its magnetic field lines to become twisted, distorting the overall heliomagnetic field (Howe,

2009; Fraknoi et al., 2022). This dynamo process drives the growth and decay of the magnetic field with alternating polarity over a period of approximately 11 years, known as the *solar cycle*. The emission of electromagnetic energy from the Sun depends heavily on this cycle, which is characterized by periods of high activity (solar maximum) and low activity (solar minimum) (Lissauer, J. and de Pater, I., 2019).

Beyond electromagnetic radiation, the Sun also emits streams of hot plasma known as the solar wind. This wind consists primarily of fully ionized hydrogen and helium, ejected from the solar corona with varying speeds and densities (Brekke, 2012). According to Alfvén's *frozen-in theorem*, magnetic flux is conserved in a perfectly conducting fluid (Alfvén, 1958). Although the solar wind plasma is not a perfect conductor, it is highly conductive (Weber and Davis Jr, 1967) and therefore effectively conserves its magnetic flux. Consequently, the solar wind carries the magnetic field of the solar region from which the plasma was ejected (Alfvén, 1958), forming what is known as the *Interplanetary Magnetic Field* (IMF). We denote this vector as \mathbf{B}_{IMF} , given in units of Tesla (T). Throughout this work, components of the IMF are given in the Geocentric Solar Magnetospheric (GSM) coordinate system (Russell, 1971), as this frame best organizes the magnetospheric response.

Driven radially outward, the solar wind impinges upon the planetary bodies of our solar system, transporting and depositing both mechanical and electromagnetic energy into these environments (Lissauer, J. and de Pater, I., 2019). For Earth specifically, the interaction between this magnetized plasma flow and the geomagnetic field forms the complex and dynamic cavity known as the magnetosphere (Kivelson and Bagenal, 2007).

3.1.2 Earth's Magnetosphere

The terrestrial magnetosphere is the region of space where the Earth's magnetic field dominates over the IMF, governing the motion of charged particles (Kivelson and Bagenal, 2007). Within ~ 6 Earth radii, R_E , the geomagnetic field can be approximated as a tilted dipole with its magnetic poles located near Earth's geographic poles (Brekke, 2012). At larger distances, however, the structure is highly distorted by the continuous flow of the solar wind. The dynamic pressure of the impinging solar wind is balanced by the magnetic pressure of the geomagnetic field at a boundary known as the *magnetopause* (Brekke, 2012). This interaction compresses the magnetic field on the sunward side while stretching the magnetosphere in the anti-sunward direction, forming a long magnetotail that extends hundreds of R_E (Kivelson and Bagenal, 2007).

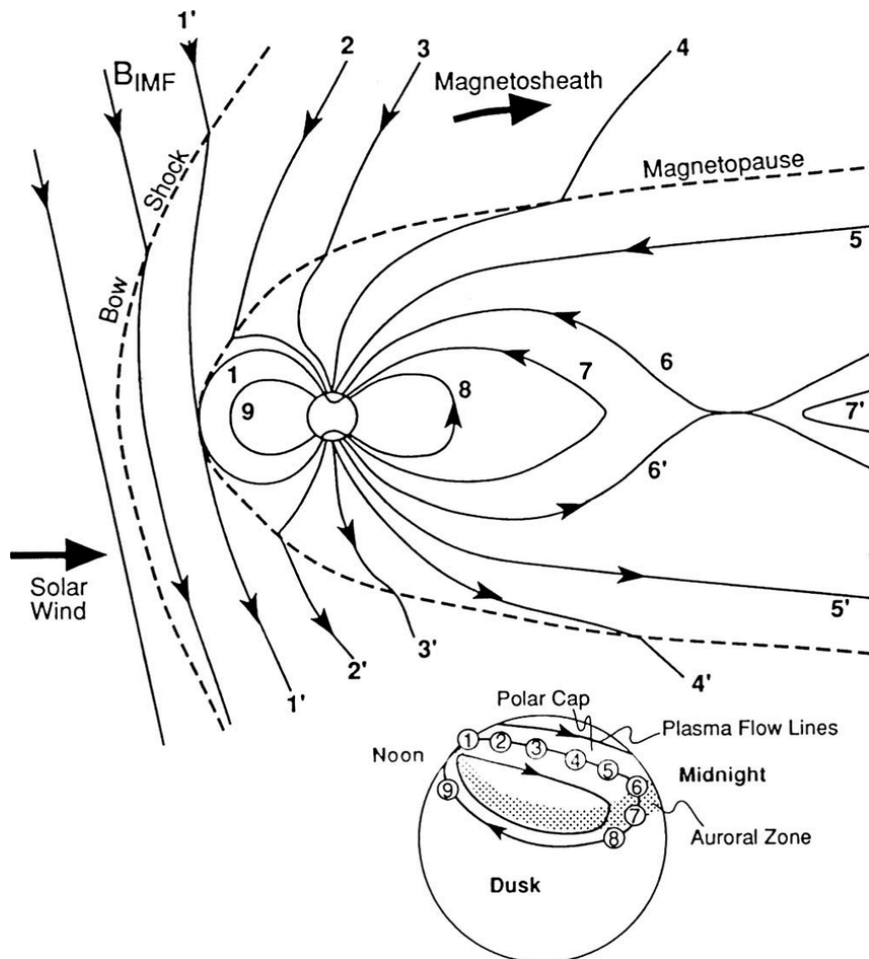


Figure 3.1: A simplified visualization of the Dungey cycle, where the annotated numbers can be viewed as sequential stages in the motion for a single magnetic field line. The interplanetary magnetic field lines approach Earth from the left, and couple with the geomagnetic field at the magnetopause (1'). The resulting open field lines convect over the polar caps (2-5), before they reconnect once again on the nightside (6). Once reconnected, the closed field lines convect back to the dayside at lower latitudes (7-9), and the cycle continues. Adapted from (Russell et al., 2016) with permission from Cambridge University Press.

The degree of coupling between the solar wind and the geomagnetic field is critically dependent on the orientation of the IMF, specifically its B_z component (Cowley, 2000). Under southward IMF conditions ($B_z < 0$ T), magnetic reconnection occurs on the dayside, coupling the interplanetary and terrestrial fields. This process drives the transfer of mass, momentum, and energy into the system. However, the magnetosphere remains a highly effective obstacle; the *coupling efficiency*, i.e., the ratio of energy entering the magnetosphere to the

incident solar wind kinetic energy, is estimated to be only $\sim 0.4\%$ (Tenfjord and Østgaard, 2013). The *Dungey cycle* conceptualizes this magnetic reconnection and the circulation of magnetic flux and plasma in the magnetosphere (Dungey, 1961).

Figure 3.1 shows a simplified visualization of the Dungey cycle, where the annotated numbers can be viewed as sequential stages in the motion for a single magnetic field line. The interplanetary magnetic field lines approach Earth from the left, and couple with the geomagnetic field at the magnetopause (1'). The resulting open field lines convect over the polar caps (2-5), before they reconnect once again on the nightside (6). Once reconnected, the closed field lines convect back to the dayside at lower latitudes (7-9), and the cycle continues.

The lower part of Figure 3.1 displays resulting plasma flow in the ionosphere. This motion is governed by the previously mentioned frozen-in theorem; as the field lines convect, they drag the ionospheric plasma with them (Kivelson and Bagenal, 2007). In the following section, we introduce the ionosphere and its properties, before discussing how this global convection cycle impacts the ionospheric medium.

3.1.3 Earth's Ionosphere

The ionosphere is a region of partially ionized plasma surrounding the Earth. It is formed by the ionization of neutral atmospheric constituents through solar photoionization, energetic particle precipitation and galactic cosmic rays (Brekke, 2012). Although the medium satisfies the condition of quasi-neutrality on macroscopic scales, i.e., electron density equals ion density ($N_e = N_i$), it exhibits local fluctuations and irregularities in charge density (Kelley, M.C., 1989). Consequently, the ionosphere behaves as a dynamic, conducting fluid, where electric fields imposed by the magnetosphere drive plasma currents through the resistive atmosphere (Cowley, 2000). The spatial extent of the ionosphere is variable; its upper boundary transitions gradually into the plasmasphere at altitudes exceeding 1000 km, while the significant decrease in ionization below approximately 60 km defines the lower boundary (Brekke, 2012).

The vertical structure of the ionosphere is divided into several distinct regions (Brekke, 2012). The first to be identified was the E-layer, discovered in the early 1920s by Sir Edward Appleton and his Ph.D. student M.A.F. Barnett (Appleton and Barnett, 1925). They confirmed its existence by observing the "downward atmospheric reflection of electric rays" (Appleton and Barnett, 1925; Brekke, 2012), a discovery that established the conducting nature of the upper atmosphere. Subsequent identification of additional layers prompted an alphabetical nam-

ing convention, resulting in the D- and F-layers (the latter comprising F1 and F2), situated below and above the E-layer, respectively (Brekke, 2012). Although commonly referred to as layers, there are no sharp discontinuities or distinct stratifications separating them. Instead, this terminology serves to classify altitude regions that exhibit similar physical and chemical properties.

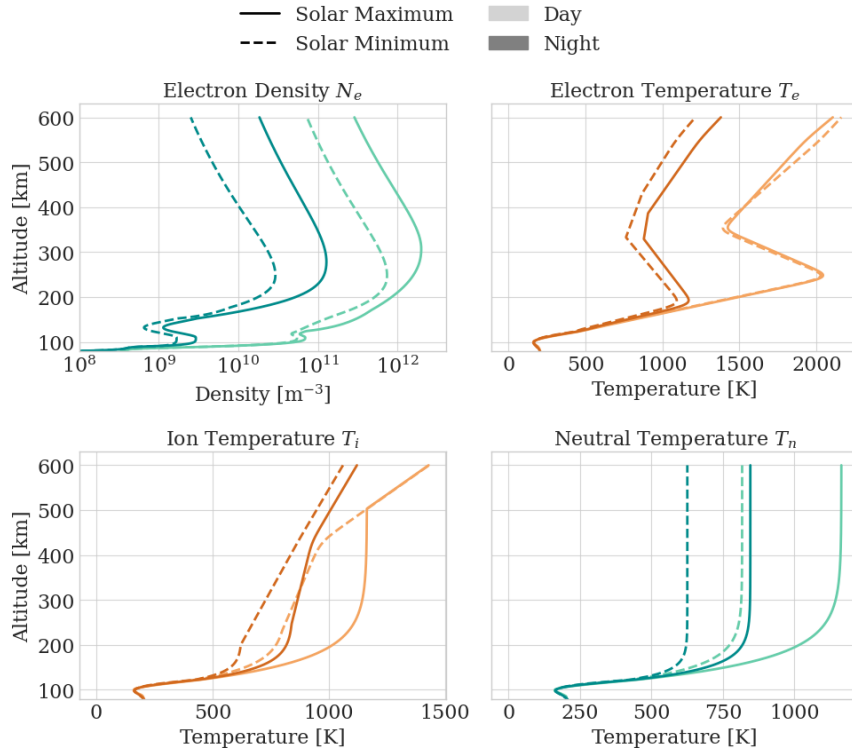


Figure 3.2: Difference in atmospheric parameters over the diurnal and 11-year solar cycle. The upper left and right plots show the electron density N_e and electron temperature T_e , respectively, and the lower left and right plots show the ion and neutral temperatures T_i and T_n , respectively. Data for solar minimum and maximum was retrieved from dates 01.01.2019 and 01.01.2014, respectively, with the day- and night time data from 12:00 and 00:00 LT. All values are obtained from the International Reference Ionosphere (IRI) model.

The D-layer is generally defined as the region between 60 and 90 km altitude (Brekke, 2012). While it possesses a relatively low plasma density, it is highly variable. High-energy phenomena, such as electron precipitation from auroral activity, solar flare X-ray bursts, and other sporadic ionization events, can drive significant increases in D-region plasma density (Kero, 2008; Brekke, 2012). Above this, spanning 90–150 km, lies the E-layer, which contains significantly higher plasma densities than the D-region while maintaining large variability

(Brekke, 2012). Finally, the highest ionospheric plasma densities are found in the F-region, which extends from 150 km up to approximately 500 km altitude (Brekke, 2012).

During Earth's diurnal cycle, plasma densities in the D-, E- and F-layers vary in direct response to the rate of local photoionization (Brekke, 2012). During nighttime, in the absence of solar radiation, the plasma density of the D- and E-regions diminishes rapidly due to recombination of free ions and electrons. In contrast, the F-region retains a significant amount of its plasma throughout the night.

Figure 3.2 visualizes the diurnal variation in electron density as well as electron (T_e), ion (T_i) and neutral (T_n) temperature. The daytime and nighttime profiles are represented by the light and dark lines, respectively. The solar cycle variation is distinguished by line style, where solid lines represent solar maximum and dashed lines represent solar minimum. In this specific example, the daytime electron density exceeds the nighttime density by more than an order of magnitude.

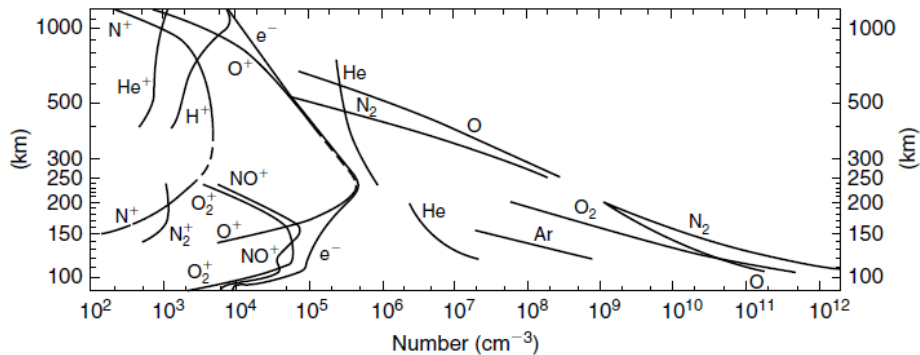


Figure 3.3: Ionospheric composition of ions, electrons and neutral constituents.
Adopted from (Kelley, M.C., 1989) with the permission of Elsevier Books Limited.

The physical mechanism driving this disparity is linked to the ion composition. Figure 3.3 illustrates that the D- and E-regions are dominated by molecular ions, such as NO^+ and O_2^+ , whereas atomic oxygen, O^+ , becomes the primary constituent at F-region altitudes. This distinction is critical because the recombination rates of molecular ions exceed those of atomic ions by approximately three orders of magnitude (Brekke, 2012). Consequently, once the photoionization source is removed at sunset, the lower ionosphere is quickly depleted, whereas the F-region plasma decays much more slowly. Additionally, the solar cycle exerts a major influence on these densities, as solar activity modulates

the intensity of ionizing radiation, resulting in the overall enhancement of atmospheric parameters observed during solar maximum.

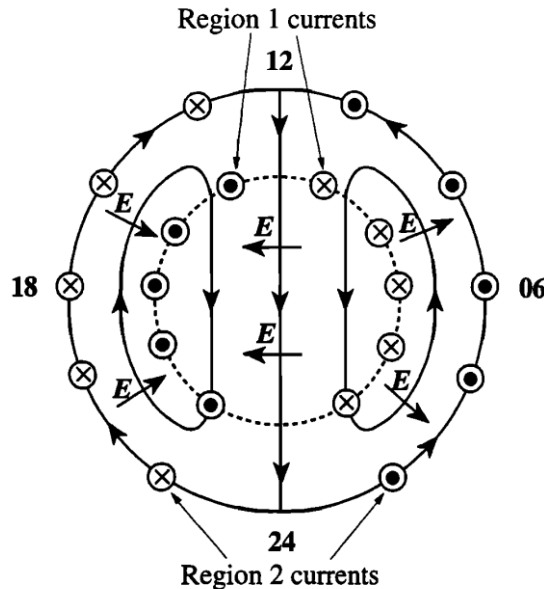


Figure 3.4: Schematic of the ionospheric large-scale two-cell plasma convection pattern associated with the Dungey cycle. Solid arrowed lines are plasma streamlines, while the dashed line is the open-closed field line boundary. Arrows indicate ionospheric electrical fields, with X's and dots indicating the field aligned currents flowing into and out of the ionosphere, closing the current system. Hall currents flow oppositely directed to the plasma streamlines, while Pedersen currents flow along the ionospheric E-fields. The ambient geomagnetic field points into the plane. Adopted from (Cowley, 2000).

Magnetospheric effects of the Dungey cycle maps down to the ionosphere, manifesting a large-scale two-cell plasma convection pattern (Cowley, 2000), as illustrated in Figure 3.4. The ionospheric electric fields E , represented by the small arrows, are imposed by the magnetospheric convection and drive the motion of the plasma perpendicular to the ambient geomagnetic field (which points into the plane).

The electrodynamic forcing generates two horizontal current components: *Pedersen currents*, which flow parallel to the electric field, and *Hall currents*, which flow perpendicular to both E and B i.e., in the $-E \times B$ direction (Cowley, 2000). This horizontal system is coupled to the magnetosphere via Field-Aligned Currents (FACs) flowing along magnetic field lines. These FACs close the circuit, with Region 1 currents mapping to the magnetopause and Region 2 currents to

the partial ring current (Cowley, 2000). In Figure 3.4, the FACs are depicted as circled dots and crosses, indicating flow out of and into the ionospheric plane, respectively.

3.2 Ionospheric Physics

This section provides a brief introduction to the physics of the ionosphere relevant to this thesis. We introduce the concepts of conductivity and conductance, as well as the mechanisms driving Joule heating.

3.2.1 Conductivity and Conductance

The conductivity of a medium quantifies its ability to conduct electric current. It is important to distinguish between *conductivity* (measured in Siemens per meter, S m^{-1}) and *conductance* (measured in Siemens, S). In the context of the ionosphere, the total conductance Σ is generally defined as the conductivity $\sigma(z)$ integrated over altitude z , i.e., $\Sigma = \int \sigma(z) dz$ (Brekke, 2012). Currents arise from the collective motion of charged particles, with the number density determining the available charge carriers, and the collision frequency determining how freely they flow. In the ionosphere, internal collisions between charged particles and neutrals are essential for the generation of Hall and Pedersen currents (Cowley, 2000).

The ability of a particle to drift through the neutral atmosphere under the influence of electromagnetic fields is determined by its mobility (Brekke, 2012). While often defined as a scalar with units, we here define the *dimensionless mobility coefficient* k_s for a species s . This parameter quantifies the ratio of the magnetic gyration frequency to the collisional frequency (Brekke, 2012):

$$k_s = \frac{\omega_{cs}}{\nu_s} \quad (3.1)$$

Here, ω_{cs} represents the gyrofrequency, determined by the species' charge q_s and mass m_s , and the magnetic field strength B :

$$\omega_{cs} = \frac{q_s B}{m_s} \quad (3.2)$$

The term ν_s denotes the total collision frequency, defined as the sum of collision frequencies ν_{sn} between species s and neutral constituents n :

$$\nu_s = \sum_n \nu_{sn} \quad (3.3)$$

The plot in Figure 3.5 shows the ionospheric ion and electron mobility coefficients k_i and k_e , respectively. At lower altitudes $k_i \ll 1$, meaning ions are collision-dominated and relatively immobile with respect to the neutral gas. Meanwhile, $k_e \geq 1$ above ~ 90 km, allowing electrons to exhibit appreciable mobility relative to the neutral atmosphere.

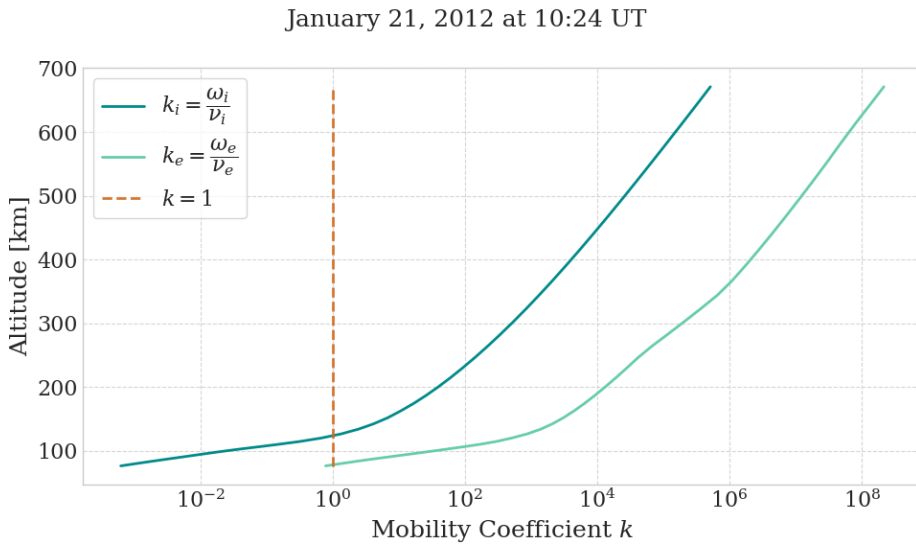


Figure 3.5: The figure shows a plot of the ion and electron mobility coefficients k_i and k_e above EISCAT Ramfjordmoen January 21st 2012 10:24 UT. The orange dashed line indicates where the mobility coefficient k becomes 1. The magnetic field data was obtained from the IGRF model using the Github repository ppigrf (Laundal, 2025). Neutral and ion constituents are obtained from NRLMSISE-oo (Picone et al., 2002) and IRI model (Ilma, 2024), respectively.

Assuming the neutral gas is stationary in the Earth-fixed frame, the drift velocity \mathbf{V}_s for species s is determined by the steady-state force-balance equation (Cowley, 2000):

$$q_s(\mathbf{E} + \mathbf{V}_s \times \mathbf{B}) = m_s v_s \mathbf{V}_s \quad (3.4)$$

where \mathbf{E} and \mathbf{B} are the ionospheric electric and geomagnetic fields, respectively. We focus on the flow perpendicular to \mathbf{B} , the solution for which is given by Equation 3.5 (Cowley, 2000):

$$V_{s\perp} = \frac{1}{1 + \left(\frac{v_s}{\omega_{cs}}\right)^2} \left[\frac{\mathbf{E} \times \mathbf{B}}{B^2} + \left(\frac{v_s}{\omega_{cs}} \right) \frac{\mathbf{E}}{B} \right] \quad (3.5)$$

By substituting the definition of the mobility parameter k_s from Equation 3.1,

we can reformulate Equation 3.5 as:

$$V_{s_\perp} = \frac{1}{1 + \left(\frac{1}{k_s}\right)^2} \left[\frac{\mathbf{E} \times \mathbf{B}}{B^2} + \left(\frac{1}{k_s}\right) \frac{\mathbf{E}}{B} \right] \quad (3.6)$$

Expanding the terms, the drift velocity components along \mathbf{E} and $\mathbf{E} \times \mathbf{B}$ are scaled by the coefficients D_E and $D_{E \times B}$, respectively. These coefficients determine the direction of the drift based on the magnitude of k_s , which varies with altitude:

$$D_{E_s} = \frac{\left(\frac{1}{k_s}\right)}{1 + \left(\frac{1}{k_s}\right)^2} = \frac{k_s}{1 + k_s^2} \quad (3.7)$$

$$D_{E \times B_s} = \frac{1}{1 + \left(\frac{1}{k_s}\right)^2} = \frac{k_s^2}{1 + k_s^2} \quad (3.8)$$

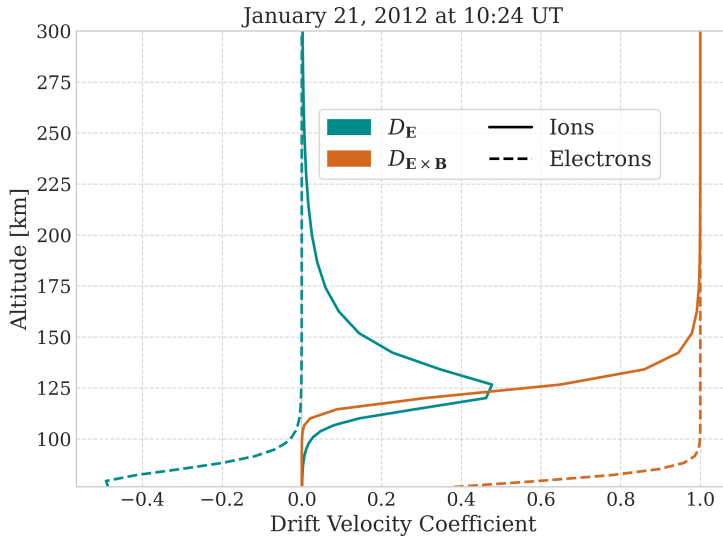


Figure 3.6: The plot shows the coefficients contributing to ion drift parallel to ionospheric E -fields (blue) and in the direction orthogonal to E - and B -fields (orange) for ions (solid) and electrons (dashed).

Figure 3.6 illustrates the altitudinal variation of these drift coefficients. For ions (solid lines), the drift is negligible below 100 km due to high collision rates. The ion drift component parallel to \mathbf{E} (D_E , solid teal line) peaks at ~ 125 km. Above

this altitude, D_E diminishes rapidly as collisions become less frequent, and the $\mathbf{E} \times \mathbf{B}$ term ($D_{E \times B}$, solid orange line) becomes the dominant driver.

For electrons (dashed lines), the $\mathbf{E} \times \mathbf{B}$ drift (orange dashed line) dominates throughout nearly the entire ionosphere. The D_E component for electrons (teal dashed line) is non-negligible only at the lowest altitudes (< 100 km). It is negative due to the particle's charge sign, resulting in a drift opposite to the E-field, but it rapidly converges to zero as altitude increases.

The Pedersen current consists of charged particles flowing parallel to E. As shown by the distinct peak in the solid teal line, this current is carried primarily by ions and is strongest around ~ 125 km. The Hall current, which flows perpendicular to E and B, is dominated by electrons at lower altitudes (where the orange dashed line is ~ 1 while the orange solid line is small). At higher altitudes (> 200 km), $D_{E \times B} \approx 1$ for both species, and as a consequence, electrons and ions drift together in the same direction, resulting in zero net current.

The Hall and Pedersen currents are characterized by the conductivities σ_H and σ_P . Since this thesis focuses on Joule heating, which we later show is driven by Pedersen currents (Zhu et al., 2005), we omit σ_H and focus on σ_P . The Pedersen conductivity is given by (Schunk and Nagy, 2009b):

$$\sigma_P = \sum_i \sigma_i \frac{v_i^2}{v_i^2 + \omega_{ci}^2} + \sigma_e \frac{v_e^2}{v_e^2 + \omega_{ce}^2} \quad (3.9)$$

where σ_s is the scalar conductivity for species s :

$$\sigma_s = \frac{N_s q_s^2}{m_s v_s} \quad (3.10)$$

where N_s is the density of the species. Substituting the mobility parameter k_s into Equation 3.9, we obtain:

$$\sigma_P = \sum_i \sigma_i \frac{1}{1 + k_i^2} + \sigma_e \frac{1}{1 + k_e^2} \quad (3.11)$$

The Pedersen conductivity is linearly dependent on the density of the plasma. However, its relationship with the mobility parameter k is more complex. As seen in Equation 3.11, the term $1/(1 + k^2)$ acts as a suppression factor. If $k \ll 1$ (collision dominated), the particles cannot move effectively. If $k \gg 1$ (magnetic field dominated), the particles drift perpendicular to E rather than along it. Therefore, the Pedersen conductivity is maximized when the collective mobility $k \approx 1$, representing the optimal balance between collisions and magnetic gyration.

3.2.2 Joule Heating

Joule heating is the heating of the neutral atmosphere, caused by currents flowing in the resistive ionospheric medium (Tenfjord and Østgaard, 2013; Koskinen and Tanskanen, 2002). The relative motion between the neutral and charged particles in the atmosphere leads to the dissipation of electrical energy into thermal energy. Vasyliūnas and Song (2005) argues that ionospheric Joule heating is simply frictional heating from the relative motion of plasma and neutrals, and not necessarily primarily Ohmic or Joule heating in the strictest physical sense. Regardless of terminology, this heating increases the thermal motion of the neutral gas particles, effectively causing a vertical expansion of the atmospheric column (Bates, 1974). The significance of this energy transfer is substantial, as Tenfjord and Østgaard (2013) showed that over 50% of solar wind kinetic energy entering the magnetosphere is converted to Joule heating of the neutral atmosphere.

The conservation of electromagnetic energy in an arbitrary volume is described by Poynting's theorem in differential form (Thayer and Semeter, 2004),

$$\frac{\partial W}{\partial t} + \nabla \cdot \mathbf{S} + \mathbf{J} \cdot \mathbf{E} = 0 \quad (3.12)$$

where W is the electromagnetic energy density, \mathbf{S} is the Poynting's flux vector, \mathbf{J} is the current density and \mathbf{E} is the electric field. The theorem states that the time rate of change of electromagnetic energy within a volume ($\frac{\partial W}{\partial t}$) plus the net energy flux flowing out of the volume ($\nabla \cdot \mathbf{S}$) must be balanced by the rate of energy conversion ($\mathbf{J} \cdot \mathbf{E}$).

The conversion term $\mathbf{J} \cdot \mathbf{E}$ represents the transfer of energy between the electromagnetic and mechanical regimes. Following Thayer and Vickrey (1992), this term can be decomposed to distinguish between heating and mechanical work:

$$\mathbf{J} \cdot \mathbf{E} = \mathbf{J} \cdot \mathbf{E}' + \mathbf{V}_n \cdot (\mathbf{J} \times \mathbf{B}) \quad (3.13)$$

where \mathbf{V}_n is the neutral wind velocity, and \mathbf{E}' is the electric field in the reference frame of the neutral gas, given by (Thayer and Semeter, 2004):

$$\mathbf{E}' = \mathbf{E} + \mathbf{V}_n \times \mathbf{B} \quad (3.14)$$

The first term in Equation 3.13, $\mathbf{J} \cdot \mathbf{E}'$, represents the Joule heating rate: the rate at which electrical energy is dissipated as heat in the neutral gas (Thayer and Vickrey, 1992). The second term, $\mathbf{V}_n \cdot (\mathbf{J} \times \mathbf{B})$, represents the mechanical energy transfer rate (Thayer and Semeter, 2004).

If we assume the neutral gas is stationary ($\mathbf{V}_n = 0$), Equation 3.14 simplifies to $\mathbf{E}' = \mathbf{E}$, and the total energy conversion is purely dissipative. To derive the

specific heating rate, we decompose the current density and electric field into components parallel and perpendicular to the geomagnetic field (i.e., $\mathbf{J} = \mathbf{J}_\perp + \mathbf{J}_\parallel$). Since the magnetic field lines are highly conductive, the electric potential drop along \mathbf{B} is negligible in the thermosphere, allowing us to approximate $\mathbf{J} \cdot \mathbf{E}' \approx \mathbf{J}_\perp \cdot \mathbf{E}'_\perp$ (Zhu et al., 2005).

The perpendicular current density is given by Ohm's law (Zhu et al., 2005):

$$\mathbf{J}_\perp = \sigma_P \mathbf{E}'_\perp + \sigma_H \hat{\mathbf{B}} \times \mathbf{E}'_\perp \quad (3.15)$$

where σ_P and σ_H are the Pedersen and Hall conductivities, respectively, and $\hat{\mathbf{B}}$ is the unit vector along the geomagnetic field (Zhu et al., 2005). Substituting Equation 3.15 into the expression for the Joule heating rate q yields:

$$q = \mathbf{J}_\perp \cdot \mathbf{E}'_\perp = [\sigma_P \mathbf{E}'_\perp + \sigma_H (\hat{\mathbf{B}} \times \mathbf{E}'_\perp)] \cdot \mathbf{E}'_\perp \quad (3.16)$$

The Hall term vanishes because the vector $\hat{\mathbf{B}} \times \mathbf{E}'_\perp$ is orthogonal to \mathbf{E}'_\perp , making their dot product zero. Consequently, Joule heating is driven solely by the Pedersen conductivity and \mathbf{E}'_\perp :

$$q = \sigma_P |\mathbf{E}'_\perp|^2 \quad (3.17)$$

For clarity, we define the altitude-dependent Joule heating rate as q (W m^{-3}) and the height-integrated Joule heating rate as Q (W m^{-2}). This derivation highlights that Joule heating is a resistive process governed by the Pedersen conductivity. The vertical expansion of the neutral atmosphere that follows, increases the particle density at higher altitudes, which can lead to increased satellite drag (Fang et al., 2022), and changes in the ion chemistry of the upper atmosphere (Fuller-Rowell et al., 1994).

3.3 Incoherent Scatter Radar Theory

In this section we take a brief look back on the history of incoherent scattering theory, before establishing electromagnetic scattering principles and their application to the ISR technique. To maintain alignment with the thesis objectives, the discussion remains concise rather than exhaustive.

3.3.1 Historical Overview and Significance

Following Thomson (1906)'s identification of electrons as negative current carriers and the formulation of scattering from free particles, also known as Thomson scattering, interest in the electromagnetic properties of the upper

atmosphere grew. By the 1920s, the existence of the ionosphere was established (Appleton and Barnett, 1925).

In his 1958 paper, W.E. Gordon proposed the use of Thomson scattering of radio waves by free electrons to observe ionospheric plasma parameters (Gordon, 2007). With the assumption that the scattering would be from independent electrons moving at thermal velocities, he predicted that the backscattered radio waves would have a very wide spectral width, with a Maxwellian distribution. Bowles (1961) made the first observations of incoherent scattering from ionospheric plasma, but noted that the spectral width was indeed much narrower than Gordon's prediction. He offered the explanation that the electrons were not *free*, but coupled to the ions through electrostatic forces. This coupling causes electrons to exhibit a *collective* behaviour controlled by the ions (Bowles, 1961).

In the following years, numerous authors published theories of incoherent scattering, e.g., (Fejer, 1960; Salpeter, 1960; Hagfors, 1961; Dougherty and Farley, 1961). See Kudeki and Milla (2010) for a modern treatment of the ISR theory and a discussion on how the different formulations relate to one another. In parallel with theoretical efforts, several incoherent scatter radars were established, such as Jicamarca, Arecibo, and the EISCAT facilities. Later developments introduced phased arrays like the Poker Flat ISR. Unlike ionosondes, which rely on total reflection, ISRs operate at frequencies above the plasma frequency. This allows the radio wave to permeate the ionosphere, making topside measurements possible. Today, the incoherent scatter technique is the state-of-the-art technique for ground-based ionospheric measurements, as it provides altitude profiles for ionospheric plasma parameters like electron density, electron and ion temperature, and ion Line-Of-Sight (LOS) velocity V_{LOS} simultaneously.

3.3.2 Fundamentals of Electromagnetic Scattering

Thomson Scattering

Thomson scattering is the elastic scattering of electromagnetic radiation by a free charged particle. The total Thomson scatter cross-section of an electron is defined as $\sigma_e = 6.65 \times 10^{-29} \text{ m}^2$ (Gordon, 2007). The incident electromagnetic plane wave transmitted by the radar possesses a spatiotemporally varying electric field. As the wave approaches the electron, the electron is accelerated by the E-field, which eventually leads to its oscillation and emittance of electromagnetic radiation at the wave frequency (Kudeki and Milla, 2010). Due to the mass difference between electrons and ions, incident ISR waves do not possess enough energy to oscillate the ions significantly; therefore, we only receive

incoherent backscatter from electrons.

ISRs require massive transmitters and receivers to detect signals of the electron cross-section scale, as the proportionality between the received radar power P_R and σ_e can, to a first order approximation, be expressed by Equation 3.18 (Chen, 2004; Beynon and Williams, 1978):

$$P_R \propto \sigma_e N_e \left(1 + \frac{T_e}{T_i}\right)^{-1} \quad (3.18)$$

Collective Plasma Behavior

A fundamental behavioral property of plasma is its inherent ability to neutralize applied electric potentials through a mechanism called *Debye shielding* (Chen et al., 1984). The *Debye length* λ_D is a quantification of the shielding distance, expressed by Equation 3.19 (Chen et al., 1984),

$$\lambda_D = \left(\frac{\epsilon_0 k_B T_e}{N q^2} \right)^{\frac{1}{2}} \quad (3.19)$$

where ϵ_0 is the permittivity of free space in units of Fm^{-1} , k_B is Boltzmann's constant in units of JK^{-1} , T_e is electron temperature in units of K, N is the plasma density far away from the applied charge in units of m^{-3} , and q is the charge of the plasma's constituent particles in units of Coulomb. To ensure that the plasma is large enough for these shielding distances to be negligible, the characteristic length of the plasma, L , must be sufficiently large, such that $\lambda_D \ll L$ (Chen et al., 1984; Pécseli, 2025).

If the radar wavelength λ_R is comparable to or less than λ_D , the incoherent backscatter will be from independent particles (Pécseli, 2025). For radar wavelengths much larger than λ_D , the radar is able to resolve collective behavior, such as Debye shielding of ions and other plasma density fluctuations Rexer (2021). The scattering is still from the electrons, but their overall motion is controlled by the ions.

The Bragg vector \mathbf{k}_B is the difference between the transmitted and received wave vectors (Kudeki and Milla, 2010). The Bragg scattering condition determines the density fluctuation wavelengths of the ionospheric plasma we can observe for a given radar system (Rexer, 2021)

$$\Lambda = \frac{\lambda_R}{2 \cos \theta}$$

where θ is the angle between the incident and backscattered wave. Density fluctuations in plasma are often due to thermal gradients, and manifest themselves as plane waves of all wavenumbers k in all directions (Rexer, 2021). For

monostatic radar systems, meaning where radar transmitter and receiver are co-located, $\theta = 180$, which corresponds to density fluctuations of wavelength $\Lambda = \frac{\lambda_R}{2}$ (Rexer, 2021). The two wave modes from which the ISR receive spectra are the ion acoustic and electron acoustic (or plasma) waves.

3.3.3 ISR Spectrum and Its Interpretation

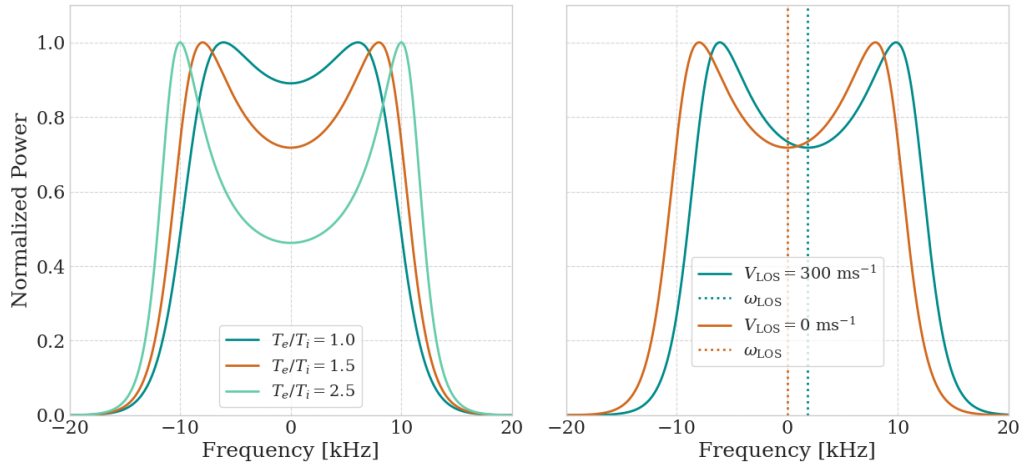


Figure 3.7: Plots showing multiple configurations of the ion line. The left plot visualizes transition of the ion line ISR spectrum for different temperature ratios T_e/T_i . The right plot shows how the ion line (using $T_e/T_i = 1.5$) is Doppler shifted in frequency domain due to ion velocity. Here we consider only O⁺-ions and electrons as the constituent particles, with $N_e = 2 \times 10^{11} \text{ m}^{-3}$, $T_i = 1000K$ and a radar frequency $f_R = 930 \text{ MHz}$, similar to that of the EISCAT UHF. The figure was made using supervisor Juha Vierinen's Github repository `isr_spec` (Vierinen, 2025).

The returned signal is spread in frequency domain due to the thermal motion of the scattering particles. Figure 3.7 shows two plots of normalized power spectra for the ion acoustic waves i.e., the ion line. The left plot showcases how the spectrum "shoulders" sharpens and broadens for increasing T_e/T_i -ratio. The right plot shows how the ion line is Doppler shifted by ω_{LOS} in frequency, with the dotted lines indicating the shift. By measuring this shift, we can infer the ion LOS velocity V_{LOS} given by:

$$V_{\text{LOS}} = \frac{\omega_{\text{LOS}} \lambda_R}{4\pi} \quad (3.20)$$

As the backscatter from the ionosphere is caused by Thomson scattering of electrons, the power density is directly proportional to the electron density N_e (Beynon and Williams, 1978). The broadness of the ion line spectrum is directly

proportional to the ratio T_i/m_i where m_i is the ion mass, giving rise to the well-known mass-temperature ambiguity. However, with sophisticated models of the ionospheric constituents, we can resolve it.

3.4 Machine Learning and Deep Neural Networks

In this section, we introduce the field of machine learning and some of its fundamental concepts. We then introduce and describe Multilayer Perceptrons and their structure, the role of loss functions, the optimization process, and finally, regularization techniques to prevent overfitting.

3.4.1 Machine Learning

At the intersection of computer science and statistics lies the field of machine learning, which improves system performance by learning from experience via data-driven computational methods (Jordan and Mitchell, 2015; Zhou, 2021). Throughout the 20th century, the interest in machine learning has had its peaks and troughs. The start of the 21st century has seen the renaissance of machine learning, driven by the growth of Big Data, reduced cost of memory and parallel computing, as well as the development of *deep* machine learning algorithms (Fradkov, 2020). The field is evolving rapidly due to the intense industry demand and its relatively recent emergence as a distinct scientific discipline.

The primary goal of this thesis is to predict field-aligned electron density profiles from local plasma and global geophysical parameters. Since electron densities are continuous, real-valued physical quantities, this problem is inherently a regression task, falling under the field of supervised learning (Goodfellow, 2016). Supervised learning algorithms construct models by learning from datasets consisting of input-output pairs (Cunningham et al., 2008). The inputs are referred to as *features*, often denoted as \mathbf{x} , and the outputs as *labels*, denoted as \mathbf{y} (Zhou, 2021). The fundamental goal is to learn a mapping from the features to the labels, based on a finite set of training examples. The trained models can then be used for the prediction of labels from new, unseen features. To approximate this complex mapping, we employ the mathematical framework of Deep Neural Networks, specifically Multilayer Perceptrons, which are detailed in the following section.

3.4.2 Multilayer Perceptrons

Deep feedforward networks, also known as Multilayer Perceptrons (MLPs), are the cornerstone of deep learning models. This mathematical framework has the ability to map complex, non-linear relationships, making it an excellent tool for tackling complex real-world problems.

Given an input vector \mathbf{x} and a desired label \mathbf{y} , we make the assumption that there exists a true underlying function f mapping \mathbf{x} to \mathbf{y} . In general, f is not known. To estimate this mapping, we define a neural network model \hat{f} , parameterized by a set of weights and biases, denoted θ . The objective is to learn these parameters from training data, allowing us to transform an input \mathbf{x} into a predicted output $\hat{\mathbf{y}}$:

$$\hat{\mathbf{y}} = \hat{f}(\mathbf{x}; \theta) \quad (3.21)$$

Here, the notation $\hat{f}(\mathbf{x}; \theta)$ implies that the function \hat{f} is defined by the parameters θ (Goodfellow, 2016). The output $\hat{\mathbf{y}}$ represents either class probabilities for the classification case, or continuous numerical values for the regression task. These deep networks are composed of elementary building blocks called *neurons*, and a schematic of a single neuron's architecture is shown in Figure 3.8. Neurons are aggregated in parallel to form a *layer*. For a single neuron j , the output, often called the *activation* a_j , is calculated as:

$$a_j = \sigma(\mathbf{w}_j^T \mathbf{x} + b_j) \quad (3.22)$$

where \mathbf{x} is the input vector to the neuron, \mathbf{w}_j is the weight vector and b_j is the bias scalar. The term $\mathbf{w}_j^T \mathbf{x} + b_j$ represents a linear affine transformation, while σ is the non-linear *activation function* (Goodfellow, 2016). The activation function is the fundamental element that allows the network to model non-linear relationships (Sharma et al., 2017). Without non-linear activation functions, deep neural networks reduce to a linear function.

The architecture of an MLP is formed by stacking these layers in depth. The output of one layer becomes the input to the next, creating a deep hierarchy capable of learning data representations with increasing levels of abstraction (LeCun et al., 2015). The number of layers and neurons within each layer are hyperparameters that can be adjusted to fit a specific task's needs.

The Universal Function Approximation Theorem, established in the late 1980s, states that a feed-forward network with a single hidden layer containing a finite number of neurons can approximate any continuous function on compact subsets of \mathbb{R}^n to arbitrary precision (Hornik et al., 1989). In the context of incoherent scatter radar data, this provides the theoretical justification that a neural network is capable of representing the complex mapping from local plasma- and geophysical state parameters to an entire field-aligned electron

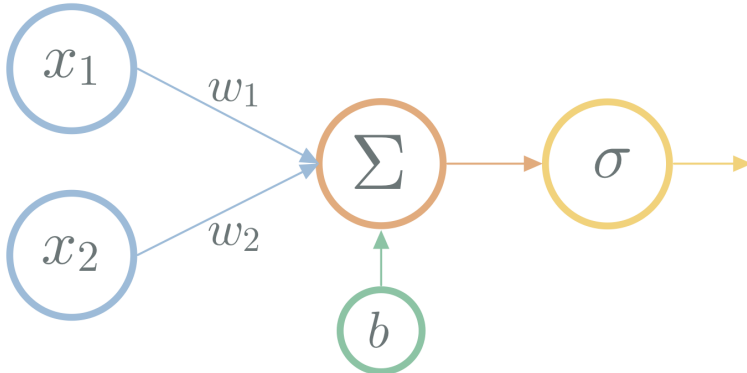


Figure 3.8: Schematic of a single neuron’s architecture. The input features, x_1 and x_2 , are multiplied by their corresponding weights, w_1 and w_2 , and added to the bias term b to form the weighted sum Σ . This sum is passed through an activation function σ to generate the neuron’s final output.

density profile. However, while this theorem guarantees the existence of such a solution, it is not given that the training algorithm will be able to find it; that depends on the optimization process and the quality of the data.

3.4.3 Loss Functions

A loss function \mathcal{L} serves as a quantitative metric for evaluating a model’s performance by measuring the discrepancy between predictions and ground truths (Goodfellow, 2016). Since the ground truths are fixed observations, and the predictions are determined by the model’s parameters θ , the loss becomes strictly a function of θ . Consequently, we can define a *loss space* spanned by these parameters, within which the value of the loss function maps out a *loss surface* (Li et al., 2018). Figure 3.9 visualizes a three-dimensional example of such a surface, illustrating how the topography represents the success of the model. Lower points on the surface generally correspond to parameter combinations that yield more accurate predictions (Goodfellow, 2016).

The choice of loss function depends on the task at hand, as different loss functions penalize the model with different objectives. One very common loss function for the regression task is the Mean Squared Error (MSE) (Goodfellow, 2016):

$$\mathcal{L}(\theta) = \frac{1}{N} \sum_{i=1}^N (\mathbf{y}_i - \hat{\mathbf{y}}_i)^2 \quad (3.23)$$

where \mathbf{y} and $\hat{\mathbf{y}}$ are true and predicted labels respectively, and N the number of samples. Squaring the error penalizes larger errors more compared to smaller

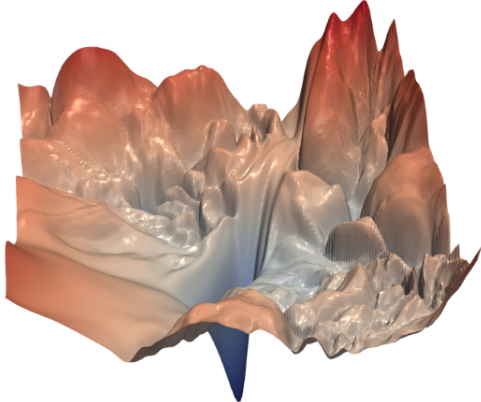


Figure 3.9: Visualization of a 3D loss surface. Adapted from Li et al. (2018).

ones. Another loss function that proves beneficial for regression tasks is the robust Huber Loss, combining Mean Absolute Error (MAE) for large errors and MSE for smaller errors (Huber, 1992). The choice of loss function defines the topology of the loss surface (Goodfellow, 2016).

3.4.4 Optimization

Optimization is the process of navigating the loss landscape to find the set of parameters θ that minimizes the loss function \mathcal{L} (Goodfellow, 2016). Leveraging the geometric abstraction of the loss as a multi-dimensional surface, the fundamental strategy for moving "downhill" is *Gradient Descent*. This involves calculating the gradient of the loss with respect to the network parameters and updating the weights and biases in the direction *opposite* to the gradient (Goodfellow, 2016).

The efficient calculation of these gradients is achieved through *backpropagation*, which is essentially a recursive application of the *chain rule* of calculus (Goodfellow, 2016). The magnitude of the parameter adjustment in each step is regulated by the *learning rate* η (Goodfellow, 2016).

Since calculating gradients for the entire dataset at once can be computationally demanding, the data is often divided into smaller *batches*. This approach, known as *Stochastic Gradient Descent* (SGD), introduces noise into the gradient estimation which stochastically helps the optimizer escape local minima (Goodfellow, 2016). State-of-the-art optimization today typically employs adaptive methodologies. The *Adam* optimizer (Adaptive Moment Estimation) introduces an adaptive method for adjusting the step size of the gradient update, as well as individual learning rates for each parameter (Kingma et al., 2014). We employ

AdamW, which improves upon Adam by decoupling weight-decay from the gradient update. This effectively regularizes the model, by stabilizing training and improving the model's ability to generalize to new data (Loshchilov et al., 2017).

3.4.5 Regularization

Regularization is a set of techniques used for preventing *overfitting* in neural networks (Goodfellow, 2016). Overfitting happens when the capacity, or the complexity, of the neural network is too large compared to the available training data. In that case, the model learns the training data too well, including random noise and variations, ultimately failing to *generalize* well (Goodfellow, 2016). A well-trained high-performance model is characterized by a high degree of generalization, meaning it effectively processes unseen data.

To mitigate overfitting, several techniques can be employed. *Weight decay*, or L₂ regularization, adds a penalty term to the loss function proportional to the weight magnitudes. This prevents any weight from growing too large, ensuring that the model learns a smooth mapping. By choosing the smallest vector that solves the learning problem, weight decay suppresses any irrelevant components of the weight vector (Krogh and Hertz, 1991).

To ensure that the model learns robust features, rather than relying on single neuron activations, we can employ dropout. During training, neuron activations are set to zero with a probability of p . This improves generalization by preventing units from co-adapting, i.e., preventing the model from learning unique, brittle pathways (Srivastava et al., 2014).

The use of batches introduces regularization through the stochastic nature of batch variations. As discussed in Subsection 3.4.4, the noisy gradients of the batches help the model escape local loss surface minima. Although an optimization technique designed to normalize layer inputs and prevent internal covariate shift, Batch Normalization (Ioffe and Szegedy, 2015) also provides regularization effects. The inherent noise in computing the mean and variance over batches introduces a stochastic element to the training process, which helps prevent overfitting.

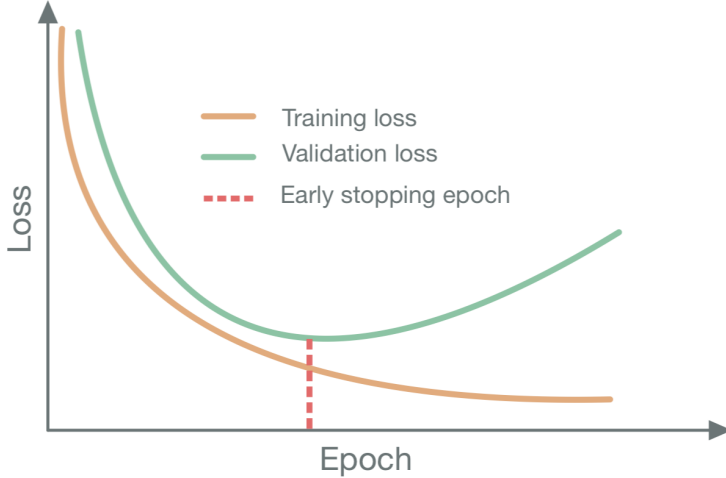


Figure 3.10: Schematic showing idealized training (orange) and validation (green) loss curves. The dashed pink line indicates the epoch at which the validation loss reaches its minimum.

The last regularizing technique we will mention here is *early stopping* of the training process, to ensure that the model is not overfitted on the training data (Goodfellow, 2016). During training, the model is evaluated on the validation set after each iteration over the training set, yielding the validation loss. One iteration over the training and validation set is called an *epoch*. When employing early stopping, the training of the model is stopped once the validation loss is starting to increase due to overfitting on the training set. We then fall back on the model state characterized by the lowest validation loss. Figure 3.10 shows the training and validation loss curves in orange and green, respectively, and the additional dashed pink line indicates the epoch after which the model performance on the validation set is starting to degrade. The key idea here is to stop the training when the model reaches its lowest validation loss (Goodfellow, 2016).

/ 4

Methodology

In this chapter, we outline the datasets and computational methods employed in this thesis. Section 4.1 details the instrumentation and data acquisition procedures. Section 4.2 presents an exploratory data analysis, establishing the necessary preprocessing steps for the training datasets. Section 4.3 describes the selected neural network architecture, loss functions, and training hyperparameters. Finally, Section 4.4 details the methodology for predicting electron density profiles, calculating Pedersen conductivity, and estimating the subsequent Joule heating rates.

4.1 Datasets

This section describes the curation of datasets used for training and case studies. We detail the instrumentation, data origins, and geophysical indices employed. High-quality input data is critical for Deep Learning applications, as "without good data, even the best machine learning algorithms cannot perform well." (Whang et al., 2023).

Incoherent Scatter Radar

The primary data sources for this thesis are the monostatic EISCAT UHF and VHF radar systems located at the Ramfjordmoen facility near Tromsø (Tjulin,

2025).

The EISCAT UHF radar employs a fully steerable 32 m parabolic dish operating in the 930 MHz band. It functions as both a transmitter and receiver, with a peak transmitter power of 2.0 MW, a 12.5% duty cycle, and pulse lengths ranging from $1 \mu\text{s}$ to 10 ms . The minimum elevation limit for radio transmissions is 25° (Tjulin, 2025).

The EISCAT VHF radar consists of a parabolic cylinder with four 30 m x 40 m tiltable rectangular dishes, operating in the 224 MHz band. Similar to the UHF, it is a transceiver system with a peak power of 3.0 MW, a 12.5% duty cycle, and pulse lengths of $1 \mu\text{s}$ to 2 ms . The VHF radar is restricted to transmission angles from zenith northward, with a lower elevation limit of 25° (Tjulin, 2025). Both radars are capable of frequency and phase modulation. Technical specifications were obtained from (EISCAT AB, 2021) unless otherwise specified.

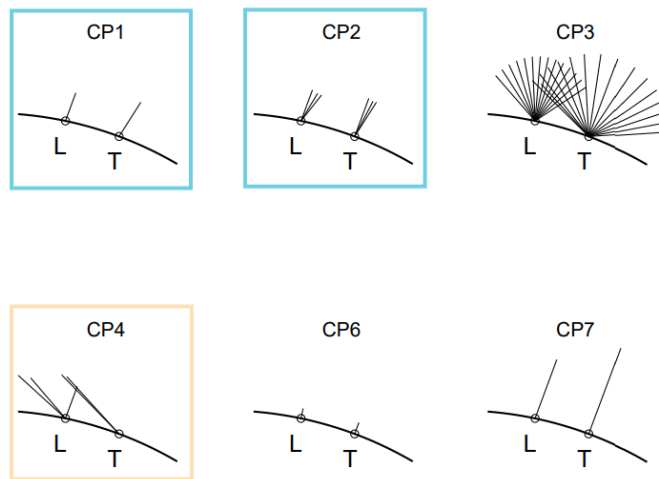


Figure 4.1: Schematic of EISCAT radar scan patterns CP1 through CP6. L and T denote the EISCAT radar sites near Longyearbyen and Tromsø, respectively. The blue and orange frames indicate the scan patterns associated with the UHF and VHF datasets used in this thesis, respectively. Figure adapted from (Tjulin, 2025).

EISCAT radars operate in two primary modes: Special Programmes (SP) and Common Programmes (CP). SPs are individual campaigns where data is reserved for the user for a specific period (Tjulin, 2025). Conversely, CPs are conducted regularly by EISCAT, and the resulting data is immediately available to the community. CPs utilize pre-defined antenna scan patterns to accommodate various scientific objectives, and a schematic of these patterns is shown in Figure 4.1.

The CP1 and CP2 patterns (blue frames in Figure 4.1) contain field-aligned measurements in the ionospheric region of interest. These patterns are exclusively used in the *beata* experiment conducted with the UHF radar (Tjulin, 2025). Consequently, the field-aligned training dataset is derived from instances where the UHF radar operated the *beata* programme.

The CP4 programme (orange frame in Figure 4.1) covers a wide range of latitudes due to its low elevation. In this configuration, the radar beam has a significant perpendicular component to the geomagnetic field, intersecting field lines at various altitudes as illustrated previously in Figure 2.2. The *bella* experiment is the only standard experiment using the CP4 programme on the mainland VHF system (Tjulin, 2025). Therefore, the case study dataset covering a range of geomagnetic field lines is derived from *bella* operations. These will be referred to as the UHF and VHF datasets, respectively.

The radars measure ionospheric plasma parameters, and this thesis primarily utilizes electron density, electron temperature, and ion temperature. Additionally, ion LOS velocity is used for the Joule heating calculation in the case studies presented in Section 6.1. All EISCAT data is retrieved from the Madrigal database (Rideout and Cariglia, N.D.) via the Python API.

4.1.1 The UHF Dataset

The training dataset is constructed from EISCAT UHF data collected using the *beata* experiment. We retrieve 1-minute resolution data, specifically filtering for measurements with radar elevations above 70° . This elevation threshold is selected to ensure the radar beam is approximately aligned with the local geomagnetic field line ($\sim 12^\circ$ off zenith), which is a prerequisite for the field-aligned modeling approach.

Ideally, the dataset would span multiple solar cycles (~ 22 years) to capture long-term ionospheric variations. However, the *beata* experiment was not commissioned until approximately 2007, which limits the temporal extent of our dataset to the period 2007–2024. While data from other experiments, such as *tau* (Tjulin, 2025), exist for earlier periods, they were excluded from this analysis to ensure consistency in the radar scan patterns and pulse codes.

4.1.2 The VHF Dataset

For the application and evaluation of the trained model, we construct a separate dataset containing low-elevation radar scans. We retrieve 1-minute resolution VHF data collected using the *bella* experiment, restricting the query to radar

elevations between 25° and 40° . In this geometric configuration, the radar beam intersects the geomagnetic field lines at an oblique angle, allowing for the reconstruction of plasma parameters across multiple field lines as described in the introduction.

4.1.3 Geophysical State Parameters

Observations of the solar wind, geomagnetic conditions, FACs, and ground magnetic disturbances have previously been utilized to construct empirical conductance models (Ma et al., 2025, & references therein). The inclusion of these parameters provides critical global context regarding ionospheric and magnetospheric conditions, information that is not inherent in the local plasma parameter measurements provided by ISRs.

We supplement the ISR plasma parameters with the following geophysical indices: AE, AL, SYM/H, PCN, A_p , and F10.7. The AE and AL indices quantify the intensity and direction of ionospheric currents related to global electrojet activity (Davis and Sugiura, 1966). The SYM/H index measures the intensity of the storm-time ring current, calculated from the symmetric portion of the horizontal magnetic field component near the equator (Wanliss and Showalter, 2006). The Polar Cap North (PCN) index estimates the cross-polar current intensity driven by electric fields associated with anti-sunward plasma convection and Dungey cycle dynamics (Stauning, 2013). The A_p index quantifies daily geomagnetic activity derived from mid-latitude observations (Rostoker, 1972). Finally, the F10.7 index, representing the solar radio flux at the wavelength 10.7 cm, serves as a robust proxy for solar activity (Tapping, 2013).

These parameters are retrieved from OMNIWeb (NASA, N.D.) with varying time resolutions. AE, AL, SYM/H, and PCN are available at 5-minute resolution, while A_p and F10.7 are provided at 1-hour resolution. To synchronize these datasets with the high-resolution ISR data, the lower-resolution parameters are linearly interpolated to match the timestamps of the ISR measurements.

4.2 Exploratory Data Analysis and Preprocessing

This section outlines the processing pipeline used to transform the raw EISCAT and geophysical datasets into a curated, high-quality format suitable for deep learning. While a comprehensive exploratory data analysis (EDA) is presented in Appendix A, we summarize here the key findings that dictate our preprocessing strategy.

4.2.1 Data Cleaning and Filtering

Based on the analysis detailed in Appendix A, several cleaning and filtering steps were applied to the UHF training dataset to ensure consistent and high-quality data.

As shown in Figure A.2, the radar data contains varying profile lengths. We restrict the dataset to measurements with exactly 42 range gates to ensure a fixed-size output vector for the neural network.

To account for the secular variation of the geomagnetic field (see Figure A.9), we filter the dataset to include only measurements with radar elevations $\in [76^\circ, 79^\circ]$ and azimuths $\in [184^\circ, 190^\circ]$. This ensures the training data represents true field-aligned conditions.

Profiles containing NaN values in any plasma parameter (N_e, T_e, T_i) are removed entirely. This results in a clean dataset of approximately 440,000 unique profiles.

4.2.2 Data Processing

The aim of our neural network is to predict field aligned electron density profiles. To achieve this, we structure our data to use the local plasma conditions to predict the entire profile.

More specifically, for each measurement, we deconstruct the measured profiles into individual, altitude-specific feature sets. Feature vectors are formed using the electron density, electron temperature and ion temperature at a single altitude, supplemented by the altitude value, and the geophysical state parameters. The corresponding label for each feature vector is the entire 42-point electron density profile for that measurement. Thus, each complete profile is utilized as the target label 42 times, each time associated with the features from one of its constituent altitudes. This approach augments the dataset size by a factor of 42.

In other words, our neural network learns to predict an *entire* field aligned electron density profile, from a single datapoint of electron density, electron temperature, and ion temperature, given the altitude of these measurements and additional knowledge of the geophysical conditions.

4.2.3 Transformation and Normalization

The distribution of plasma parameters, particularly electron density, spans several orders of magnitude (see Figure A.11). To compress this dynamic range and stabilize the training process, we apply a \log_{10} transformation to N_e , T_e , and T_i . To prevent numerical errors from zero-values, a unity shift is applied prior to the logarithm:

$$x_{\text{trans}} = \log_{10}(x_{\text{raw}} + 1)$$

Following the log-transformation, the features require standardization. As noted in the EDA (see Figure A.11 and Figure A.19), the dataset contains significant outliers. Standard normalization is sensitive to such outliers, and we therefore employ *Robust scaling*. This method scales the data using the median and the Interquartile Range (IQR), making it resilient to extreme values:

$$X_{\text{scaled}} = \frac{X - \text{median}(X)}{\text{IQR}(X)}$$

All parameters are scaled using this method, except for the cyclical time features ($\sin(\text{TOD})$, etc.) that are already bounded $\in [-1, 1]$.

4.2.4 Data Splitting

For robust model training and evaluation, the dataset is partitioned into training, validation, and test sets. A critical consideration is the prevention of *data leakage* stemming from our feature-label architecture. As a single profile generates 42 training samples, a simple random split would place different data points from the exact same profile into both the training and test sets, invalidating the evaluation. We circumvent this by using a strict chronological separation by year. This split is also designed to test the model's generalization across different solar conditions, with each dataset containing periods of both solar minimum and maximum. The specific split is detailed in Table 4.1.

Table 4.1: Train, test and validation dataset split by year.

Dataset	Years	Samples (approx.)
Train	2009-2021	13.78M
Test	2007, 2023, 2024	2.50M
Validation	2008, 2022	1.90M

4.3 Model

4.3.1 Model Architecture

We employ a Fully Connected Neural Network (FCNN) designed to map the scalar input features to the complete field-aligned electron density profile. The network consists of an input layer, three hidden layers and an output layer, with the specific neuron configuration of (15, 128, 256, 128, 42). This architecture comprises a total of 73,386 trainable parameters, as detailed in Table 4.2.

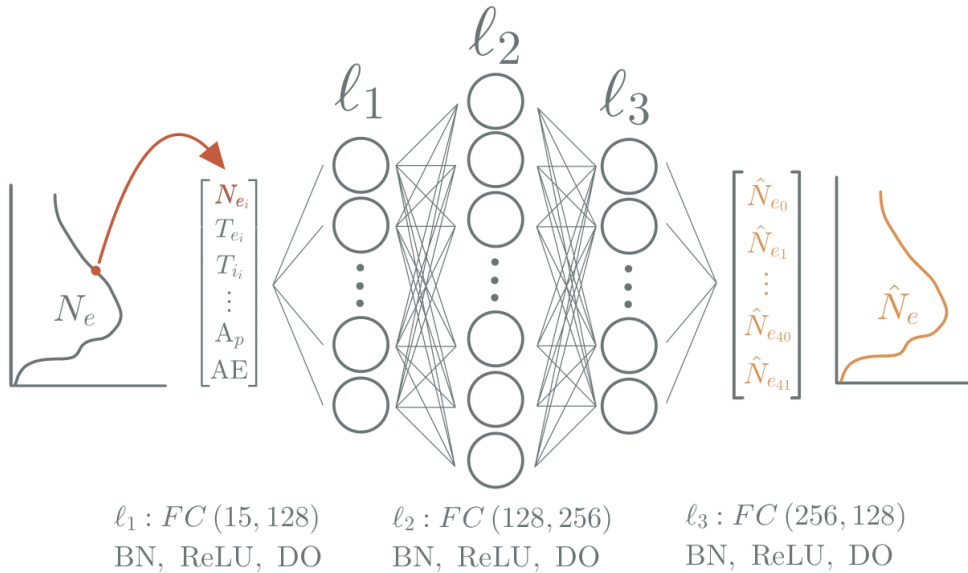


Figure 4.2: Schematic of the Fully Connected Neural Network (FCNN) architecture. The input vector (left), derived from plasma parameters at a single altitude i combined with geophysical indices, is mapped to a complete predicted electron density profile \hat{N}_e (right). The network comprises three hidden layers (ℓ_1, ℓ_2, ℓ_3), each utilizing Batch Normalization (BN), ReLU activation, and Dropout (DO).

To mitigate overfitting and accelerate convergence, the input and each hidden layer is followed by Batch Normalization (Ioffe and Szegedy, 2015), a Rectified Linear Unit (ReLU) activation function, and a Dropout layer. The output layer is linear, providing the regression values for the 42-point electron density profile. A schematic of the architecture is presented in Figure 4.2.

Table 4.2: Parameter breakdown for the FCNN architecture.

Layer Connection	Weight Matrix W	Bias Vector b	Parameter Count
Input → Hidden 1	(128 × 15)	(128 × 1)	$128 \times 15 + 128 = 2,048$
Hidden 1 → Hidden 2	(256 × 128)	(256 × 1)	$256 \times 128 + 256 = 33,024$
Hidden 2 → Hidden 3	(128 × 256)	(128 × 1)	$128 \times 256 + 128 = 32,896$
Hidden 3 → Output	(42 × 128)	(42 × 1)	$42 \times 128 + 42 = 5,418$
Total Parameters			73,386

4.3.2 Loss Function Development

Defining an appropriate loss function is critical when working with ISR data, which is inherently noisy due to the nature of the scattering process and radar theory.

Handling Data Noise

Initial experiments explore preprocessing techniques to suppress noise in the ground truth profiles. We test temporal median filtering with varying kernel sizes ($k \in [3, 5, 7]$), as shown in Figure 4.3. While the variance appears to be reduced by this technique, it only accentuates the vertical feature around 10^{10} m^{-3} . This appears to be a systematic artifact of the radar system, and not the manifestation of a physical phenomena.

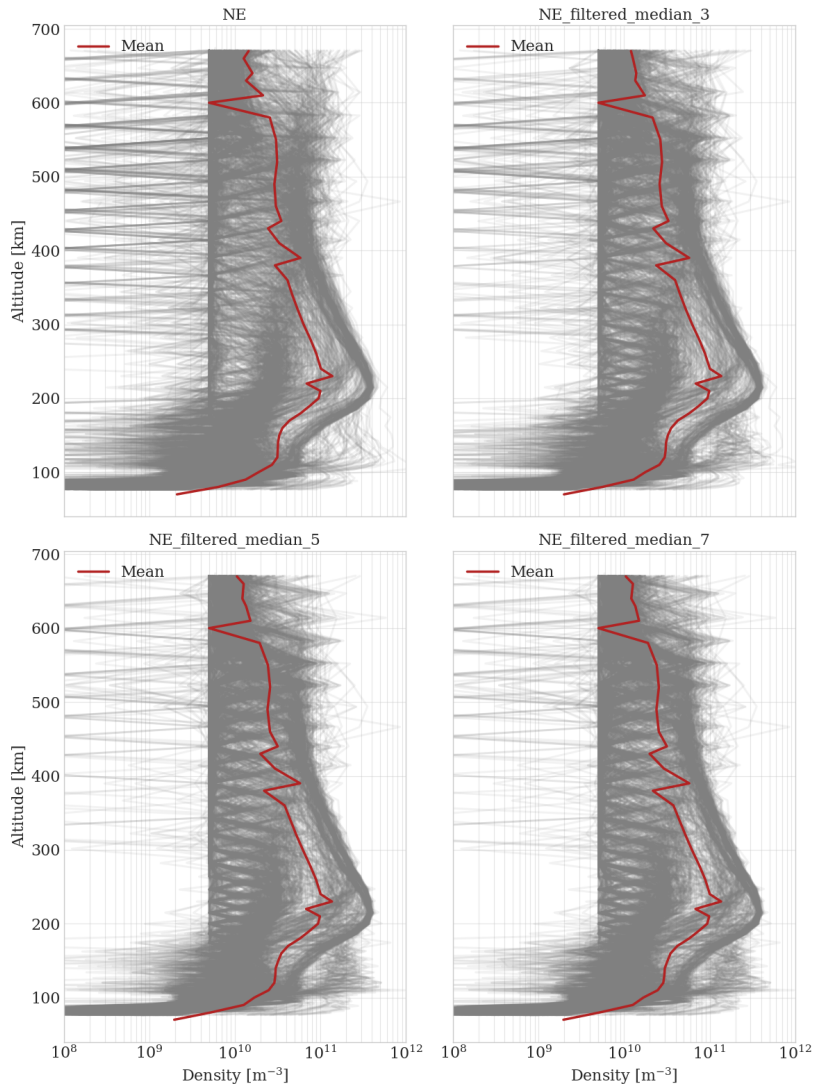


Figure 4.3: The figure shows random samples of electron density profiles, from no filtering on the upper left, to increasing temporal median filtering kernel $k \in [3, 5, 7]$, respectively.

Subsequent attempts utilize splines to reduce the "zig-zag" noise pattern. However, as illustrated in Figure 4.4, this approach tends to underestimate high-density peaks in the E-region, effectively skewing the electron density distribution towards lower magnitudes.

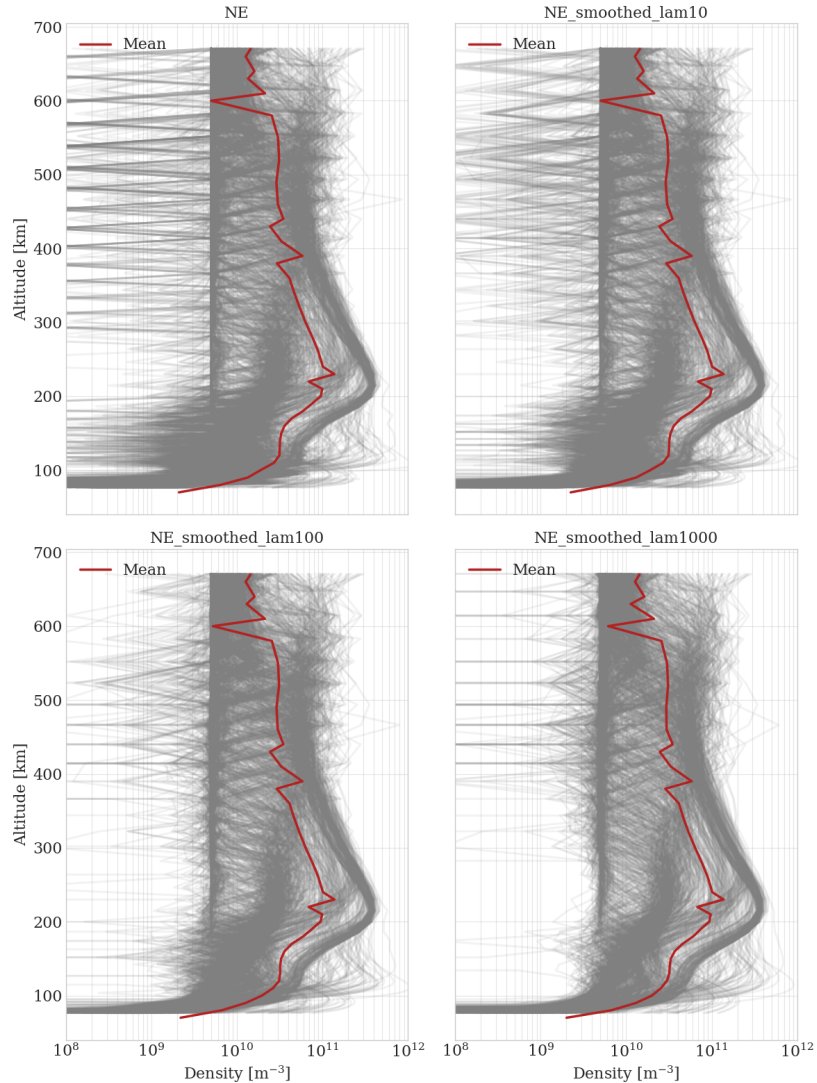


Figure 4.4: The figure shows random samples of electron density profiles, from no smoothing on the upper left, with increasing smoothing parameters towards right.

A more sophisticated data-driven approach involves training a dedicated Autoencoder to learn a low-dimensional representation of the electron density profiles. It compresses the 42-point input profile into a 6-neuron latent space through convolutional and fully connected layers. The resulting decoded 42-point output profile should retain the most important features of the input profiles, while removing the noise. We also add four neurons for cyclic parameters in the input and latent layers, such as $\cos(\text{TOD})$ and so on, to give the Autoencoder diurnal and seasonal context. Figure 4.5 shows a comparison

between Autoencoder smoothed and raw UHF profiles.

Despite the impressive visual performance of the Autoencoder, we ultimately choose not to use it for the final training pipeline. Pre-processing the ground truth labels with a neural network adds another layer of uncertainty and complexity to our attempted solution to the posed problem. Instead, we opt for a more mathematical rigorous and elegant solution: leveraging the measurement uncertainty directly.

4.3.2.1 Final Configuration: Variance-Weighted MSE

Since every EISCAT data point is accompanied by its standard deviation σ , we leverage it as a weighing factor in the loss function. This allows for the model to learn from raw data, penalizing data points according to their uncertainties. We design a *Variance Weighted MSE* loss function. By weighting using $\frac{1}{\sigma^2}$, we ensure that highly uncertain measurements contribute less to the gradient update. This allows the model to ignore the noisy data points, and eliminates the need for filtering the data.

Preliminary experimentation revealed that the network did not utilize the input electron density feature N_e . To enforce physical consistency, we introduced a penalizing factor α to contribute to the loss term from the altitude of the input N_e . We emphasise that it is multiplicative and not additive, ensuring that the loss does not increase if the input N_e is highly uncertain.

The final loss function for a batch of size M is defined as:

$$\mathcal{L}_{\text{batch}} = \frac{1}{M} \sum_{m=1}^M \left[\frac{1}{N} \sum_{i=1}^N \frac{W_i^{(m)}}{(\sigma_i^{(m)})^2} (y_i^{(m)} - \hat{y}_i^{(m)})^2 \right] \quad (4.1)$$

where $N = 42$ is the profile length. The penalty weight $W_i^{(m)}$ is defined piece-wise:

$$W_i^{(m)} = \begin{cases} \alpha, & \text{if } i = j^{(m)} \\ 1, & \text{otherwise} \end{cases}$$

Here, $y_i^{(m)}$ and $\hat{y}_i^{(m)}$ represent the true and predicted electron density at altitude index i , and $\sigma_i^{(m)}$ is the measurement uncertainty. The penalizing parameter α anchors the predicted output to the known input value. We choose to use the epoch-average batch loss $\mathcal{L}_{\text{batch}}$ as the epoch loss.

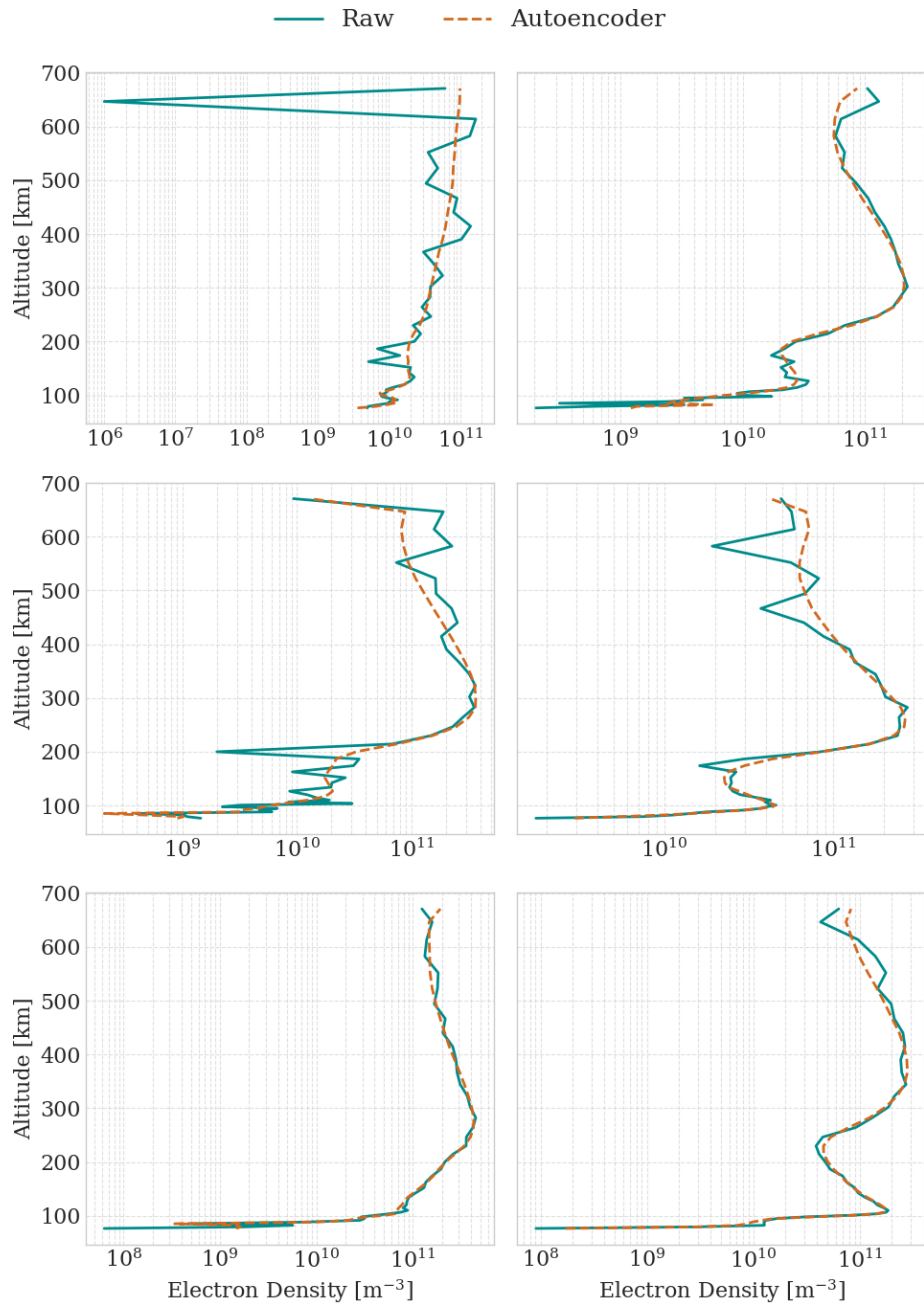


Figure 4.5: Comparison of raw UHF electron density profiles (teal) and the reconstructed profiles from the Autoencoder (orange).

4.3.3 Training and Evaluation

The model is trained using the AdamW optimizer (Loshchilov et al., 2017), and we employed a learning rate of 1×10^{-3} , and a weight decay factor of 1×10^{-2} .

We conducted a hyperparameter sweep on batch sizes ranging from 8 to 8192. The smaller batches generally improved on generalization, but had longer training times. An effective batch size of 32 is selected as the optimal trade-off between convergence speed and model performance.

For comparative evaluation between model configurations, we utilize the standard Weighted MSE, i.e., $\alpha = 1$ in Equation 4.1.

4.4 Joule Heating Prediction

This section outlines the assumptions and methodology used to predict electron density profiles, followed by the calculations for Pedersen conductance and Joule heating.

4.4.1 Electron Density Profile Predictions

The trained model outputs an electron density profile vector of length 42 for each input feature vector. Each of the elements in such a vector corresponds to the specific altitude gates. We define this altitude grid for the predictions as the mean altitude profile derived from the curated UHF dataset. This results in a vector spanning the magnetic field over the altitude range [79, 600+] km, with increasing vertical span for larger altitudes.

4.4.2 Calculation of Ionospheric Pedersen Conductance

To calculate Pedersen conductivity, given by Equation 3.9, sufficient assumptions about the atmospheric constituents are necessary. We assume a three-species neutral atmosphere consisting of atomic oxygen O, molecular oxygen O₂ and molecular nitrogen N₂. This assumption is tenable as trace constituents (e.g., Ar and He) generally possess densities several orders of magnitude lower than the primary constituents of the E- an F- region (Kelley, M.C., 1989). Implicitly, the ionospheric model assumes O⁺, O₂⁺, N₂⁺ and NO⁺ to be the primary ion constituents. N⁺ is excluded due to its negligible abundance relative to the other ion constituents.

We employ global empirical models for estimating atmospheric constituent density and composition. For the neutral atmosphere, we consider the Mass Spectrometer and Incoherent Scatter (MSIS) radar model developed by US Naval Research Laboratory (NRL), specifically NRLMSISE-00 (Picone et al., 2002). Relative ion densities are retrieved from the International Reference Ionosphere (IRI) model using the Github repository by Ilma (2024). To preserve quasi-neutrality, total ion density is scaled to match the predicted electron density ($N_i = N_e$). Electron, ion and neutral temperatures from the IRI model are also considered for collision frequency calculations. Finally, we employ the International Geomagnetic Reference Field (IGRF) to obtain geomagnetic field strength estimates using the Github repository by Laundal (2025).

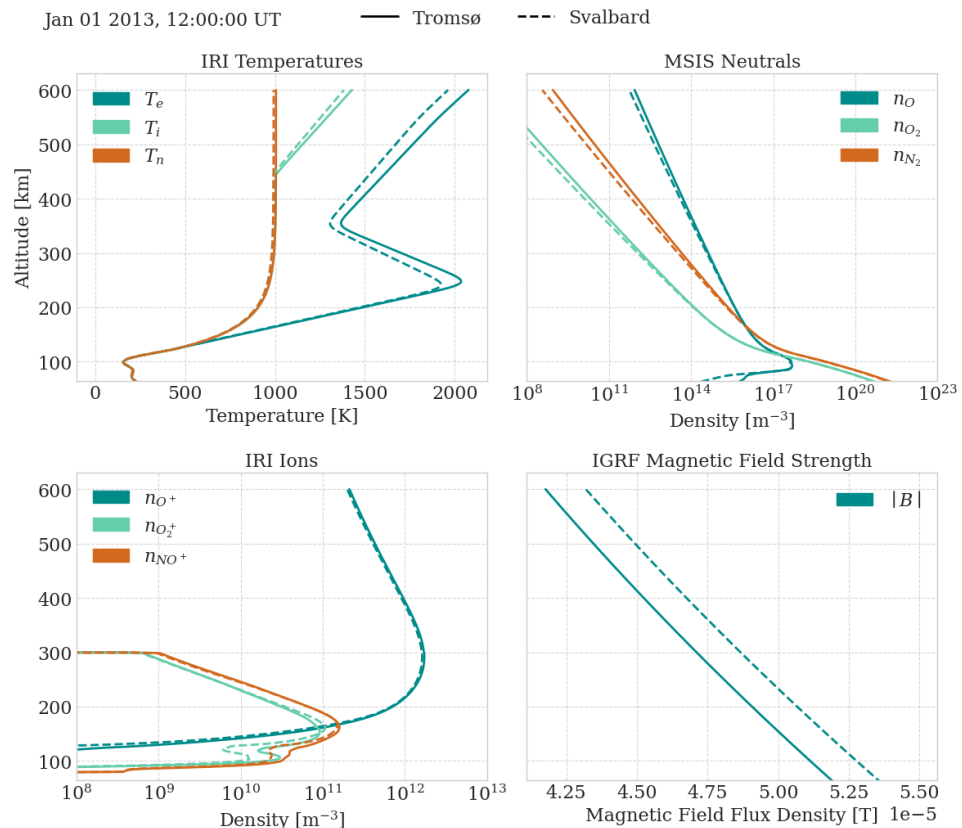


Figure 4.6: Comparative plot illustrating the variation in atmospheric and ionospheric parameters between Tromsø (solid lines) and Svalbard (dashed lines) latitudes. The upper left plot shows IRI ion, electron and neutral temperatures T_n , T_e and T_i , the upper right shows MSIS neutral constituent densities n_O , n_{O_2} and n_{N_2} , the lower left show IRI ion constituent densities n_{O^+} , $n_{O_2^+}$ and n_{NO^+} (scaled by N_e), and, finally, the lower right shows IGRF magnetic field flux density $|B|$. Note that $n_{N_2^+}$ is not included in the lower left plot as its density is negligible.

To reduce computation time, we make the assumption that the ionospheric and geomagnetic conditions (except electron density) are spatially invariant along both UHF and VHF radar beams. Figure 4.6 illustrates the variation in IRI, MSIS and IGRF between Tromsø and Svalbard latitudes. Although discrepancies exist, this approximation allows for a increased efficiency for the processing of large datasets. Note that $n_{N_2^+}$ is not included in the lower left plot as its density is negligible, but it must be considered when assessing the chemical reaction budgets of the ionospheric region.

Collision frequencies for ions (ν_i) and electrons (ν_e) are calculated by Equation 3.3. For non-resonant ion-neutral interactions, we consider $\nu_{in} = C_{in}N_n$, utilizing the coefficients C_{in} provided in Table B.1 in Appendix B. Table B.2 and Table B.3 displays the momentum transfer collision frequencies we use for the resonant ion-neutral and electron-neutral interactions, respectively.

While it is common to simplify the conductivity equation by ignoring the electron term when $\nu_e \ll \omega_{ce}$ (Schunk and Nagy, 2009b), this assumption breaks down at lower altitudes.

Figure 4.7 demonstrates in the middle right plot that for altitudes below approximately 100 km, ν_e becomes comparable to the electron gyrofrequency ω_{ce} . By neglecting the electron contribution, we may introduce conductivity errors spanning three orders of magnitude in the lower E-region, as demonstrated in the upper left plot. We therefore consider the complete expression for the Pedersen conductivity, given by Equation 3.9.

We emphasise that the Pedersen conductivity is maximized for the altitude where ion gyro- and collision frequencies reaches similar magnitudes, but also reaches significant values for where the electron gyro- and collision frequencies coincide. This is a consequence of the physics discussed in Subsection 3.2.1.

Pedersen conductance Σ_P is obtained through field-line integration of the conductivity profiles. By employing trapezoidal integration, we account for the non-uniform spatial distribution of measurements along the beam.

4.4.3 Calculation of Joule Heating

By the assumption of a stationary neutral atmosphere, we calculate Joule heating by Equation 3.17, where E'_{\perp} is the electric field perpendicular to the magnetic field in the frame of reference of the neutral gas, and Pedersen conductivity σ_P . Similar to van Hazendonk et al. (2024), we estimate the

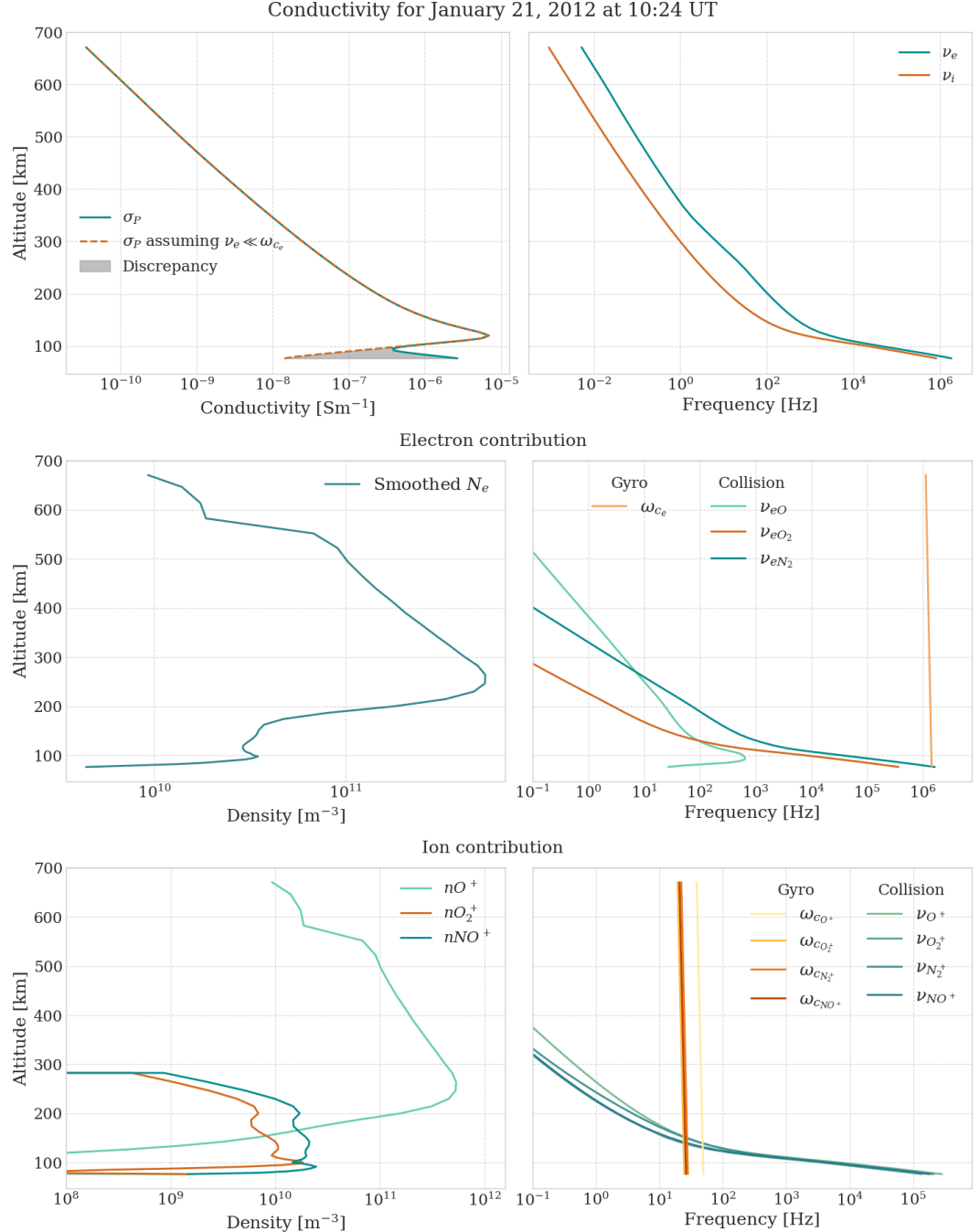


Figure 4.7: The figure shows plots in relation to conductivity calculations. The upper left plot shows the difference between the Pedersen conductivity σ_P with and without electron contribution. The upper right plot shows the comparison of the total electron-neutral and ion-neutral collision frequencies ν_e and ν_i , respectively. The second row shows the electron contribution, with the plot on the left being a neural network smoothed electron density N_e profile. The plot on the right shows a comparison of the electron-neutral collision frequencies ν_{en} compared to the electron gyrofrequency ω_{ce} . The lower row shows the ion contribution, with the leftmost plot showing the ion density profiles for O^+ , O_2^+ and NO^+ . The rightmost plot shows the comparison of ion-neutral collision frequencies ν_{in} and ion gyrofrequencies ω_{ci} . Note that the conductivity is maximised where the ion gyro- and collision frequency coincide. Also note that the largest discrepancy in the upper left plot occurs when electron-neutral collision frequencies and electron gyrofrequency are similar in magnitude.

magnitude of perpendicular electric field $|E'_\perp|$ by $|E'_\perp| = |V_{\text{LOS}}|B$, where V_{LOS} is the ion LOS velocity as measured by the ISR, and B is the magnitude of the magnetic field flux density as obtained from IGRF.

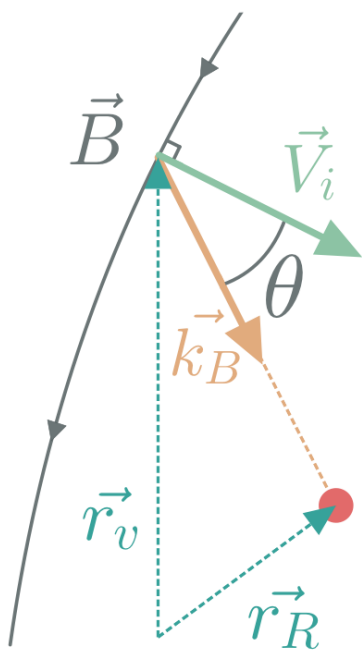


Figure 4.8: Schematic of how the radar measures the ion velocity, with the pink dot as the radar site. The grey arrowed line indicates the geomagnetic field \mathbf{B} , the green arrow is the ion velocity vector \mathbf{V}_i , the yellow arrow is the Bragg vector \mathbf{k}_B , and θ is the angle between the two. The two blue dashed lines indicate the volume and radar vector from the center of the Earth, denoted \mathbf{r}_v and \mathbf{r}_R , respectively.

However, the intersection between the radar beam and geomagnetic field lines is non-orthogonal, due to the elevation of the radar and the angle of the geomagnetic field. Figure 4.8 shows an idealized schematic of how the radar beam measures V_{LOS} . The grey arrowed line is the geomagnetic field line, the green arrow is the ion velocity \mathbf{V}_i perpendicular to the geomagnetic field, the yellow arrow is the Bragg vector \mathbf{k}_B , and the two blue lines \mathbf{r}_v and \mathbf{r}_R indicate the vectors from Earth's center to the radar volume and site. Lastly, the pink circle indicates the radar site. The angle θ is the angle discrepancy between \mathbf{k}_B and \mathbf{V}_i . The Bragg vector \mathbf{k}_B is defined by:

$$\mathbf{k}_B = \frac{4\pi}{\lambda_R} \hat{\mathbf{k}}_B \quad (4.2)$$

where the unit Bragg vector $\hat{\mathbf{k}}_B$ is defined by:

$$\hat{\mathbf{k}}_B = \frac{\mathbf{r}_R - \mathbf{r}_v}{|\mathbf{r}_R - \mathbf{r}_v|} \quad (4.3)$$

It is possible to decompose the ion velocity \mathbf{V}_i into its north and east components:

$$\mathbf{V}_i = V_{ni} \hat{\mathbf{n}} + V_{ei} \hat{\mathbf{e}} \quad (4.4)$$

where V_{ni} and V_{ei} are the north- and eastward components of V_i , and $\hat{\mathbf{n}}$ and $\hat{\mathbf{e}}$ are the north- and eastward unit vectors. The Doppler shift of the ion line can be expressed by:

$$\omega_{\text{LOS}} = \mathbf{k}_B \cdot \mathbf{V}_i = \mathbf{k}_B \cdot \hat{\mathbf{n}} V_{ni} + \mathbf{k}_B \cdot \hat{\mathbf{e}} V_{ei} \quad (4.5)$$

The last term in Equation 4.5 evaluates to zero, as for VHF measurements, \mathbf{k}_B has no component in the eastward direction. The Doppler shift ω_{LOS} therefore

evaluates to:

$$\omega_{\text{LOS}} = \mathbf{k}_B \cdot \hat{\mathbf{n}} V_{ni} \quad (4.6)$$

Additionally, from Figure 4.8, we can make the geometric argumentation that:

$$\mathbf{k}_B \cdot \hat{\mathbf{n}} = \frac{4\pi}{\lambda_R} \sin \theta \quad (4.7)$$

Using Equation 4.7, we can approximate the Doppler shift in the northward direction ω_{LOS} to be:

$$\omega_{\text{LOS}} \approx \frac{4\pi}{\lambda_R} V_{ni} \sin \theta \quad (4.8)$$

Finally, using Equation 3.20, we can define the ion velocity in the northward direction V_{ni} to be:

$$V_{ni} = \frac{\omega_{\text{LOS}} \lambda_R}{4\pi \sin \theta} = \frac{V_{\text{LOS}}}{\sin \theta} \quad (4.9)$$

Thus, we use the ion LOS velocity as measured from the radar to calculate a lower bound of the electric field $\hat{E}'_{\perp L}$ by:

$$\hat{E}'_{\perp L} = \frac{V_{\text{LOS}}}{\sin \theta} B \quad (4.10)$$

since we only consider ion motion in the northward direction. Ion motion perpendicular to the Bragg vector will not be captured by the radar. It is not tenable to assume that the east-west ion velocity component is negligible, which is why we state this as the lower bound electric field magnitude.

V_{LOS} contains a significant amount of noise, especially at greater altitudes due to low Signal-to-Noise Ratio (SNR), an example of which can be seen in Panel 4 in Figure 6.1. As we evaluate Joule heating using the magnitude of V_{LOS} , the noise will cause unphysically high Joule heating rates, especially at higher altitudes. To mitigate this, we unbias the calculation by considering

$$E'_{\perp L} = \hat{E}'_{\perp L} + \xi \quad (4.11)$$

where $\hat{E}'_{\perp L}$ is given by Equation 4.10, and $\xi = \sigma_{\hat{E}'_{\perp L}} = \frac{\sigma_{V_{\text{LOS}}}}{\sin \theta} B$, in which $\sigma_{V_{\text{LOS}}}$ refers to the standard deviations from the radar measurements of V_{LOS} . We can use this lower bound of the electric field to calculate a lower bound of the Joule heating rates using Equation 3.17:

$$q_L = \sigma_P \left(\hat{E}'_{\perp L} + \xi \right)^2 = \sigma_P \left(\hat{E}'_{\perp L}^2 + 2\hat{E}'_{\perp L}\xi + \xi^2 \right) \quad (4.12)$$

We assume the random variable ξ to be normally distributed i.e., $\xi \sim \mathcal{N}(0, \sigma_{\hat{E}'_{\perp L}}^2)$, and it follows that $\langle 2\hat{E}'_{\perp L}\xi \rangle = 0$. Consequently, Equation 4.12 can be written as

$$q_L = \sigma_P \left(\hat{E}'_{\perp L}^2 + \xi^2 \right) \quad (4.13)$$

We may use Equation 4.13 to express the lower bound unbiased Joule heating rate q_{UL} by using and $\langle \xi^2 \rangle = \sigma_{\hat{E}'_{\perp L}}^2$:

$$q_{UL} = q_L - \beta \sigma_P^2 \sigma_{\hat{E}'_{\perp L}}^2 \quad (4.14)$$

where q_L is expressed by Equation 4.13, and β is a scaling parameter for the standard deviation term. We try to mitigate the noise from V_{LOS} measurements degrading Joule heating estimates by accounting for the standard deviations of the parameter measurements. Please note that σ_P refers to the Pedersen conductivity and $\sigma_{\hat{E}'_{\perp L}}$ is the standard deviation of the electric field.

With Equation 3.17 and Equation 4.14, we obtain the altitude profile of the Joule heating rates q_L and q_{UL} , respectively, evaluated at the same altitudes as the electron density and Pedersen conductivity. We calculate the height-integrated Joule heating rates Q_L and Q_{UL} , using the same trapezoidal integration method as previously mentioned.

/ 5

Results

In this chapter, we present the results obtained from the trained Fully Connected Neural Network (FCNN). We first detail the hyperparameter selection process and the training dynamics, before evaluating the model's performance on the unseen test set. Finally, we present a comparison of derived conductances using predicted profiles versus autoencoder smoothed and raw radar data.

5.1 Model Selection and Training

To identify the optimal model architecture, we perform manual grid search on two key hyperparameters: the dropout rate p and penalty factor α . We constrain the search space to $\alpha \in [10, 50, 100]$ and $p \in [0.20, 0.30]$, and calculate the variance weighted MSE loss (with $\alpha = 1$) for each trained model. The configuration with $\alpha = 50$ and $p = 0.20$ minimizes the loss with a validation set loss of ~ 0.0106 . We use this model configuration for all subsequent analysis.

Figure 5.1 shows the training and validation loss curves for this optimal model. The model reaches its validation loss minimum at epoch 32. For the subsequent 18 epochs (not shown), the validation loss increases, indicating the onset of overfitting. By restoring the model weights from epoch 32, we effectively employ early stopping as a regularization technique. Note that the loss values in Figure 5.1 includes the penalty term $\alpha = 50$, whereas the validation loss

used for comparison between models uses $\alpha = 1$.

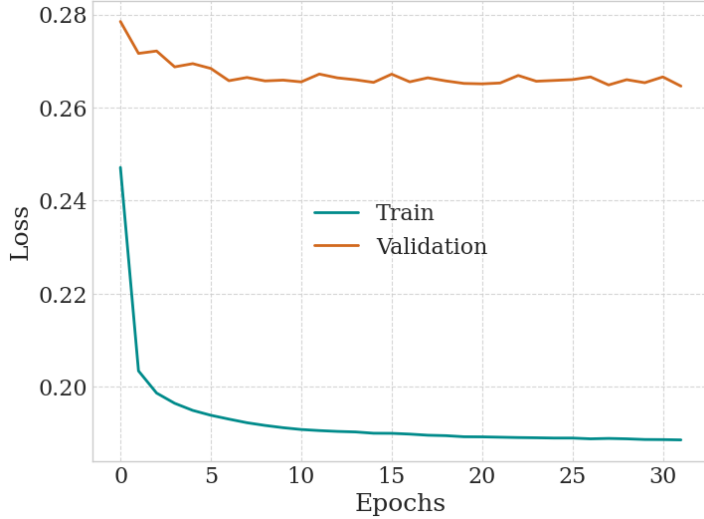


Figure 5.1: Training (blue) and validation (orange) loss curves for the model configuration with $\alpha = 50$ and $p = 0.20$. The model was trained for 50 epochs, but reached its minimum at epoch 32. The remaining 18 epochs are not shown.

5.1.1 Electron Density Prediction

The generalization performance of the FCNN model is evaluated using the unseen test set. The model achieved a global WMSE (computed with $\alpha = 1$) of 0.0095, slightly outperforming the validation loss observed in the grid search (0.0106). This indicates that the model has generalized well without overfitting.

The coefficient of determination (R^2) for the test set evaluates to ~ 0.73 . Usually, values closer to 1 are preferred, as that indicates the model explains all variability in the ground truth data. However, in the context of noisy ISR data, the FCNN should not explain all the ground truth variability, as that would indicate that the model has learned the noise patterns too. A theoretical model that perfectly predicts electron density profiles, would still yield an $R^2 < 1$. Thus, our model seems to capture aspects of the physics of the ionosphere, while filtering out the high-frequency measurement noise.

Figure 5.2 presents a randomized set of predicted and associated ground truth profiles from the test set. The blue solid lines represent the ground truth, while the orange dashed lines represent the FCNN predictions. The grey marker indicates the single local electron density point provided as input to the

model.

Qualitatively, the model demonstrates a robust ability to reconstruct the full altitude profile from limited input. A notable characteristic of the model is that it functions as a intelligent non-linear filter. In cases where the true profile exhibits significant noise or outliers (e.g., the plots in the center column), the network predicts a smooth, physically realistic profile. This suggests the model has learned the underlying physical morphology of the field-aligned density rather than simply memorizing noise patterns.

To evaluate the field aligned consistency of the model, we calculate the WMSE as a function of altitude, averaged over the entire test set. The resulting field aligned WMSE profile is shown in figure 5.3.

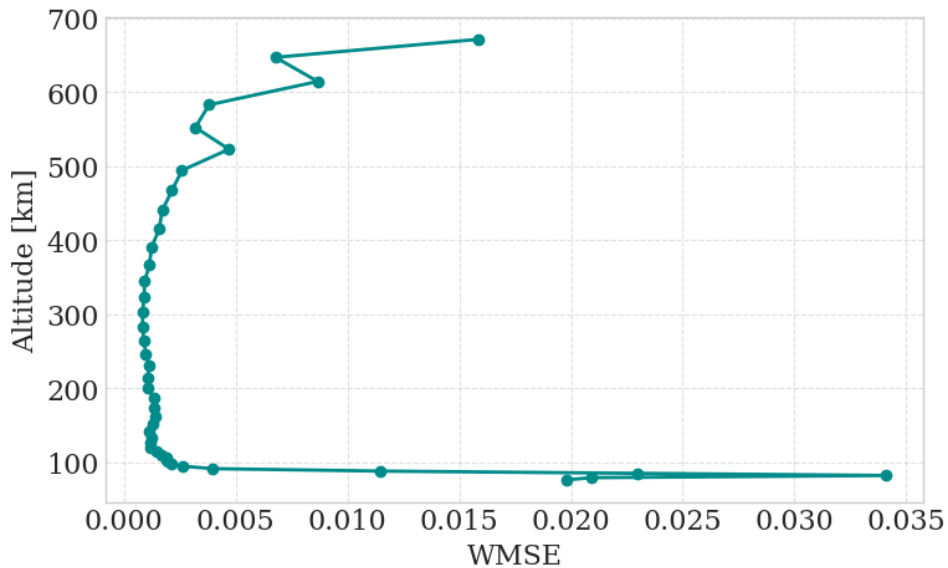


Figure 5.3: Field aligned profile of the WMSE (computed with $\beta = 1$) calculated over the test set. The model shows highest accuracy in the F-region (150-500 km), and reduced performance in the low-altitude E-region and high-altitude topside ionosphere.

The WMSE profile exhibits a distinct altitude dependency, as the lower and higher altitudes show greater loss values. The model performs optimally in the F-region (approximately 150-500 km), where the WMSE remains consistently low. This altitude range corresponds to the region of greatest electron densities and typically highest SNR in the radar data.

In the topside ionosphere (> 500 km) and in the lower E- and D-regions (< 100

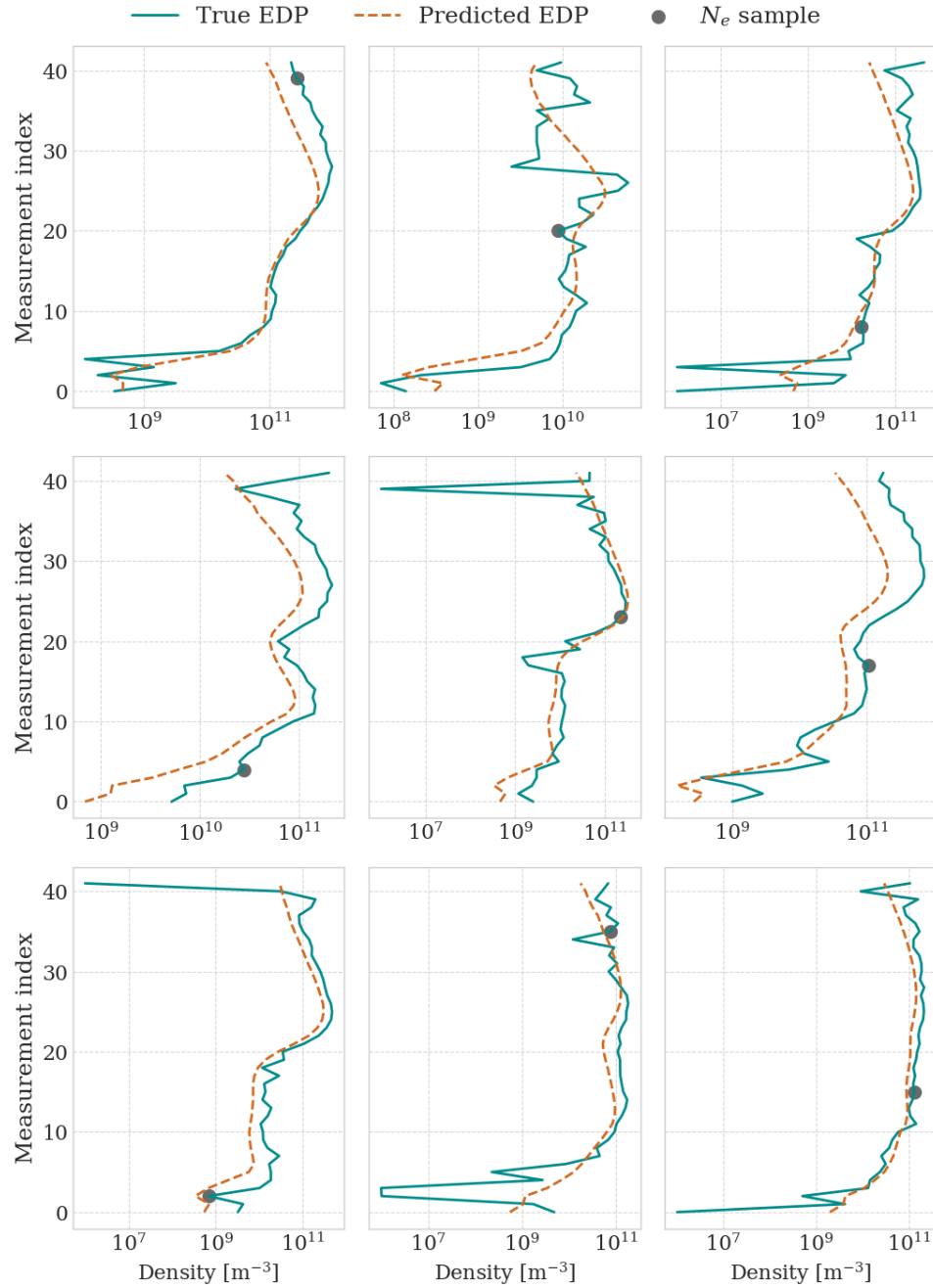


Figure 5.2: Comparison of the measured (blue) and predicted (orange) electron density profiles. The grey scatter point on each plot indicates the single electron density point that the model is fed during prediction.

km), the error notably increases. The reduced electron density in both altitude ranges causes the SNR to decrease, which may be one reason why the WMSE is larger. E-region electron densities are also dominated by sporadic ionization events (Brekke, 2012), which does not necessarily correlate with the F-region physics. The increased errors indicate that the current model architecture or the dataset, captures the dominant F-region physics more effectively than the distinct dynamics of the lower and upper ionosphere.

5.2 Pedersen Conductance Comparison

To test the physical validity of the model, we compare the field-line integrated Pedersen conductances Σ_P derived from (1) FCNN-predicted electron density profiles, (2) Autoencoder-Smoothed (AS) profiles, and (3) raw ISR profiles. The comparison is conducted on a small subset of the test set, comprising 42,000 individual samples. For all three cases, we compute Σ_P using the methodology described in Subsection 4.4.2.

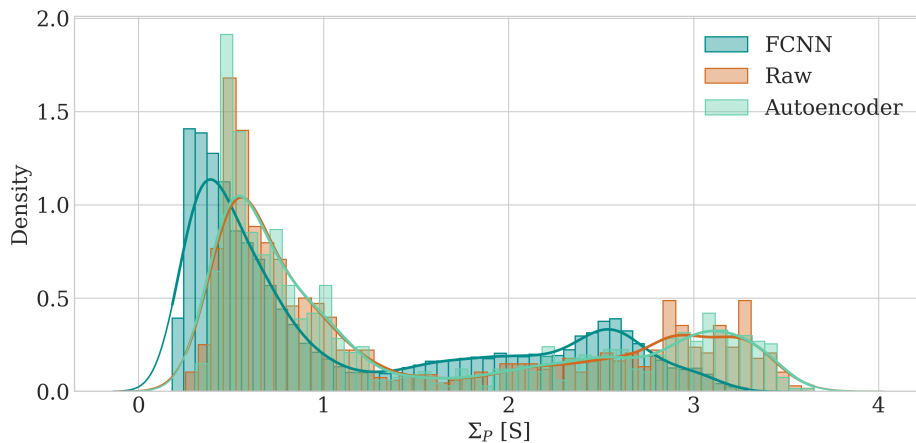


Figure 5.4: Histogram of Pedersen conductance Σ_P computed using FCNN-predicted profiles (dark blue), raw ISR ground truth profiles (orange), and Autoencoder-smoothed electron density profiles (light blue).

Figure 5.4 shows a comparison of the distributions of the derived conductances. The distribution for the raw (orange) and AS (light blue) displays a high correlation, indicating that the Autoencoder effectively retains the electron density information while reducing noise. The histogram for the FCNN (darker blue) displays a systematic shift of Σ_P towards lower magnitudes compared to the raw and AS distributions. The distributions of Σ_P based on the raw and AS

electron density profiles are almost identical, with only small differences for larger values.

To quantify the correlation between the three methods, we analyze the correlation between the their derived conductances. Figure 5.5 presents three correlation plots: the upper two compare the FCNN Σ_P against the raw and AS Σ_P , respectively, while the lower plot compares the raw versus the AS Σ_P . The orange line indicates the linear fit. The lower plot displays a strong linear relationship between the raw and AS profiles, indicating that the Autoencoder reliably denoises the electron density profiles.

Comparisons involving the FCNN showcase vertical striation patterns. These are not model errors, but rather a consequence of the training data architecture described in Subsection 4.2.2. Each electron density profile is used as the label for 42 different feature vectors, each from a different altitude. Thus, for a batch of 42 samples, Σ_P from raw or AS profiles remain constant, while the FCNN produces slightly varying values of Σ_P depending on which local altitude input it is provided with. These are artifacts of the training data architecture. This results in the vertical structures we observing, and is a manifestation of how the FCNN predicts slightly different electron density profiles for different altitudes of the input parameter. We also observe that the FCNN consistently predicts lower conductance values than the Autoencoder and raw values. However, for values of $\Sigma_P \in [0, 1]$, we observe that some raw and AS values are lower than the FCNN values.

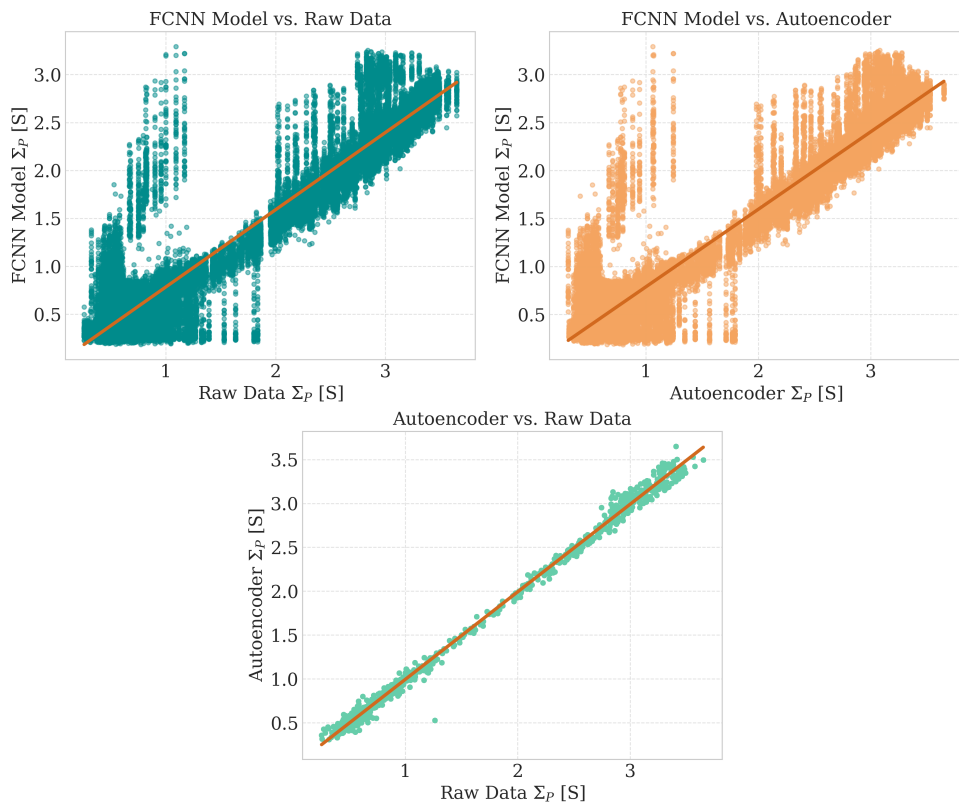


Figure 5.5: Correlation plots of conductances computed using FCNN predicted, autoencoder smoothed and ground truth electron density profiles. From left to right, the plots show the correlation of the FCNN and the ground truth, the FCNN and the autoencoder, and the ground truth and autoencoder. The light orange line is the linear fit of the correlation scatter plot. Vertical structures can be seen in the center and leftmost plot. This is caused by our label architecture, as each label is used 42 times.

/ 6

Discussion

In this chapter, we demonstrate the application of the neural network by employing it to two independent case studies derived from EISCAT VHF measurements. The two cases are characterized by contrasting geophysical conditions; a geomagnetically quiet period and an active storm event. Following the case studies, we provide a critical evaluation of the proposed methodology with emphasis on its physical validity, limitations, and coherence with existing literature. Finally, we outline potential applications and future directions for this framework.

6.1 VHF Case Studies

To assess the model's ability to generalize and its physical consistency, we analyze two distinct 24h experiment campaigns conducted using the VHF radar. In contrast to the UHF data which was filtered for field-aligned measurements, the VHF radar operates at a low elevation angle of 30°.

For both events, we process the data in the following fashion; the FCNN predicts complete field-aligned electron density profiles (\hat{N}_e) based on the scalar electron density inputs (N_e) along the oblique VHF beam, following the method described in Subsection 4.4.1. Next, we utilize the predicted \hat{N}_e profiles to compute field-aligned profiles of Pedersen conductivity σ_P and the field-line integrated Pedersen conductance Σ_P using the procedure detailed in

Subsection 4.4.2. Finally, we calculate altitude resolved and field-line integrated Joule heating rates q and Q by combining the conductivity profiles with ion LOS velocity measurements V_{LOS} from ISR in accordance with the described method in Subsection 4.4.3.

Unless stated otherwise, all temporal data in the following sections are presented in Coordinated Universal Time (UTC). The local time at the EISCAT Ramfjordmoen site corresponds to UTC+1 (Central European Time) or UTC+2 (Central European Summer Time), depending on the season.

6.1.1 Quiet Time Case Study

For the quiet time case study, we selected an observational period from January 24–25, 2017. This period is biased towards solar minimum and low geomagnetic activity, while also aligning with the season of the year most heavily represented in the UHF training data.

The measured plasma parameters electron density N_e , electron temperature T_e , ion temperature T_i and ion LOS velocity V_{LOS} are shown in the upper four panels of Figure 6.1. The data exhibits expected diurnal patterns, with solar photoionization driving N_e enhancements around noon UT (Brekke, 2012). The ion velocity V_{LOS} displays distinct dynamic features between 18:00 and 06:00 UT, while also showcasing significant high-frequency noise at higher altitudes/latitudes.

The lower five panels display the following quantities: the field-line integrated predicted electron density (\hat{N}_e), derived Pedersen conductance (Σ_P), derived biased Joule heating rate (Q_L), measured ion LOS velocity standard deviation ($\sigma_{V_{\text{LOS}}}$) and the derived unbiased Joule heating rate (Q_{UL}).

It is crucial to interpret the plot geometry of the derived quantities correctly. As the look-direction of the VHF radar is obliquely North, altitude increases with latitude. Thus, the y-axis refers to the altitude and latitude of the *single input measurement point*. The color intensity of each pixel represents the *integrated* quantity derived from the field aligned profiles predicted by the FCNN based on the input at that altitude and latitude. Effectively, these plots provide a top-down view of the ionospheric slab. We emphasize that as the profiles are field-aligned and not perfectly vertical, the ionospheric volume we look at is rather a parallelogram than a rectangular shape. We do not account for this geometry in the plots shown here, simplifying the volume to a rectangular shape for visualization purposes.

The integrated predicted density \hat{N}_e (Panel 5) reproduces the diurnal solar cycle

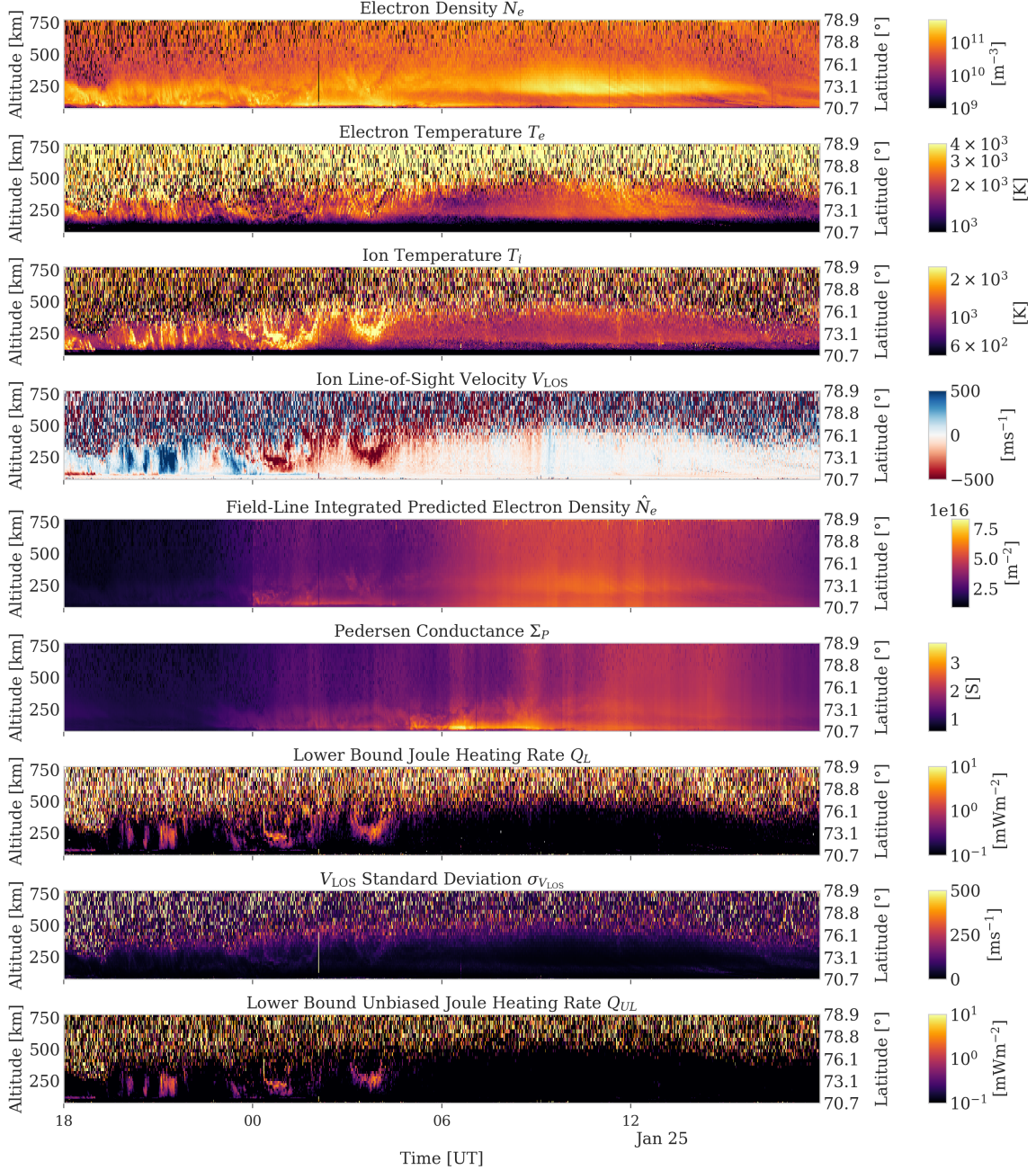


Figure 6.1: Overview of the quiet time case study (January 24–25, 2017). **Panel 1–4:** Measured Electron Density N_e and Temperature T_e , Ion Temperature T_i and LOS Velocity V_{LOS} from the EISCAT VHF radar. **Panel 5:** Field-Line Integrated Electron Density \hat{N}_e predicted by the FCNN. **Panel 6:** Derived Field-Line Integrated Pedersen Conductance Σ_P . **Panel 7:** Lower Bound Biased Joule Heating Rate Q_L . **Panel 8:** Standard Deviation of the ion LOS velocity measurement $\sigma_{V_{\text{LOS}}}$. **Panel 9:** Lower Bound Joule Heating Rate Q_{UL} calculated using $\beta = 30$. Note that for panels 5–9, the y-axis represents the altitude, and corresponding latitude, of the *input* measurement along the oblique VHF beam.

accurately. A faint horizontal band of low integrated density appears when inputs are taken from 150–200 km. This likely mirrors the "valley" region often observed between E- and F-layers in the input data (Brekke, 2012). On the contrary, an enhanced band appears near ~ 250 km, corresponding to the F-region peak. The model appears to bias the entire output profile; overestimating at high N_e input magnitudes and underestimating at low ones, rather than fully resolving the altitude dependence. This may imply that the model relies more heavily on the density input than the altitude parameter.

The magnitude of the integrated \hat{N}_e is on the order of 10^{16} m^{-2} . This is consistent with Total Electron Content (TEC) derived from Global Positioning Systems (GPS) systems (Stankov et al., 2003). TEC is calculated as the integrated electron density from the ground height up to the altitude of the transmitting satellite, given in TEC Units (TECUS), which is defined as $10^{16} \text{ electrons m}^{-2}$ (Lean et al., 2016). Vertical TEC (vTEC) can range from a few to several tens of TECU depending on solar activity (Leitinger, 1998). The values observed here, ranging between 2–7 TECU, are consistent with the low background density expected during winter around solar minimum (Lean et al., 2016).

The Pedersen conductance Σ_P (Panel 6) varies between ~ 1 at night and 2.5 during the day. A distinct enhancement reaching ~ 3 S is observed in the morning sector (06:00 UT) at lower altitudes. Through statistical analysis based on electron spectrometer measurements from DMSP satellites, Hardy et al. (1987) made estimates of the average Σ_P in the polar ionosphere due to electron precipitation. For low geomagnetic activity (quantified by the geomagnetic index $K_p=0$), they found average Pedersen conductance values to range between $\sim 0\text{--}2$ S. However, these values were predominantly observed in the midnight-dawn sector, as the model did not account for Pedersen conductivity due to solar photoionization.

The biased Joule heating rate Q_L (Panel 7) exhibits strong morphological correlation with the ion velocity V_{LOS} , which we expect since the electric field is proportional to V_{LOS} . These structures seem to produce Joule heating rates of a few mW m^{-2} . van Hazendonk et al. (2024) made estimates of the total ionospheric Joule heating caused by Ultra-Low Frequency (ULF) waves, therein also made the estimation of the base level Joule heating rate Q_L to be between $0.5 - 3 \text{ mW m}^{-2}$. Comparing the most intense events from our case study with the base line findings in van Hazendonk et al. (2024) reveals a similar magnitude in Q_L .

The unbiased Joule heating rate Q_{UL} (Panel 9) is calculated using a scaling factor of $\beta = 30$ to account for the noise variance shown in Panel 8. Due to the high magnitude of $\sigma_{V_{\text{LOS}}}$, the unbiasing term often exceeds the raw heating estimate, resulting in unphysical negative heating rates. These instances are

clipped to zero, i.e., $Q_{UL} \geq 0$. While debiasing successfully reduces the background noise (compare the dark regions of Panel 7 and 9), the high-latitude noise pattern remains visible. This is an indication that the noise in the velocity measurements is the dominant source of uncertainty in the heating estimates at high altitudes/latitudes.

To investigate the vertical structure of the predictions, we extract a cross-section of the ionosphere at a fixed timestamp, specifically $t \approx 02:32$ UT. This cross-section is presented in Figure 6.2. In this visualization, each vertical column represents a complete field aligned profile predicted by the FCNN based on the single input measurement indicated by the white scatter point.

The geometry of the VHF radar beam becomes clear; for increasing Magnetic Latitude (MLAT), the beam samples at progressively greater altitudes. For $MLAT > 74^\circ$, the input N_e is measured at altitudes approaching ~ 750 km. This exceeds the domain of the training dataset, which is bounded by the UHF radar's ceiling of ~ 600 km. Thus, for these altitudes, the FCNN is extrapolating its predictions based on feature vectors containing altitude values from outside its training distribution. Despite this, the predicted \hat{N}_e profiles remain somewhat morphologically consistent with profiles from lower MLATs. This suggests that the model has learned a robust representation of the altitude dependence, as it generalizes reasonably well beyond the training bounds.

The predicted electron density \hat{N}_e is relatively uniform across latitudes, but exhibits a significant increase near 69° MLAT. In contrast, the profiles at the very lowest MLATs exhibit lower magnitudes. This variation is likely a manifestation of the model's sensitivity to the input density scalar. As the input measurements at these lower altitudes/MLATs are smaller, they cause the network to scale down the entire output profile. The background density remains in the lower range of 10^{10} – 10^{11} m $^{-3}$, which is consistent with expected nighttime conditions (Brekke, 2012).

Pedersen conductivity profiles exhibit high stability over the MLATs. The field-aligned structure is physically realistic, with the distinct E-region peak at ~ 125 km and significant decay of several orders of magnitude in the topside ionosphere (Brekke, 2012). The magnitude of the conductivity profiles ranges from 10^{-5} at lower ionospheric altitudes, to 10^{-10} and even smaller in the upper ionosphere, which coincides with existing literature (Brekke, 2012).

Joule heating rate profiles q_L and q_{UL} displays significant latitudinal variation. As expected, the overlaid $\hat{E}'_{\perp L}$ lineplot shows its correlation with the resulting heating rates. At high MLAT, i.e., $> 73^\circ$, the estimated $\hat{E}'_{\perp L}$ showcases significant spikes. We interpret this as the manifestation of increased SNR in

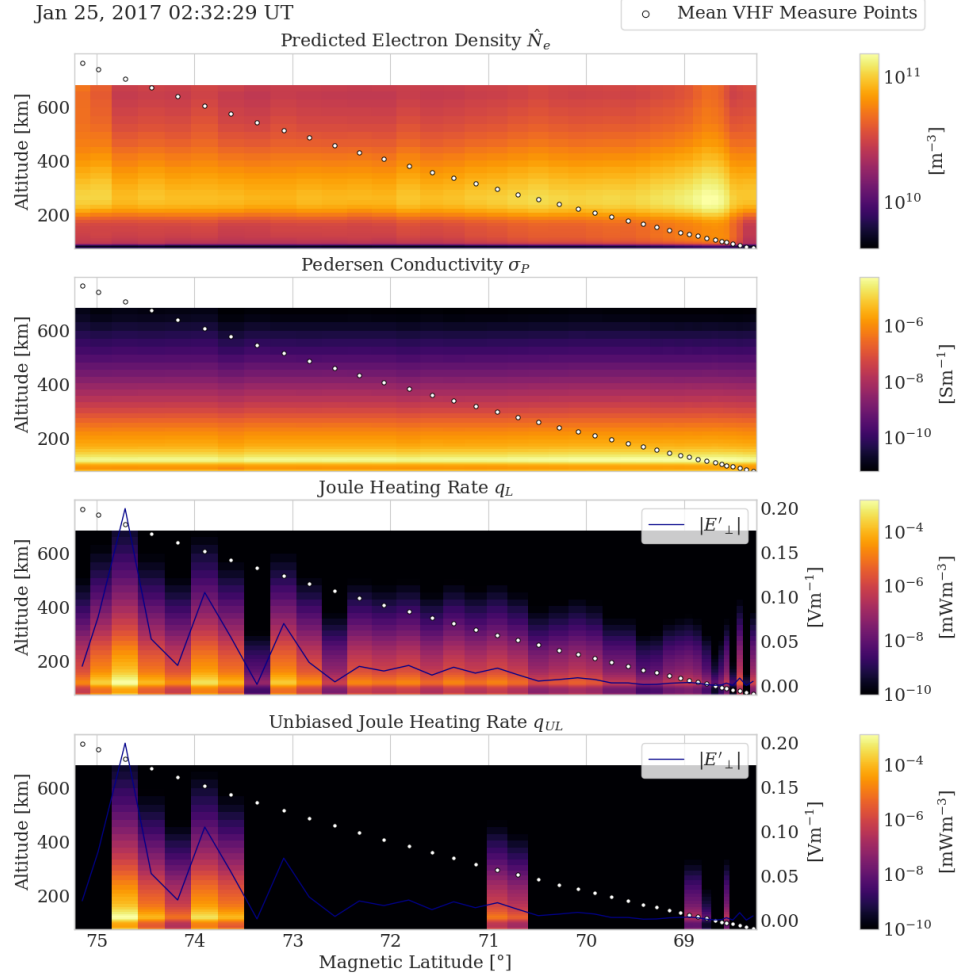


Figure 6.2: Cross-section of the ionosphere at 02:32:29 UT. The panels display from top to bottom: Predicted Electron Density Profiles \hat{N}_e , Pedersen Conductivity σ_P , Lower Bound Biased Joule Heating Rate q_L , and Lower Bound Unbiased Joule Heating Rate q_{UL} . The white scatter points indicate the altitude and Magnetic Latitude (MLAT) of the input VHF measurements used to generate each field-aligned profile. The blue line overlay on the bottom two plots represents the estimated perpendicular lower bound electric field magnitude $|E'_{\perp}|$. Laundal et al. (2024)'s dipole Github package was used for the computation of MLAT.

measurements at these altitudes rather than a more intense electric field.

The noise interpretation does not coincide with the observed unbiased heating rate q_{UL} in the bottom panel. The unbiasing algorithm is meant to suppress the heating rates at these altitudes, effectively setting them to zero. We would expect these high-altitude measurements to possess high standard deviations, and thus debiased. On the contrary, it is rather the profiles at lower altitudes/MLATs coinciding with lower values of $\hat{E}'_{\perp L}$ that are removed using this method.

To better investigate the events in a geomagnetic perspective, we present this 24-hour dataset in Magnetic Local Time (MLT) and MLAT coordinates. The data is binned azimuthally into 24 one-hour MLT bins and radially into integer MLAT steps $\in [68^\circ, \dots, 75^\circ]$. We employ the `dipole` Github package for the computation of Centered Dipole (CD) coordinates, and subsequent MLT (Laundal et al., 2024).

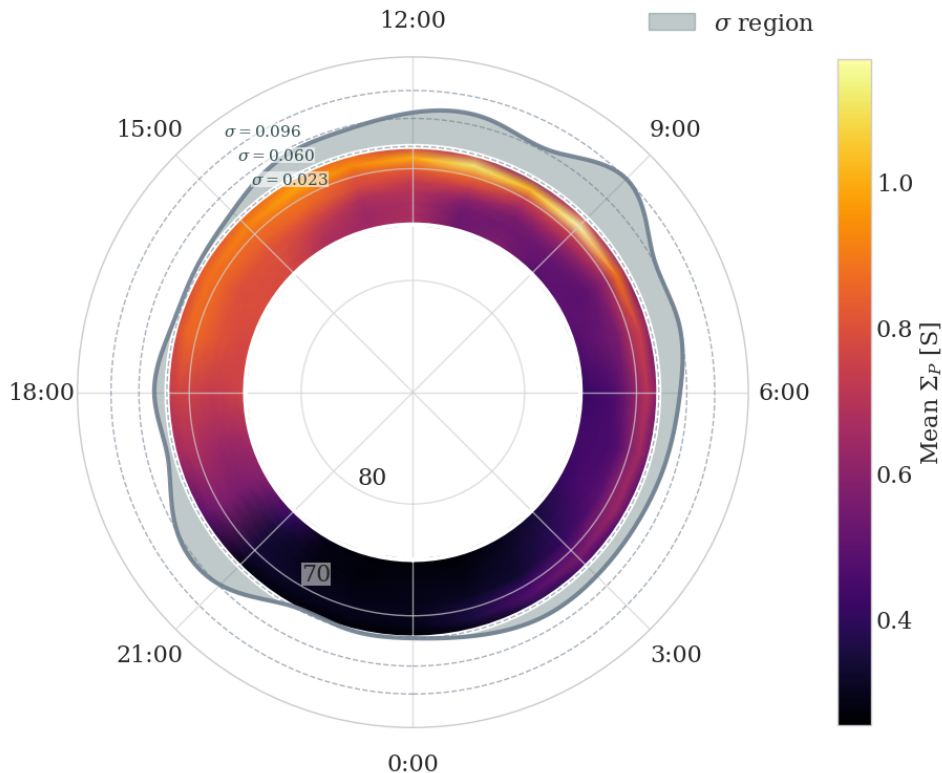


Figure 6.3: Polar projection of the mean Pedersen conductance Σ_P as a function of Magnetic Local Time (MLT) and Magnetic Latitude (MLAT). The color scale indicates the conductance. The greyshaded area bounded by the grey line indicates the temporal variation within each MLT bin. Numerical bounds are indicated on the top left.

Figure 6.3 presents the mean Pedersen conductance Σ_P in this CD coordinate system. The color map represents the mean value within each bin. We employ interpolation between the bins for smooth transitions. To visualize temporal variability, we smooth and plot the aggregated variance over MLAT for each hourly bin as the greyshaded area bounded by the grey line. The radial extent of this region is normalized to fit within the polar plot. Here, the standard deviation ranges $\in [0.023, 0.096]$ S.

The plot reveals that the greatest Pedersen conductance values coincides with the highest variability in the 09–12 MLT sector. We can compare these results with existing models. Hardy et al. (1987) observed peak conductances in the midnight-early morning sector for latitudes below 70° MLAT. Our results display almost the opposite trend with a distinct maximum near noon Local Time (LT). However, we expect this difference as the Hardy model specifically estimates the conductance caused by electron precipitation related to auroral activity (Hardy et al., 1987). In contrast, our ISR-based model includes the contribution of daytime solar photoionization of the ionosphere. During geomagnetically quiet conditions, solar radiation is the dominant ionization source (Brekke, 2012). This naturally results in peak conductances around local noon.

Figure 6.4 presents the polar distribution of the biased Joule heating rate Q_L . A pronounced gradient can be seen toward higher latitudes. As previously discussed, this feature is likely a result of high SNR in the outer range of the VHF radar beam rather than a manifestation of a physical heating event. The error propagation from the $\sigma_{V_{LOS}}$ measurement compromises the interpretability of the mean values at high latitudes. The standard deviation measure underpins this, by showcasing that the sectors with the highest apparent heating, i.e., between 18:00 – 00:00 MLT, are also the ones exhibiting highest statistical variability.

Finally, Figure 6.5 showcases the unbiased Joule heating rate Q_{UL} . While the high-latitude heating rates remain unphysically large, the range of the standard deviation is substantially diminished compared to that of Q_L . However, the morphological structure remains quite similar, making resolving heating events difficult. Thus, even the unbiased estimation of the Joule heating rates for geomagnetically quiet conditions proves difficult to determine.

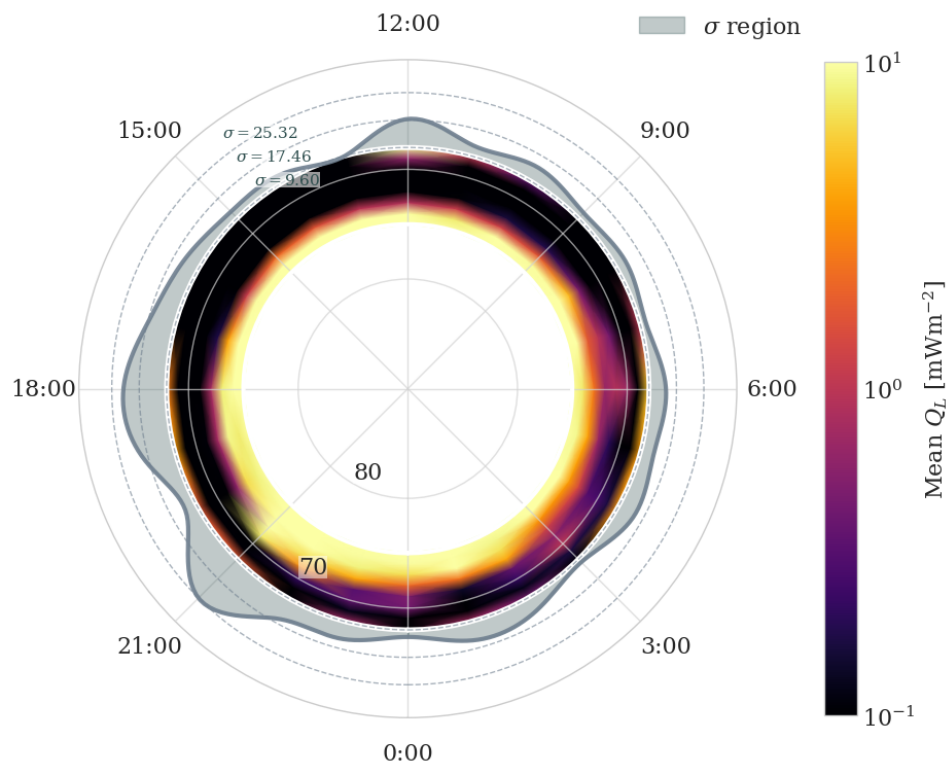


Figure 6.4: Polar projection of the mean lower bound Joule heating rate Q_L as a function of Magnetic Local Time (MLT) and Magnetic Latitude (MLAT). The color scale indicates the heating rate. The greyshaded area bounded by the grey line indicates the temporal variation within each MLT bin. Numerical bounds are indicated on the top left.

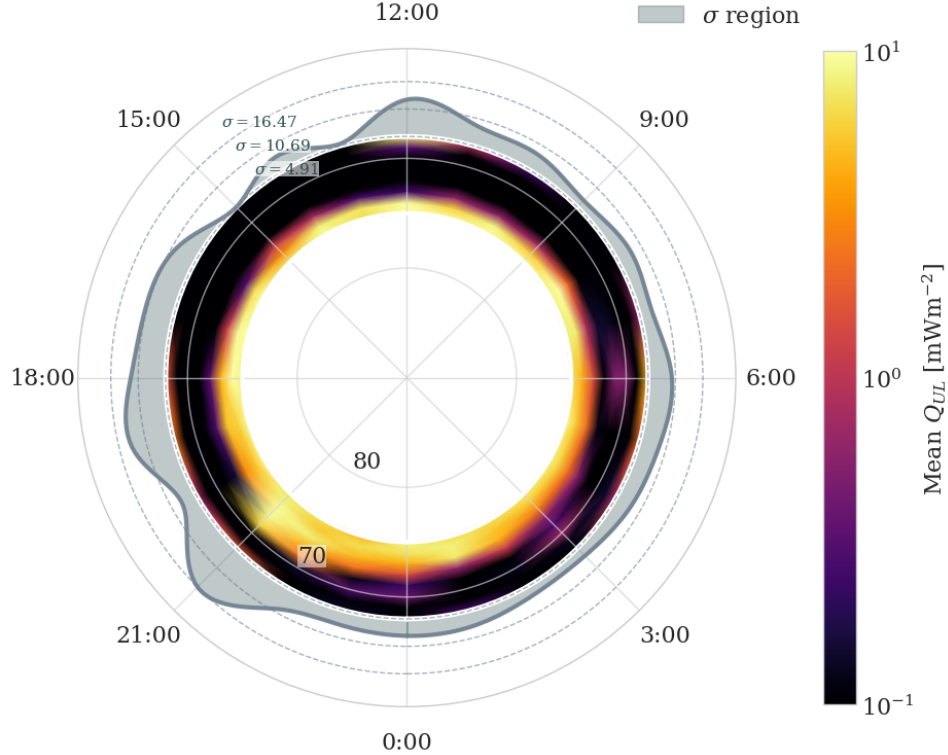


Figure 6.5: Polar projection of the mean unbiased lower bound Joule heating rate Q_{UL} as a function of Magnetic Local Time (MLT) and Magnetic Latitude (MLAT). The color scale indicates the heating rate. The greyshaded area bounded by the grey line indicates the temporal variation within each MLT bin. Numerical bounds are indicated on the top left.

6.1.2 Stormy Time Case Study

To contrast the baseline conditions analyzed in Subsection 6.1.1, we apply the FCNN to a period of intense geomagnetic activity. We select the 24-hour interval commencing at 06:00 UT on September 7, 2017. This interval covers a period of a significant geomagnetic storm, characterized by a high degree of ionospheric disturbances (Yamauchi et al., 2018). Conditions imposed by such a storm, i.e., electron precipitation and intense ionospheric electric fields, is a strong test for evaluating the model's capability to resolve complex and rapidly varying plasma dynamics.

Panels 1–4 in Figure 6.6 presents the ISR VHF plasma parameters N_e , T_e , T_i and V_{LOS} . In contrast to the quiet case, the electron density N_e exhibits high-frequency variability and complex morphological structures, such as vertical striations and localized density enhancements and depletions. Specifically, we

observe a significant density cavity around 20:00 UT.

The thermal parameters T_e and T_i exhibit distinct features that coincides with the periods of increased activity in the electron density panel. Specifically, the time periods 06:00–12:00 UT and 18:00–06:00 UT are the ones of highest activity. Notably, the ion LOS velocity also showcase intense velocity values during these time intervals, with vertical structures reminiscent of ULF waves (van Hazendonk et al., 2024). We also note that the noise in the ion LOS velocity is significantly reduced. This is most likely due to the storm-induced electron densities, effectively increasing the radar SNR.

The integrated predicted electron density \hat{N}_e (Panel 5) effectively captures the increased electron densities during the storm. The magnitudes are significantly elevated compared to the quiet case, considering the daytime magnitude ranges between 10–15 TECU, while nighttime densities reduce to ~ 5 TECU. The model successfully reproduces the density cavity observed at 20:00 UT across all latitudes/altitudes. This observation underpins the findings from the quiet time case; the model is highly sensitive to the magnitude of the input scalar N_e . However, the persistence of the depletion for higher latitudes, even where the cavity is not present in N_e , suggests that the model relies on other parameters too. For instance, the electron temperature exhibits a similar depletion as N_e , but it extends further up the VHF radar beam.

The derived Pedersen conductance Σ_P (Panel 6) reflects the heightened geomagnetic activity, surpassing 5 S around noon. That is more than double the peak values observed in the quiet case. Vertical striations are present during periods of high disturbance (21:00–06:00 UT). A faint low-conductance line can be seen spanning approximately the same period at around 150 km altitude.

The estimation of Joule heating rates demonstrates the robustness of the unbiasing methodology during periods of high SNR. We keep the same unbiasing parameter as in the quiet case, i.e., $\beta = 30$. We observe that Q_{UL} (Panel 9) preserves the fine-scale structure seen in Q_L (Panel 7), while successfully removing background noise. While in the quiet case, where the methodology zeroed out values of Q_{UL} due to low SNR, here the electric fields inferred from ion LOS velocity (Panel 4) remain strong enough to exceed the noise variance threshold. As a consequence, Q_{UL} reveals intense, resolved heating events underpinning that our unbiasing methodology can be successfully applied to periods of high geomagnetic and ionospheric activity.

To resolve the vertical structure of the storm-time ionosphere, we apply the same methodology as in Subsection 6.1.1, by analyzing a cross-section at 22:41 UT. This cross-section is presented in Figure 6.7. This timestamp is characterized

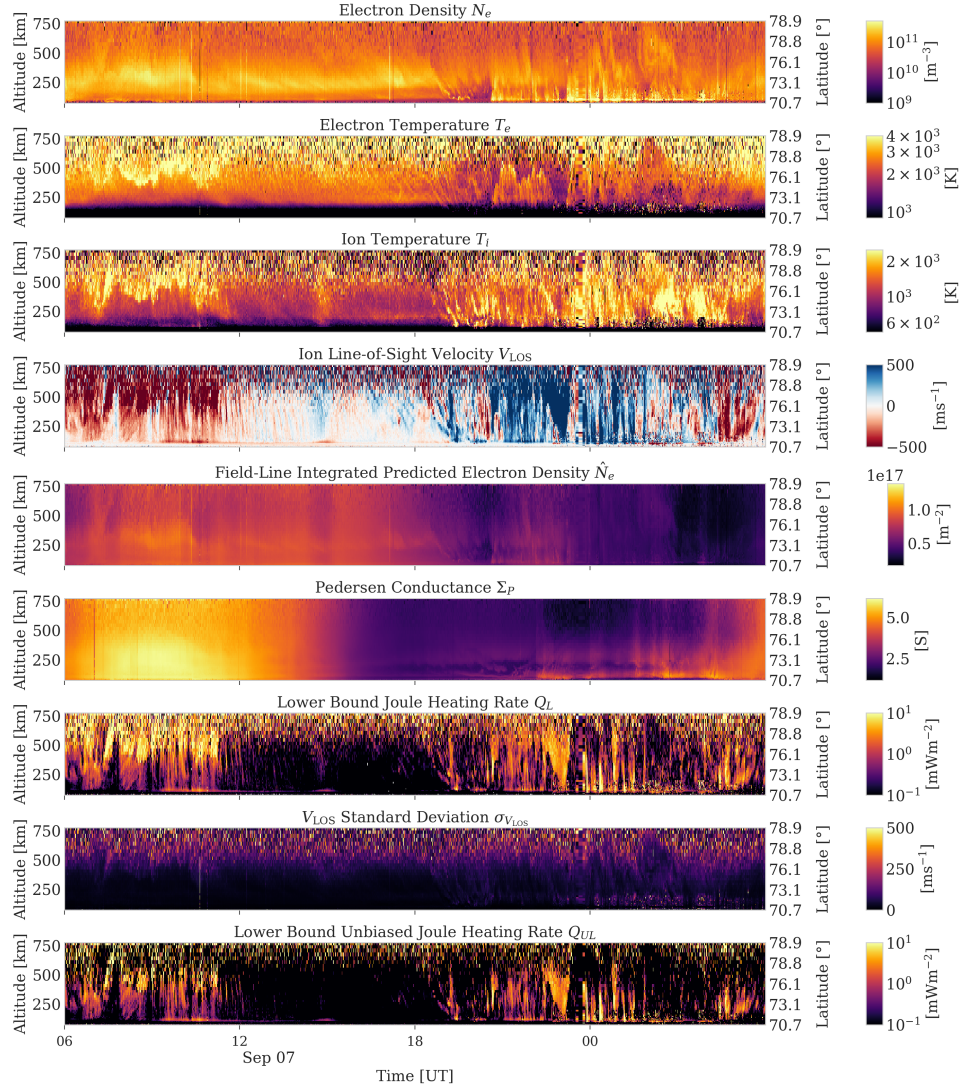


Figure 6.6: Overview of the stormy time case study (September 7–8, 2017). **Panel 1–4:** Measured Electron Density N_e and Temperature T_e , Ion Temperature T_i and LOS Velocity V_{LOS} from the EISCAT VHF radar. **Panel 5:** Field-Line Integrated Electron Density \hat{N}_e predicted by the FCNN. **Panel 6:** Derived Field-Line Integrated Pedersen Conductance Σ_P . **Panel 7:** Lower Bound Biased Joule Heating Rate Q_L . **Panel 8:** Standard Deviation of the ion LOS velocity measurement $\sigma_{V_{\text{LOS}}}$. **Panel 9:** Lower Bound Joule Heating Rate Q_{UL} calculated using $\beta = 30$. Note that for panels 5–9, the y-axis represents the altitude, and corresponding latitude, of the input measurement along the oblique VHF beam.

by elevated electron densities around 10^{11} m^{-3} , significantly higher than the quiet-time baseline.

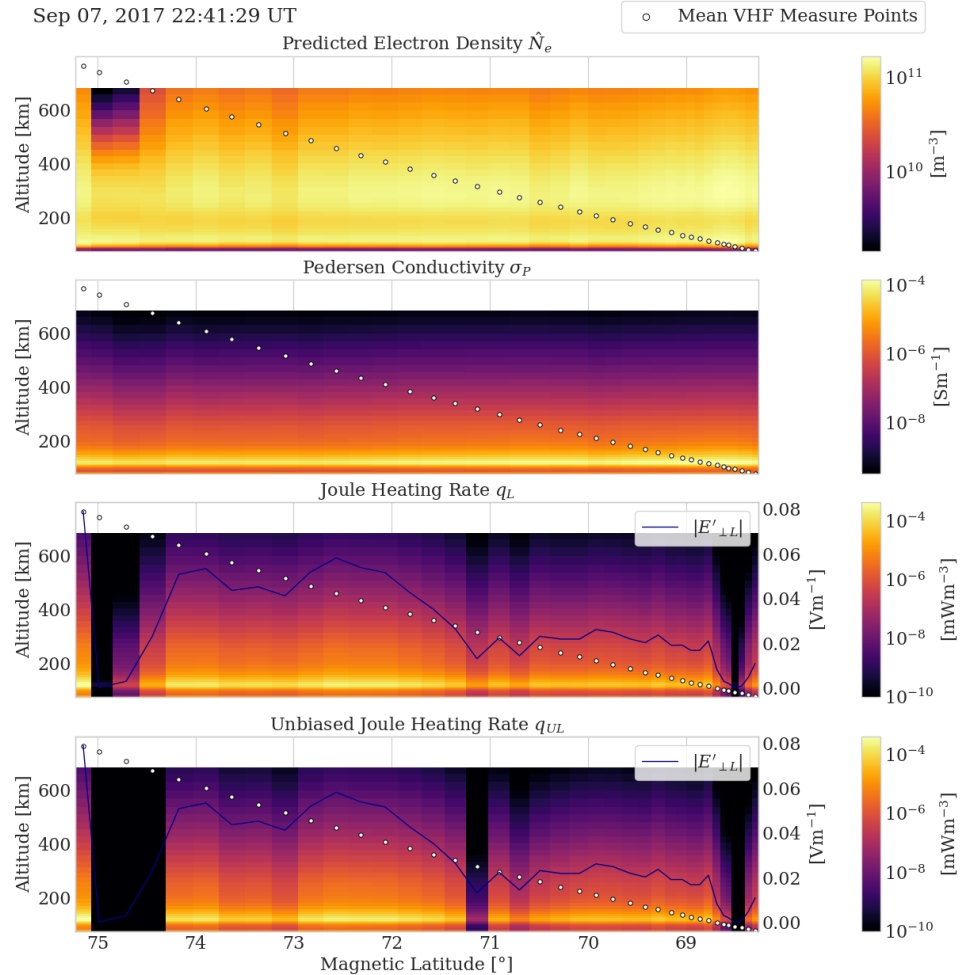


Figure 6.7: Cross-section of the ionosphere at 22:41:29 UT. The panels display from top to bottom: Predicted Electron Density Profiles \hat{N}_e , Pedersen Conductivity σ_P , Lower Bound Biased Joule Heating Rate q_L , and Lower Bound Unbiased Joule Heating Rate q_{UL} . The white scatter points indicate the altitude and Magnetic Latitude (MLAT) of the input VHF measurements used to generate each field-aligned profile. The blue line overlay on the bottom two plots represents the estimated perpendicular lower bound electric field magnitude $|E'_{\perp L}|$. Laundal et al. (2024)'s dipole Github package was used for the computation of MLATs.

The predicted electron density \hat{N}_e reveals a limitation in the generalizability of the model. That is, for input measurements taken above ~ 650 km altitude, predicted profiles exhibit a sharp discontinuity, as they appear unphysically

under-dense compared to its lower altitude neighbouring profiles. In the quiet time case, the extrapolation of these profiles remained fairly consistent, but it appears that high-latitude complex plasma dynamics challenges the model's ability to infer the profile accurately. However, we emphasize that the cross-sections presented in the case studies serves primarily as specific examples rather than the overall trends observed in the two 24-hour experiments.

Pedersen conductivity profiles σ_P remain morphologically consistent across MLATs. The profiles are characterized by the E-region peak at ~ 125 km altitude, and a decay for the upper ionosphere similar to that of the quiet case. Quantitatively, the magnitude of the conductivity reaches 10^{-4} Sm $^{-1}$, which is over an order of magnitude larger compared to the quiet time case. This observation remains consistent with the enhanced electron densities associated with the storm.

The most significant contrast with the quiet time case appears in the Joule heating rate panels q_L and q_{UL} . The electric field $|E'_{\perp L}|$ (overlaid blue line) display consistent values across MLATs, suggesting physical large-scale electric fields rather than random noise.

This interpretation is supported by the similarity between the biased and unbiased Joule heating rates q_L and q_{UL} , respectively. For the quiet case, the unbiasing method zeroed out large sections of the data due to low SNR. In contrast, here the unbiasing removes very few profiles, suggesting that the inferred electric field $|E'_{\perp L}|$ dominates over its error term $\sigma_{|E'_{\perp L}|}$. This suggests that the observed heating is the actual manifestation of the geomagnetic storm.

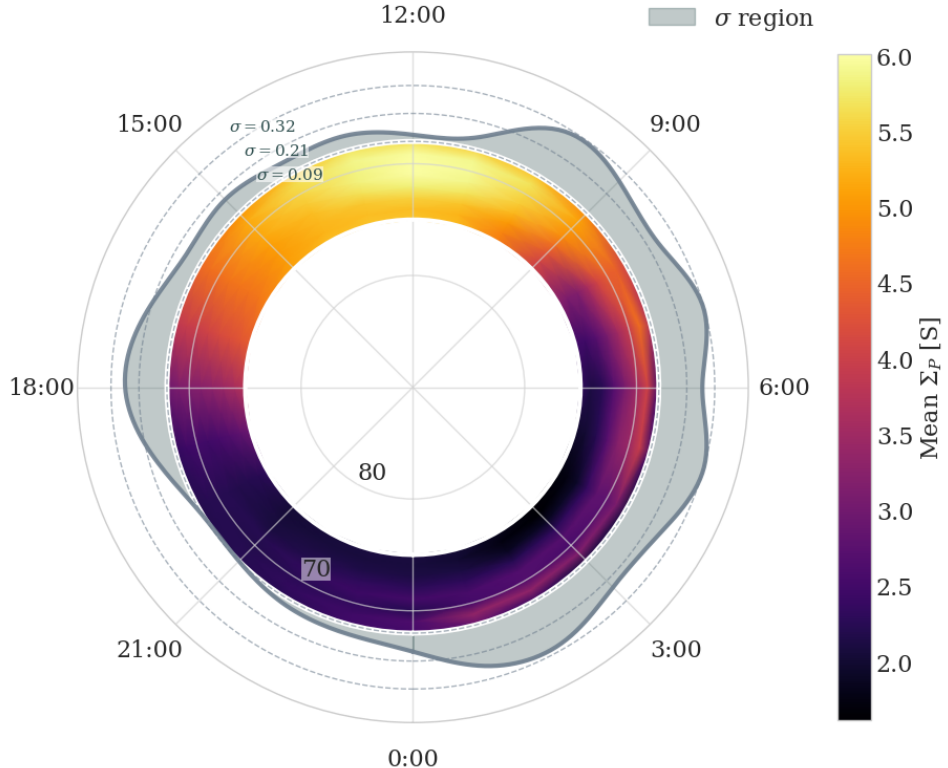


Figure 6.8: Polar projection of the mean Pedersen conductance Σ_P as a function of Magnetic Local Time (MLT) and Magnetic Latitude (MLAT). The color scale indicates the conductance. The greyshaded area bounded by the grey line indicates the temporal variation within each MLT bin. Numerical bounds are indicated on the top left.

Figure 6.8 presents the mean Pedersen conductance Σ_P in the CD coordinate system detailed in Subsection 6.1.1. The plot reveals that the greatest Pedersen conductance values is centered around ~ 12 MLT. Comparing these results with the ones obtained in Hardy et al. (1987), we again make the observation that their peak conductance values occur during midnight-early morning MLT sector. The magnitude of the conductances derived for geomagnetic active periods in Hardy et al. (1987) remains fairly consistent with the values we observe in our plot, ranging around ~ 6 S. Rosenqvist et al. (2006) calculated Pedersen conductance Σ_P observed during an intense geomagnetic storm commencing on October 30th, 2003, reaching magnitudes of ~ 120 S. These values remain significantly larger than the ones observed here, however, the October 2003 event remains one of the most geomagnetically active periods recorded in recent years (Rosenqvist et al., 2006).

Figure 6.9 presents the polar distribution of the biased Joule heating rate Q_L . We observe a pronounced gradient toward higher latitudes, but to a significantly smaller degree compared to the quiet case. While this is an indication that high-latitude noise still remains in the data, it is possible to resolve heating events to a greater extent. The main part of the heating occurs between 00:00 and 12:00 MLT, coinciding with the intervals observed in Figure 6.6. The variability of the heating is maximized around noon MLT, with peak standard deviation reaching ~ 65 .

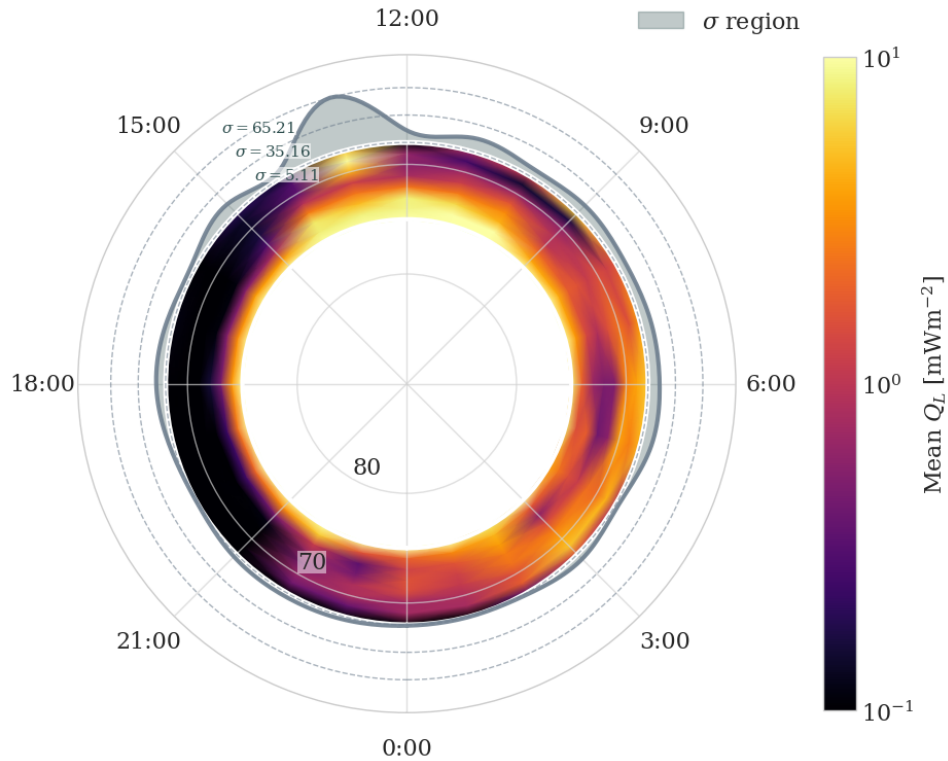


Figure 6.9: Polar projection of the mean lower bound Joule heating rate Q_L as a function of Magnetic Local Time (MLT) and Magnetic Latitude (MLAT). The color scale indicates the heating rate. The greyshaded area bounded by the grey line indicates the temporal variation within each MLT bin. Numerical bounds are indicated on the top left.

Finally, Figure 6.10 showcases the unbiased Joule heating rate Q_{UL} . Compared with the biased heating Q_L , we observe a significant reduction of the high-latitude gradient detailed in preceding sections. Additionally, background noise contributing to base level Joule heating is now reduced, which makes for identifying distinct events a simpler task. The variability of Q_{UL} is significantly lower compared to Q_L , suggesting that our unbiasing approach successfully

removes the contribution of high-frequency noise to Joule heating rates.

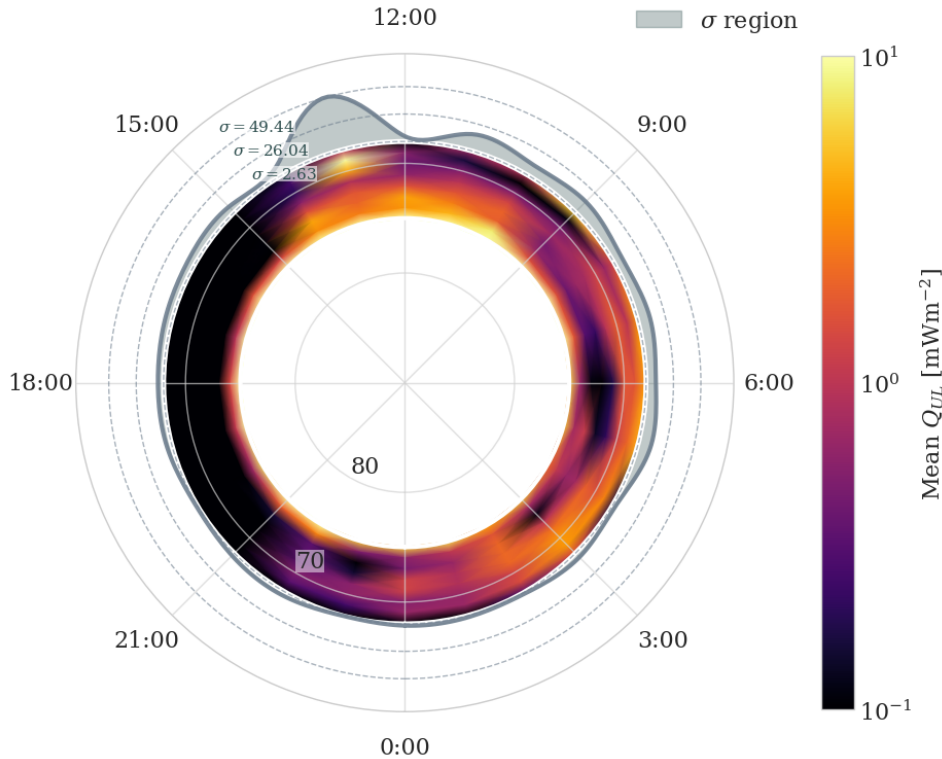


Figure 6.10: Polar projection of the mean unbiased lower bound Joule heating rate Q_{UL} as a function of Magnetic Local Time (MLT) and Magnetic Latitude (MLAT). The color scale indicates the heating rate. The greyshaded area bounded by the grey line indicates the temporal variation within each MLT bin. Numerical bounds are indicated on the top left.

6.2 Methodology Evaluation

To achieve a highly optimized model for this task, a more extensive training and evaluation scheme is required. Due to the stochastic nature of neural network initialization and optimization, an ensemble of the final model configuration should be individually trained. This approach allows the assessment of the stability of the model, ensuring that the presented performance is robust and not the result of a fortunate initialization outlier.

The current FCNN architecture does not account for the spatial and temporal dependencies in the data, as it treats each individual profile as an independent event. Ionospheric plasma parameters are correlated in space and time on

smaller scales (Brekke, 2012; Kelley, M.C., 1989), and therefore, by incorporating such a dependency, the model may be able to predict/reconstruct electron density profiles with a higher precision.

The consistently lower conductances produced by the FCNN in comparison with those from raw and AS profiles, suggests that the FCNN consistently underestimates electron density profiles. The variant of MSE employed in this thesis effectively handles noisy data, but the quadratic penalty leads to an unproportional punishment of large outliers. This causes the model to be more cautious in terms of predicting large-magnitude values, biasing the predicted electron densities towards lower magnitudes. To mitigate this, we can employ loss functions proving more robust to such outliers, such as Huber loss (Huber, 1992). This loss function employs linear and quadratic penalization for large and smaller magnitude errors, respectively. This could potentially allow the network to capture high-density events without compromising its overall performance.

Regarding the derived products, local fluctuations and irregularities in V_{LOS} propagates directly into the calculations of the Joule heating rates. Ideally, our methodology would employ entire profiles of the ion velocity perpendicular to the geomagnetic field. However, we are constrained to the V_{LOS} as measured by the VHF radar beam, which require the assumption that the electric field derived from this one measurement maps to the entire field aligned column. This assumption is an untenable one; the change in regional ionospheric properties in the field aligned column opens up for significant uncertainties (Brekke, 2012; Kelley, M.C., 1989).

Finally, the Joule heating rates calculated in the case studies must be interpreted as lower bounds of the true heating rates. These estimates rely on the electric field derived from the ion LOS velocity V_{LOS} measured by the ISR. In the idealized scenario where the entire local ion flow is captured by the ISR, this estimation is accurate. However, the total ion flow is rarely one-dimensional (Brekke, 2012; Kelley, M.C., 1989), thus, neglecting the ion velocity orthogonal to the radar beam will inevitably underestimate the derived magnitude of $|E'_\perp|$. One approach to mitigate this discrepancy is to incorporate ground-based magnetometer data. The relative change in magnetic field components, can yield information about the currents flowing in the ionosphere. However, due to the nature of such measurements, it can only capture large-scale low-frequency phenomena (Brekke, 2012). While this hybrid approach would raise the lower bound, the high-frequency components, which are often related to Joule heating events (Palmroth et al., 2021), remain uncaptured.

6.3 Future Work

The model presented in this thesis serves primarily as a proof-of-concept. It is intended to demonstrate the feasibility and potential of machine learning applications in space physics, rather than representing a fully optimized production system. Exploring other model architectures or machine learning frameworks may prove beneficial, as an exhaustive comparative analysis of network architectures was beyond the scope of this project. Beyond architectural optimization, we identify several key extensions to this work.

6.3.1 Model Explainability

The inherent ability of neural networks to map complex non-linear relations raises critical questions regarding their transparency. In particular, how predictions are derived and which input features drive the outcome. Without the proper analysis, neural networks effectively functions as "black boxes" as the mapping from input to output remains unknown.

Implementing feature importance analysis would quantify the influence of individual input features on the model's predictions. Methodologies like SHAP (SHapley Additive exPlanations) (Lundberg and Lee, 2017) or gradient analysis using saliency maps can improve model interpretability, and guide feature selection. In turn, this may increase computational efficiency due to dimensionality reduction of the dataset. Additionally, in the context of physics, such an analysis can yield crucial information on how local plasma- or global geophysical conditions affect the altitudinal distribution of electrons in the ionosphere.

A rigorous analysis of the training data distribution is essential for a robust model. If unbalanced datasets are used to train neural networks, the resulting model will be biased towards majority dataset conditions. A qualitative analysis of the training dataset can reveal uneven distribution of geomagnetic conditions. Mitigating this by constructing a balanced dataset could improve the generalizability of the model.

6.3.2 Extension of framework

As the predicted electron density profiles proves sufficiently accurate, a logical extension of the framework is the inference of electron and ion temperature profiles. This can both be done through utilizing entire predicted electron density profiles or single-altitude inputs. However, with such sequential approach comes a caveat of uncertainty propagation. However, if we can circumvent this aspect, such an approach could improve on current state-of-the-art global

models, e.g., IRI, by utilizing spatial information from the specific localized area.

6.3.3 Extension using ESR

The EISCAT system includes the EISCAT Svalbard Radar (ESR) facility (Tjulin, 2025). This site is located approximately along the trajectory of north-pointing VHF radar beam. A similar model to the one presented in this thesis could be developed using ESR data. By interpolating between the EISCAT Ramfjordmoen model and the ESR model, it could be possible to infer ionospheric conditions across twice the latitudinal range of the current study.



7

Conclusion

This thesis is motivated by the observational limitations currently hindering estimation of high-latitude ionospheric Joule heating. This energy dissipation mechanism significantly impacts the neutral atmosphere and, in extreme scenarios, can lead to the loss of operational satellites due to increased orbital drag (Fang et al., 2022). By leveraging the analytical capabilities of DNNs and the high temporal resolution of ISR data, we introduce a novel framework for estimating Joule heating rates.

The results confirm our posed hypothesis: that magnetic field lines act as equipotentials, creating strong correlations between plasma parameters along the field line. As a consequence, we find that a neural network utilizing localized, altitude-specific input parameters and global geophysical indices, is capable of accurately predicting field aligned electron density profiles.

Specifically, this work has successfully addressed the six primary objectives defined in the introduction:

1. We described the physical basis for the model, emphasizing that the high conductivity parallel to magnetic field lines allows for the mapping of plasma parameters. We established that reconstructing these profiles is essential for quantifying the Joule heating that poses a risk to space infrastructure.
2. We demonstrated that the complex, non-linear relationship between local

plasma parameters, geophysical indices, and the full field aligned electron density profile can be modeled by a fully connected neural network.

3. The model's conductance estimates were validated against ground truth EISCAT UHF measurements. Comparisons with the statistical model provided by Hardy et al. (1987) reveal that the neural network captures dynamic variations in conductance that such statistical models fail to resolve.
4. We successfully converted the predicted electron densities into field-line resolved Pedersen conductivity profiles using EISCAT VHF data. This step confirmed that valid conductivity estimates can be derived solely from single-altitude inputs when combined with atmospheric models.
5. We applied the derived conductances to the EISCAT VHF geometry to calculate Joule heating rates. Unlike previous models which rely on statistical measures, this method utilized localized plasma parameters to capture high-resolution heating events, providing a lower bound estimate for energy dissipation in the high-latitude ionosphere.
6. Finally, we provide a critical evaluation of the methodology. We identified specific limitations, such as the constraints of the loss function and the fact that the model only captures electric fields in one dimension. We also highlight the potential extension of this framework, by e.g., applying the same methodology to the EISCAT Svalbard Radar.

The success of this approach implies that the mapping from local plasma conditions to the field line profile is to a certain degree physically deterministic. The model serves as a proof-of-concept, as it successfully demonstrates the feasibility and potential of machine learning applications in space physics. Until next generation radar systems, such as EISCAT_3D, comes online, such data-driven techniques provide the spatial and temporal resolution required to make qualified estimates of Joule heating rates in the high-latitude atmosphere.

Technical Acknowledgments

I have used LLMs, such as ChatUiT, for language revision and proofreading purposes, while ensuring accordance with my supervisors and the UiT guidelines. All content, ideas and arguments presented in this thesis originates from either my supervisors or myself.

The EISCAT UHF and VHF data sets were provided from MadrigalWeb(Rideout and Cariglia, N.D.). The API provided an efficient way of downloading around 20 years of data for each radar using the `globalIsprint.py` script.

"EISCAT is an international association supported by research organisations in China (CRIRP), Finland (SA), Japan (NIPR and ISEE), Norway (NFR), Sweden (VR), and the United Kingdom (UKRI)" (EISCAT AB, 2024).

The data set containing the global geophysical parameters was retrieved from OMNIWeb. Parameters AE, AL, SYM/H and PCN were retrieved from the high resolution 5 minute data, while the Ap and F10.7 index were retrieved from 1h resolution data (NASA, N.D.).

The code used for this thesis will shortly after delivery be available on my [GitHub](#).

Bibliography

- H. Alfvén. On the theory of magnetic storms and aurorae. *Tellus*, 10(1):104–116, 1958.
- E. V. Appleton and M. A. Barnett. On some direct evidence for downward atmospheric reflection of electric rays. *Proceedings of the Royal Society of London. Series A, Containing Papers of a Mathematical and Physical Character*, 109(752):621–641, 1925.
- H. F. Bates. Atmospheric expansion from joule heating. *Planetary and Space Science*, 22(6):925–937, 1974.
- W. Beynon and P. J. Williams. Incoherent scatter of radio waves from the ionosphere. *Reports on Progress in Physics*, 41(6):909, 1978.
- K. L. Bowles. Incoherent scattering by free electrons as a technique for studying the ionosphere and exosphere: Some observations and theoretical considerations. *J. Res. NBS D*, 65:1, 1961.
- A. Brekke. *Physics of the upper polar atmosphere*. Springer Science & Business Media, 2012.
- F. F. Chen et al. *Introduction to plasma physics and controlled fusion*, volume 1. Springer, 1984.
- W. K. Chen. *The electrical engineering handbook*. Elsevier, 2004.
- S. Cowley. Magnetosphere-ionosphere interactions: A tutorial review. *Magnetospheric Current Systems, Geophys. Monogr. Ser*, 118:91–106, 2000.
- P. Cunningham, M. Cord, and S. J. Delany. Supervised learning. In *Machine learning techniques for multimedia: case studies on organization and retrieval*, pages 21–49. Springer, 2008.
- T. N. Davis and M. Sugiura. Auroral electrojet activity index ae and its universal

- time variations. *Journal of Geophysical Research*, 71(3):785–801, 1966.
- J. P. Dougherty and D. T. Farley. A theory of incoherent scattering of radio waves by a plasma. *Proceedings of the Royal Society of London. Series A. Mathematical and Physical Sciences*, 259(1296):79–99, 1961.
- J. W. Dungey. Interplanetary magnetic field and the auroral zones. *Physical Review Letters*, 6(2):47, 1961.
- EISCAT AB. EISCAT Tromsø Site. <https://eiscat.se/about/sites/eiscat-tromso-site/>, 2021. Accessed 13-10-2025.
- EISCAT AB. EISCAT Data. <https://eiscat.se/scientist/data/>, 2024. Accessed 13-10-2025.
- European Space Agency. ESA Space Environment Report 2025. Report, European Space Agency, 2025. URL https://www.esa.int/Space_Safety/Space_Debris/ESA_Space_Environment_Report_2025.
- T.-W. Fang, A. Kubaryk, D. Goldstein, Z. Li, T. Fuller-Rowell, G. Millward, H. J. Singer, R. Steenburgh, S. Westerman, and E. Babcock. Space weather environment during the spacex starlink satellite loss in february 2022. *Space weather*, 20(11):e2022SW003193, 2022.
- J. Fejer. Scattering of radio waves by an ionized gas in thermal equilibrium. *Canadian Journal of Physics*, 38(8):1114–1133, 1960.
- A. L. Fradkov. Early history of machine learning. *IFAC-PapersOnLine*, 53(2):1385–1390, 2020.
- A. Fraknoi, D. Morrison, and S. C. Wolff. *Astronomy 2e*. OpenStax, 2022.
- T. Fuller-Rowell, M. Codrescu, R. Moffett, and S. Quegan. Response of the thermosphere and ionosphere to geomagnetic storms. *Journal of Geophysical Research: Space Physics*, 99(A3):3893–3914, 1994.
- I. Goodfellow. Deep learning. i. goodfellow, y. bengio, a. courville, 2016.
- W. E. Gordon. Incoherent scattering of radio waves by free electrons with applications to space exploration by radar. *Proceedings of the IRE*, 46(11):1824–1829, 2007.
- T. Hagfors. Density fluctuations in a plasma in a magnetic field, with applications to the ionosphere. *Journal of Geophysical Research*, 66(6):1699–1712,

1961.

- D. A. Hardy, M. Gussenhoven, R. Raistrick, and W. McNeil. Statistical and functional representations of the pattern of auroral energy flux, number flux, and conductivity. *Journal of Geophysical Research: Space Physics*, 92(A11):12275–12294, 1987.
- K. Hornik, M. Stinchcombe, and H. White. Multilayer feedforward networks are universal approximators. *Neural networks*, 2(5):359–366, 1989.
- R. Howe. Solar interior rotation and its variation. *Living Reviews in Solar Physics*, 6(1):1–75, 2009.
- P. J. Huber. Robust estimation of a location parameter. In *Breakthroughs in statistics: Methodology and distribution*, pages 492–518. Springer, 1992.
- R. Ilma. iri2016, 2024. URL <https://github.com/space-physics/iri2016>.
- S. Ioffe and C. Szegedy. Batch normalization: Accelerating deep network training by reducing internal covariate shift. In *International conference on machine learning*, pages 448–456. pmlr, 2015.
- M. I. Jordan and T. M. Mitchell. Machine learning: Trends, perspectives, and prospects. *Science*, 349(6245):255–260, 2015.
- Kelley, M.C. *The Earth's Ionosphere*. Academic Press Incorporated, 1989.
- A. Kero. Ionospheric d-region studies by means of active heating experiments and modelling. 2008.
- D. B. J. Kingma et al. A method for stochastic optimization. *arXiv preprint arXiv:1412.6980*, 1412(6), 2014.
- M. G. Kivelson and F. Bagenal. Chapter 28 - planetary magnetospheres. In L.-A. McFadden, P. Weissman, and T. Johnson, editors, *Encyclopedia of the Solar System (Second Edition)*, pages 519–540. Academic Press, San Diego, second edition edition, 2007. ISBN 978-0-12-088589-3. doi: <https://doi.org/10.1016/B978-012088589-3/50032-3>. URL <https://www.sciencedirect.com/science/article/pii/B9780120885893500323>.
- H. E. Koskinen and E. I. Tanskanen. Magnetospheric energy budget and the epsilon parameter. *Journal of Geophysical Research: Space Physics*, 107(A11):SMP-42, 2002.

- A. Krogh and J. Hertz. A simple weight decay can improve generalization. *Advances in neural information processing systems*, 4, 1991.
- E. Kudeki and M. A. Milla. Incoherent scatter spectral theories—part i: A general framework and results for small magnetic aspect angles. *IEEE Transactions on Geoscience and Remote Sensing*, 49(1):315–328, 2010.
- K. Laundal. ppigrf, 2025. URL <https://github.com/IAGA-VMOD/ppigrf>.
- K. Laundal, J. Reistad, A. Smith, and A. Hovland. dipole. <https://github.com/klaundal/dipole>, 2024.
- J. Lean, R. Meier, J. Picone, F. Sassi, J. Emmert, and P. Richards. Ionospheric total electron content: Spatial patterns of variability. *Journal of Geophysical Research: Space Physics*, 121(10):10–367, 2016.
- Y. LeCun, Y. Bengio, and G. Hinton. Deep learning. *Nature*, 521:436–444, 2015. doi: 10.1038/nature14539.
- R. Leitinger. Ionospheric electron content: the european perspective. *Annals of Geophysics*, 41(5-6), 1998.
- H. Li, Z. Xu, G. Taylor, C. Studer, and T. Goldstein. Visualizing the loss landscape of neural nets. *Advances in neural information processing systems*, 31, 2018.
- Lissauer, J. and de Pater, I. *Fundamental Planetary Science: Physics, Chemistry, and Habitability*. Cambridge University Press, 2019.
- I. Loshchilov, F. Hutter, et al. Fixing weight decay regularization in adam. *arXiv preprint arXiv:1711.05101*, 5(5):5, 2017.
- S. M. Lundberg and S.-I. Lee. A unified approach to interpreting model predictions. *Advances in neural information processing systems*, 30, 2017.
- L. Ma, X. Tian, Y. Yu, L. Tang, and J. Cao. Statistical relations between ionospheric conductance and precipitating electrons derived from direct conjugate observations. *Space Weather*, 23(6):e2025SW004345, 2025.
- NASA. OMNIWeb Plus. <https://omniweb.gsfc.nasa.gov/>, N.D. Accessed 30-09-2025.
- M. Palmroth, M. Grandin, T. Sarris, E. Doornbos, S. Tourgaidis, A. Aikio, S. Buchert, M. A. Clilverd, I. Dandouras, R. Heelis, et al. Lower-thermosphere–ionosphere (lti) quantities: current status of measuring techniques and mod-

- els. In *Annales Geophysicae*, volume 39, pages 189–237. Copernicus GmbH, 2021.
- H. L. Pécseli. *Introduction to the Theory of Incoherent Scattering of Radar Waves from Plasmas*. Springer Nature, 2025.
- J. Picone, A. Hedin, D. P. Drob, and A. Aikin. Nrlmsise-oo empirical model of the atmosphere: Statistical comparisons and scientific issues. *Journal of Geophysical Research: Space Physics*, 107(A12):SIA–15, 2002.
- T. Rexer. Radio wave propagation through the ionosphere. 2021.
- W. Rideout and K. Cariglia. Madrigal Database at CEDAR. <https://cedar.openmadrigal.org/>, N.D. Accessed: 30-09-2025.
- L. Rosenqvist, S. Buchert, H. Opgenoorth, A. Vaivads, and G. Lu. Magnetospheric energy budget during huge geomagnetic activity using cluster and ground-based data. *Journal of Geophysical Research: Space Physics*, 111(A10), 2006.
- G. Rostoker. Geomagnetic indices. *Reviews of Geophysics*, 10(4):935–950, 1972.
- C. Russell, J. Luhmann, and R. Strangeway. *Space Physics: An Introduction*. Cambridge Univeristy Press, 2016.
- C. T. Russell. Geophysical coordinate transformations. *Cosmic electrodynamics*, 2(2):184–196, 1971.
- E. E. Salpeter. Scattering of radio waves by electrons above the ionosphere. *Journal of Geophysical Research*, 65(6):1851–1852, 1960.
- K. Sartipzadeh, A. Kvammen, B. Gustavsson, N. Gulbrandsen, M. G. Johnsen, D. Huyghebaert, and J. Vierinen. Plasma density estimation from ionograms and geophysical parameters with deep learning. *EGUsphere*, 2025:1–32, 2025.
- R. Schunk and A. Nagy. *Collisions*, page 72–112. Cambridge Atmospheric and Space Science Series. Cambridge University Press, 2009a.
- R. Schunk and A. Nagy. *Simplified transport equations*, page 113–158. Cambridge Atmospheric and Space Science Series. Cambridge University Press, 2009b.
- S. Sharma, S. Sharma, and A. Athaiya. Activation functions in neural networks. *Towards Data Sci*, 6(12):310–316, 2017.
- N. Srivastava, G. Hinton, A. Krizhevsky, I. Sutskever, and R. Salakhutdinov.

- Dropout: a simple way to prevent neural networks from overfitting. *The journal of machine learning research*, 15(1):1929–1958, 2014.
- S. M. Stankov, N. Jakowski, S. Heise, P. Muhtarov, I. Kutiev, and R. Warnant. A new method for reconstruction of the vertical electron density distribution in the upper ionosphere and plasmasphere. *Journal of Geophysical Research: Space Physics*, 108(A5), 2003.
- P. Stauning. The polar cap index: A critical review of methods and a new approach. *Journal of Geophysical Research: Space Physics*, 118(8):5021–5038, 2013.
- K. Tapping. The 10.7 cm solar radio flux (f10.7). *Space weather*, 11(7):394–406, 2013.
- P. Tenfjord and N. Østgaard. Energy transfer and flow in the solar wind-magnetosphere-ionosphere system: A new coupling function. *Journal of Geophysical Research: Space Physics*, 118(9):5659–5672, 2013.
- J. Thayer and J. Vickrey. On the contribution of the thermospheric neutral wind to high-latitude energetics. *Geophysical research letters*, 19(3):265–268, 1992.
- J. P. Thayer and J. Semeter. The convergence of magnetospheric energy flux in the polar atmosphere. *Journal of Atmospheric and Solar-Terrestrial Physics*, 66(10):807–824, 2004.
- J. J. Thomson. Carriers of negative electricity. *Nobel Lecture, December*, 11(1906): 1901–1921, 1906.
- A. Tjulin. Eiscat experiments. *EISCAT Scientific Association*, 350, 2025.
- C. M. van Hazendonk, L. Baddeley, K. M. Laundal, and J. Chau. Detection and energy dissipation of ulf waves in the polar ionosphere: A case study using the eiscat radar. *Journal of Geophysical Research: Space Physics*, 129(7): e2024JA032633, 2024.
- V. M. Vasyliūnas and P. Song. Meaning of ionospheric joule heating. *Journal of Geophysical Research: Space Physics*, 110(A2), 2005.
- J. Vierinen. isr_spec, 2025. URL https://github.com/jvierine/isr_spec.
- J. A. Wanliss and K. M. Showalter. High-resolution global storm index: Dst versus sym-h. *Journal of Geophysical Research: Space Physics*, 111(A2), 2006.

E. J. Weber and L. Davis Jr. The angular momentum of the solar wind. *Astrophysical Journal, vol. 148, p. 217-227*, 148:217–227, 1967.

S. E. Whang, Y. Roh, H. Song, and J.-G. Lee. Data collection and quality challenges in deep learning: A data-centric ai perspective. *The VLDB Journal, 32(4):791–813*, 2023.

M. Yamauchi, T. Sergienko, C.-F. Enell, A. Schillings, R. Slapak, M. G. Johnsen, A. Tjulin, and H. Nilsson. Ionospheric response observed by eiscat during the 6–8 september 2017 space weather event: Overview. *Space Weather, 16 (9):1437–1450*, 2018.

Z.-H. Zhou. *Machine learning*. Springer nature, 2021.

X. Zhu, E. Talaat, J. Baker, and J.-H. Yee. A self-consistent derivation of ion drag and joule heating for atmospheric dynamics in the thermosphere. *23 (10):3313–3322*, 2005.



Exploratory Data Analysis

A.o.1 UHF Analysis

This section presents a comprehensive analysis of the UHF dataset, which serves as the primary training data for the neural network. We examine the spatial and temporal extent of the dataset, the prevalence of missing values, parameter distributions, and the alignment of radar look-directions with the local geomagnetic field.

Temporal and Spatial Data Availability

The UHF dataset is an aggregation of multiple experiments conducted with variable temporal spacing. While the intra-experiment temporal resolution is typically 1 minute, the spatial (vertical) resolution varies depending on the specific radar program. In this thesis, we define a *measurement* as the collection of data for a single timestamp and elevation angle. Each measurement consists of *profiles* of ISR parameters (e.g., electron density) sampled at specific altitudes. All profiles within a single measurement share the same length. Figure A.1 illustrates the timeline of available ISR data, showing measurement profile lengths over time. The dataset effectively begins in October 2007, spanning approximately 16 years.

Figure A.2 presents the distribution of profile lengths for all unique measurements. The y-axis is logarithmic to enhance readability. It is evident that profiles

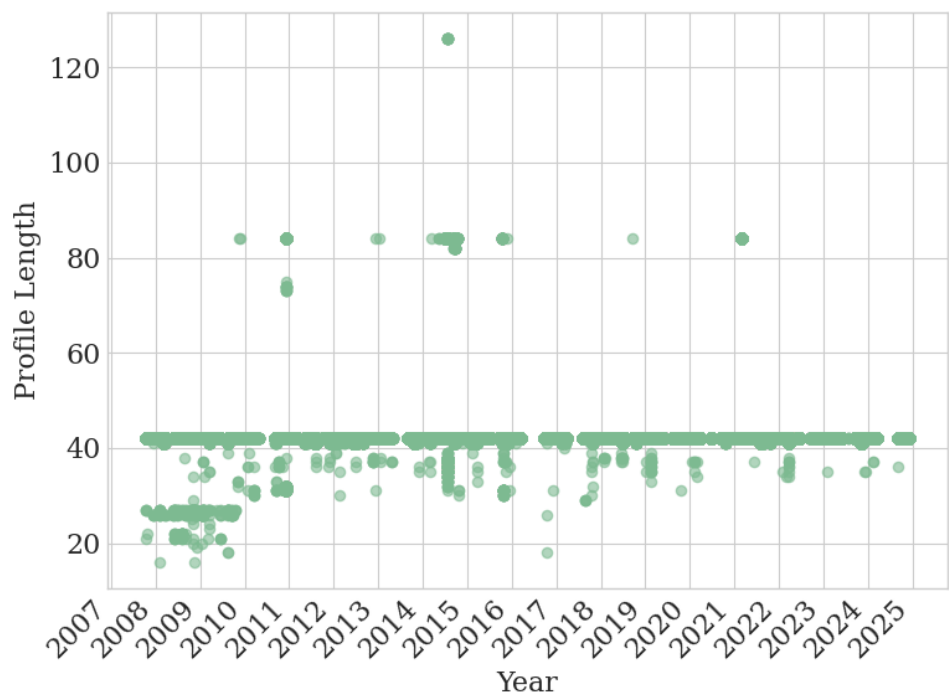


Figure A.1: Scatterplot visualizing the timeline of available ISR data and the number of range gates (profile length) per measurement.

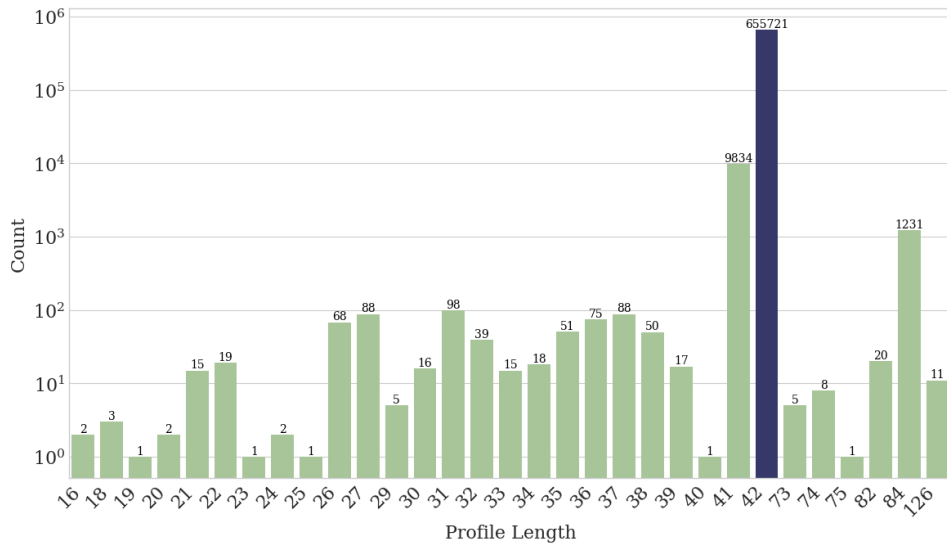


Figure A.2: Distribution of altitude counts (profile lengths) per timestamp. The x-axis represents the number of range gates in a single measurement, while the y-axis shows the frequency of such occurrences.

of length 42 are the most abundant, accounting for 655,721 measurements.

Notably, the distribution includes multiples of 42, such as 84 or 126. Investigation reveals these are instances where two or three profiles of length 42 are concatenated in sequence. To ensure input consistency for the neural network, we restrict our analysis to the 655,721 measurements with a standard profile length of 42 range gates. This subset forms the basis of the analysis unless specified otherwise.

The vertical spatial resolution is altitude-dependent, as shown in Figure A.3. The scatter points indicate the mean altitude for each range gate index, while the color map represents the standard deviation (σ). The altitude profiles exhibit high stability, with $\sigma \approx 0.5$ km for most gates, except for the highest range gate where $\sigma \approx 3$ km.

Figure A.4 displays the number of measurements per day. Given a 1-minute resolution, a continuous 24-hour run yields 1440 measurements. However, certain days exceed this count. Closer examination reveals that the radar occasionally interleaves measurements at slightly different elevations within the same minute (e.g., measuring at 77° elevation at 12:00:00, then 78° at 12:00:15). This interleaving is a characteristic of the CP2 scan pattern utilized in these experiments (Tjulin, 2025).

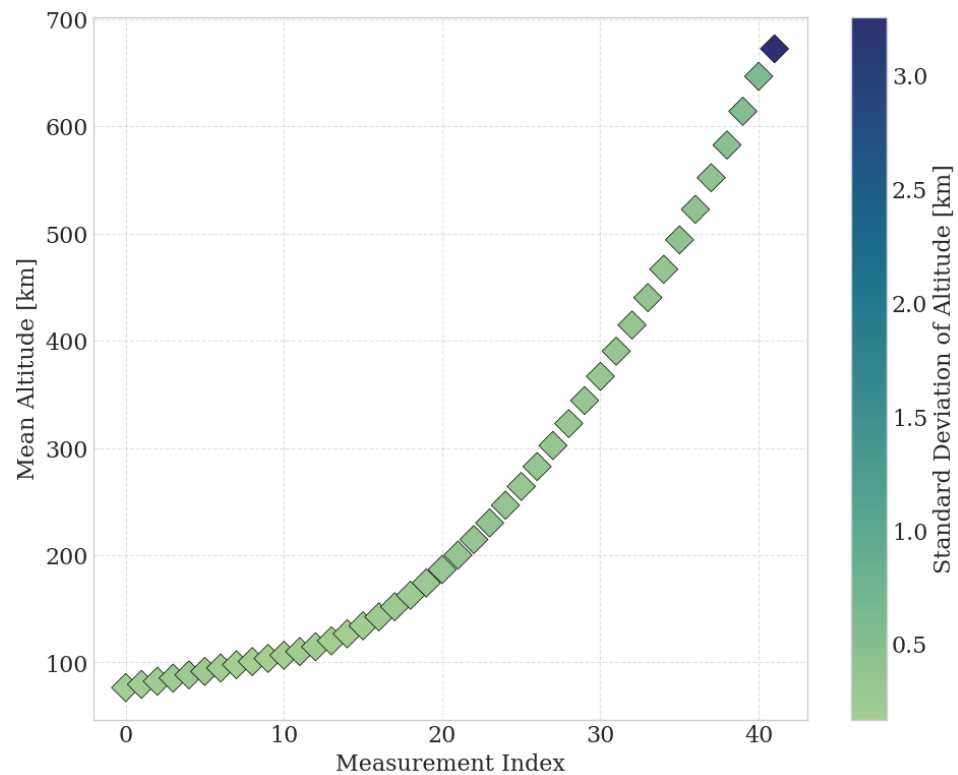


Figure A.3: Scatterplot showing the mean and standard deviation of altitude for each of the 42 range gates in the standard ISR profile.

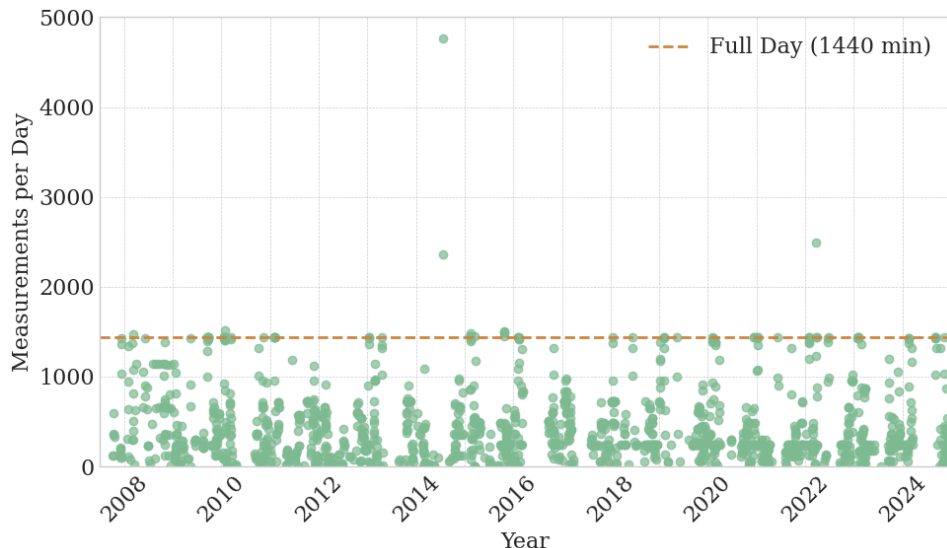


Figure A.4: Timeline of ISR data availability showing the number of individual profiles per day. The orange line indicates 1440 samples, the theoretical maximum for 1-minute resolution data in a 24-hour period. Note the absence of data from the *beata* program prior to 2007.

The seasonal and diurnal distribution of the data inherently influences the model's generalization capabilities. Figure A.5 illustrates the data distribution as a function of Day of Year (DOY) for the period 2007-2024. The data is predominantly collected during the winter months (September-April), suggesting the model will be biased towards winter ionospheric conditions. Similarly, Figure A.6 reveals the diurnal collection pattern, showing a concentration of measurements during daytime (10-15 UT) and evening (18-24 UT) hours.

ISR Parameters

Azimuth and Zenith Angles

The UHF radar utilizes variable azimuth and zenith angles throughout the experiments, as shown in Figure A.7 and Figure A.8, respectively. The majority of observations cluster around an azimuth of 185° and an elevation of 77° , corresponding to the approximate geomagnetic field line direction at Tromsø.

Crucially, the geomagnetic field is not static; its magnitude and direction drift over time due to secular variation. Using the International Geomagnetic Reference Field (IGRF) model, we quantify this migration for the coordinate

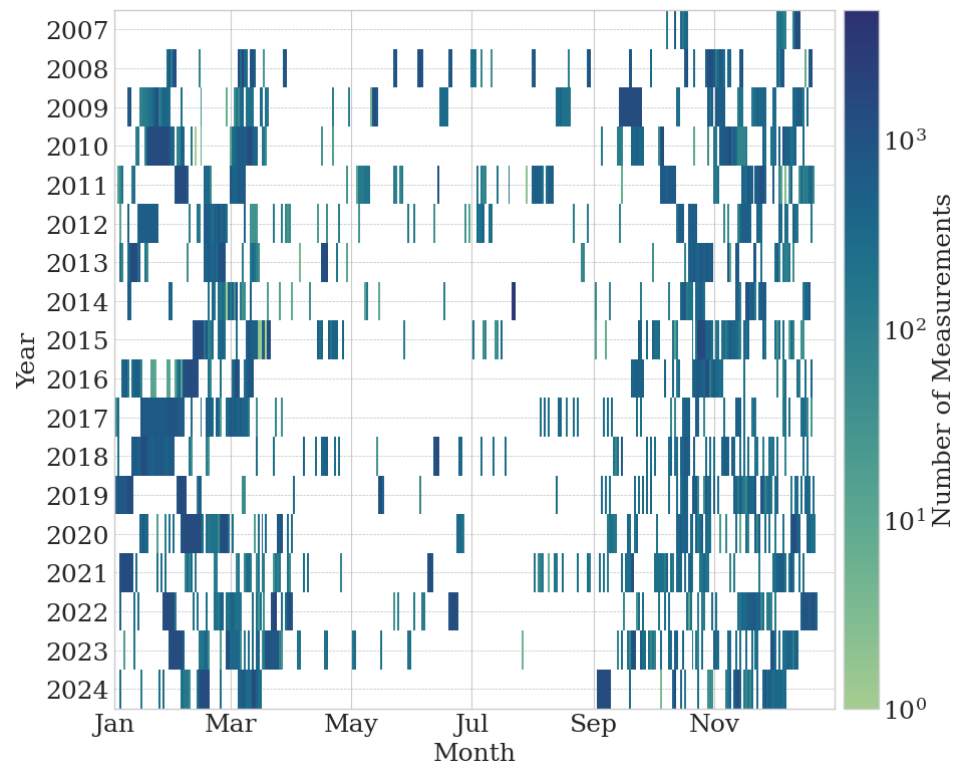


Figure A.5: Heatmap visualizing data availability per Day of Year (DOY) over the period 2007-2024.

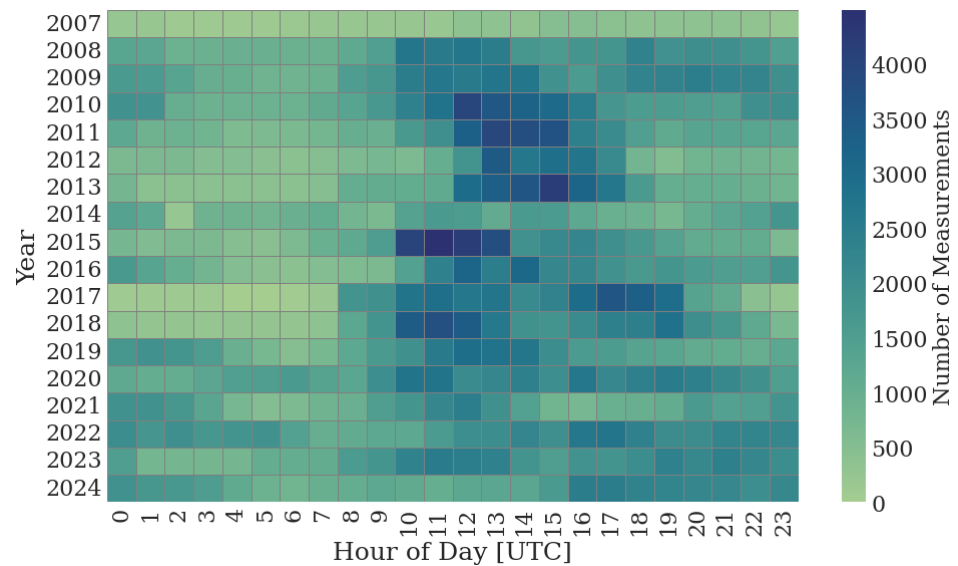


Figure A.6: Heatmap visualizing data availability per Time of Day (TOD) over the period 2007-2024.

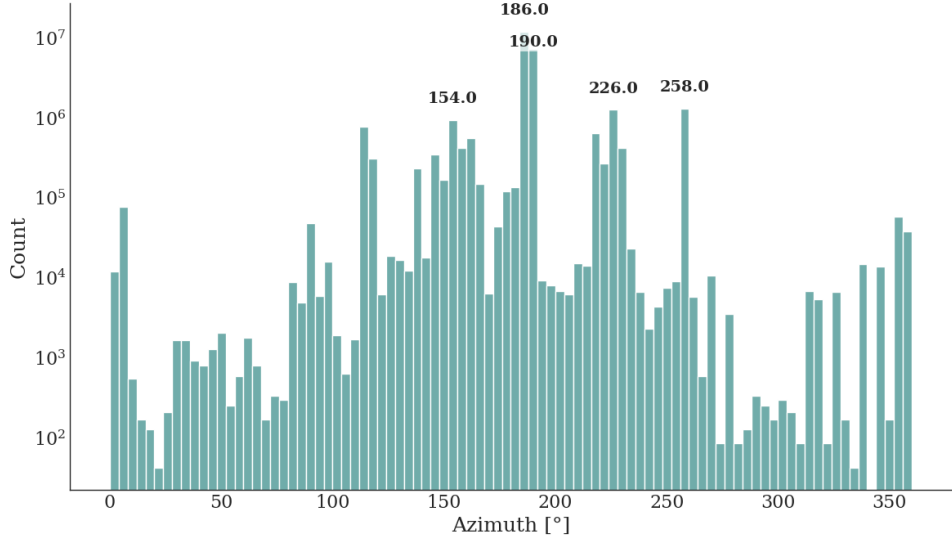


Figure A.7: Distribution of radar azimuth angles. Values are binned into 50 intervals, with the top 5 bins annotated.

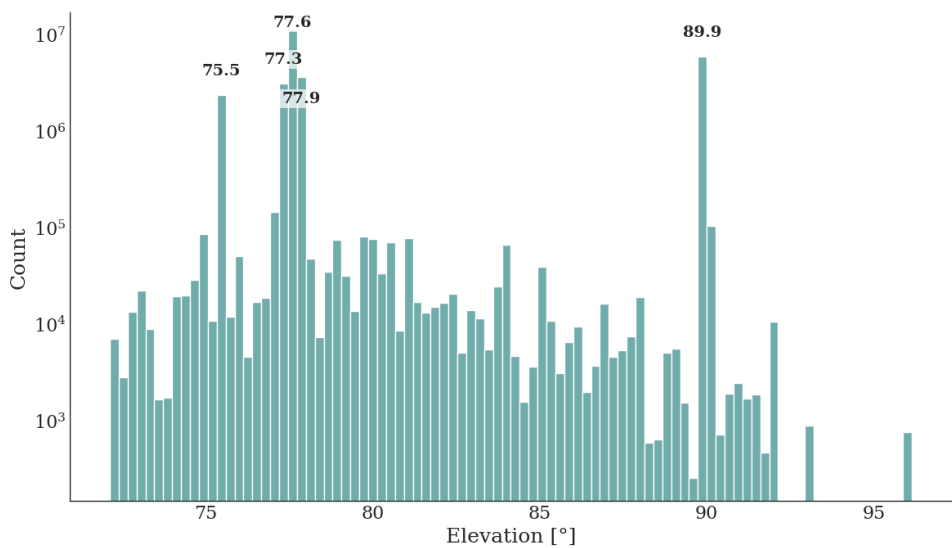


Figure A.8: Distribution of radar elevation angles. Values are binned into 50 intervals, with the top 5 bins annotated.

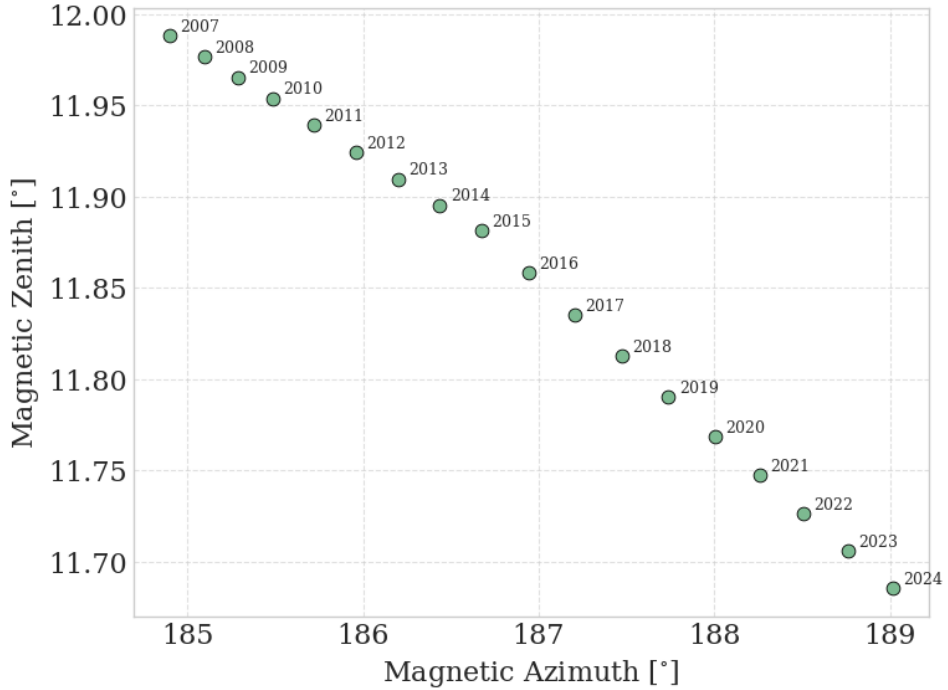


Figure A.9: Scatterplot showing the secular variation of magnetic azimuth and zenith angles for EISCAT Ramfjordmoen at 300 km altitude, 2007-2024.

[69.586°, 19.226°] at 300 km altitude. Figure A.9 shows that while the magnetic zenith has remained relatively stable (shifting < 0.3°), the magnetic azimuth has migrated by over 4° since 2007.

Let χ_m and ϕ_m represent the magnetic zenith and azimuth, respectively. A radar points along the magnetic field line when its elevation is $90^\circ - \chi_m$ and its azimuth is ϕ_m . To ensure the training data represents true field-aligned conditions, we filter the dataset to include only measurements with radar elevation $\in [76^\circ, 79^\circ]$ and azimuth $\in [184^\circ, 190^\circ]$. These ranges maximize data retention while maintaining an approximate field-aligned field-of-view. This filtering step reduces the dataset from ~650k to ~440k measurements.

Plasma Parameters

The empirical model relies on three primary plasma parameters: electron density (N_e), electron temperature (T_e), and ion temperature (T_i). To maintain dataset integrity, we analyze the prevalence of missing data. Figure A.10 displays the distribution of NaN values. The overall missing value rate is low

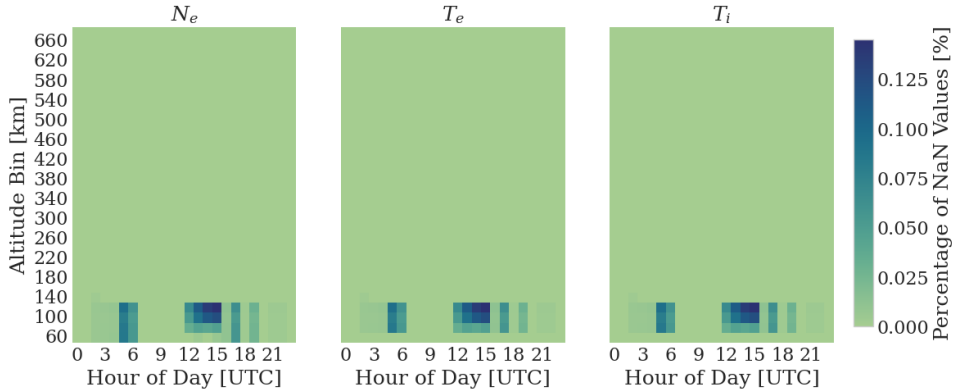


Figure A.10: Heatmap displaying the frequency of NaN values in N_e , T_e , and T_i as a function of time of day and altitude.

(~0.14%), affecting only 234 out of the ~440k unique profiles. Consequently, we employ a strict filtering policy: if any profile within a measurement contains missing values, the entire sample is discarded.

Figure A.11 presents the distributions of the valid plasma parameter profiles on both linear and logarithmic scales. The upper row displays data up to the 99th percentile to exclude extreme outliers that otherwise would distort the histograms.

We also examine the associated uncertainties (standard deviation) for these measurements, shown in Figure A.12. The uncertainty in electron density (DNE) is notably high, ranging from 10^7 to 10^{11} m^{-3} . We explore filtering based on signal quality by thresholding DNE. However, setting a threshold of 10^9 removes all profiles, and a threshold of 10^{10} retains only 18k of the ~440k profiles. Given that such aggressive filtering would leave insufficient data for training, we opt to retain the noisy profiles and rely on other approaches to noisy profile filtration.

This concludes the UHF EDA. The filtered dataset of ~440k measurements is subsequently merged with the geophysical state parameters as described in Subsection A.o.4.

A.o.2 VHF Analysis

This section provides an exploratory analysis of the VHF dataset, which is utilized primarily for case studies. The goal is to identify high-quality, continuous experimental runs suitable for evaluating the model's predictions.

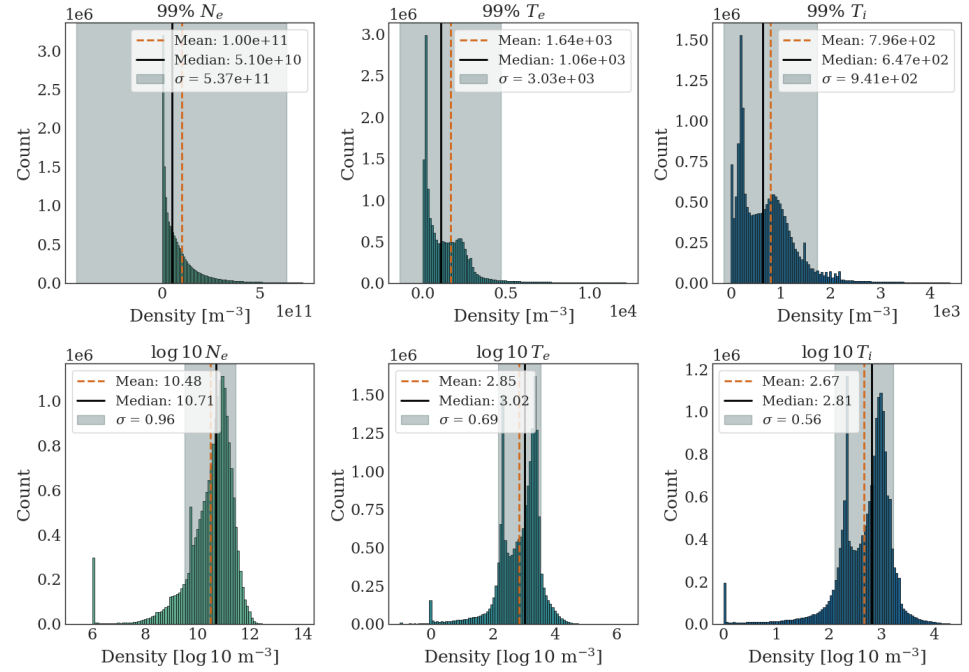


Figure A.11: Distribution of ISR parameters NE, TE and TI.

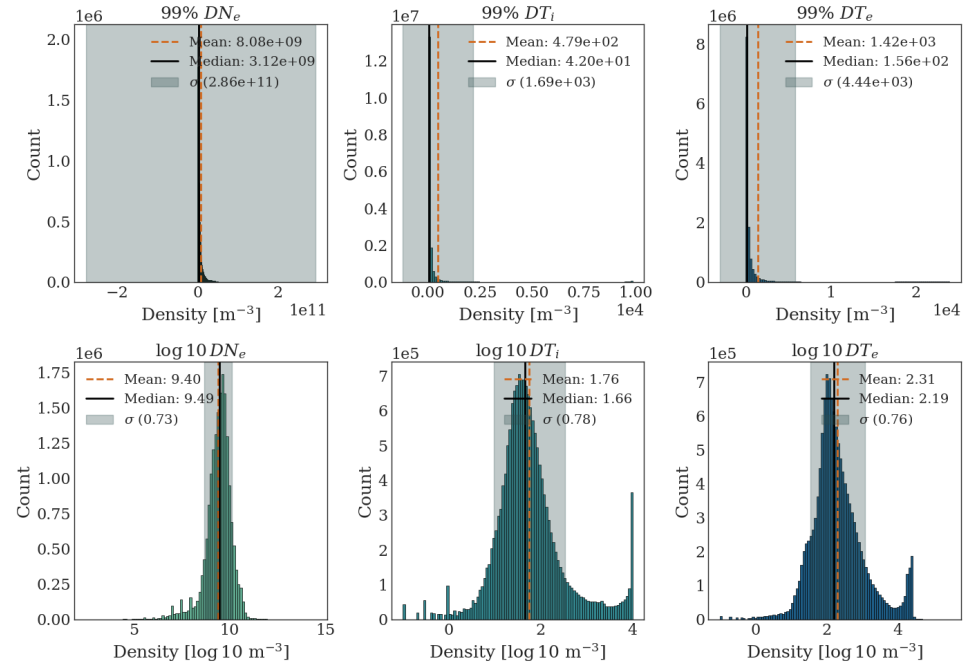


Figure A.12: Standard deviation distribution of ISR parameters NE, TE and TI.

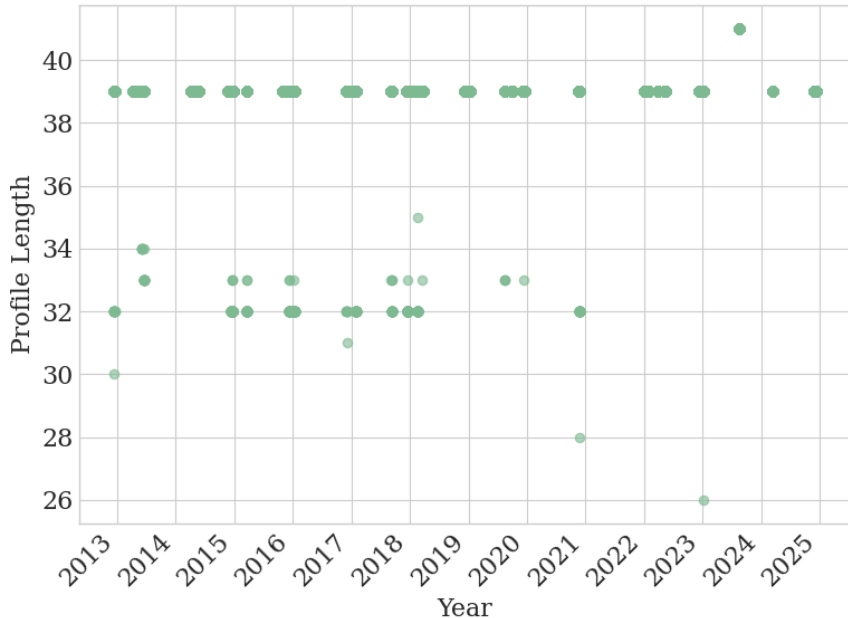


Figure A.13: Scatterplot visualizing the timeline of available VHF data and the profile length per measurement.

Figure A.13 visualizes the data availability. The VHF dataset spans approximately 11 years (starting in 2013), covering roughly one solar cycle. In contrast to the UHF dataset, profile lengths are more consistent, with a length of 39 range gates being the most common. This dominance is clearly visible in Figure A.14.

Restricting our analysis to profiles of length 39, we computed the mean and standard deviation of the altitude gates (Figure A.15). The range gates are more closely spaced at lower altitudes and spread out at higher ranges. The altitude stability is high, with standard deviations generally around 0.5 km. Notably, the highest altitude gate exhibits surprisingly low variance, contrary to the trend seen in the UHF data.

The pointing geometry is shown in Figure A.16. The dataset exclusively contains measurements directed towards geographic north (azimuth $\approx 0^\circ$) with a low elevation of 30° . This confirms that the radar beam has a substantial component perpendicular to the geomagnetic field, as intended for the case study.

Figure A.17 illustrates the occurrence of missing values for N_e , T_e , T_i , and V_{LOS} . Similar to the UHF dataset, missing values are most frequent at the lowest altitudes. However, unlike the UHF data, there is no strong diurnal pattern to the data gaps.

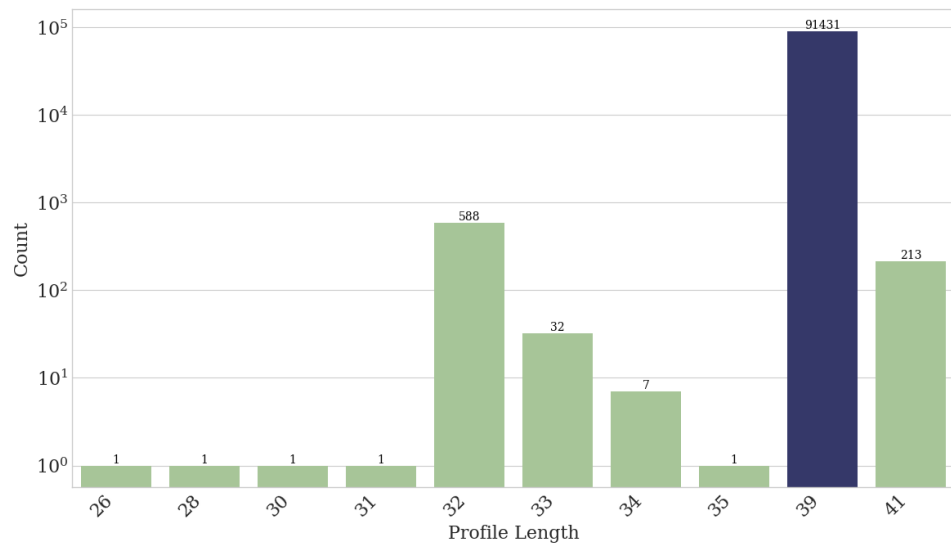


Figure A.14: Distribution of altitude counts for VHF measurements.

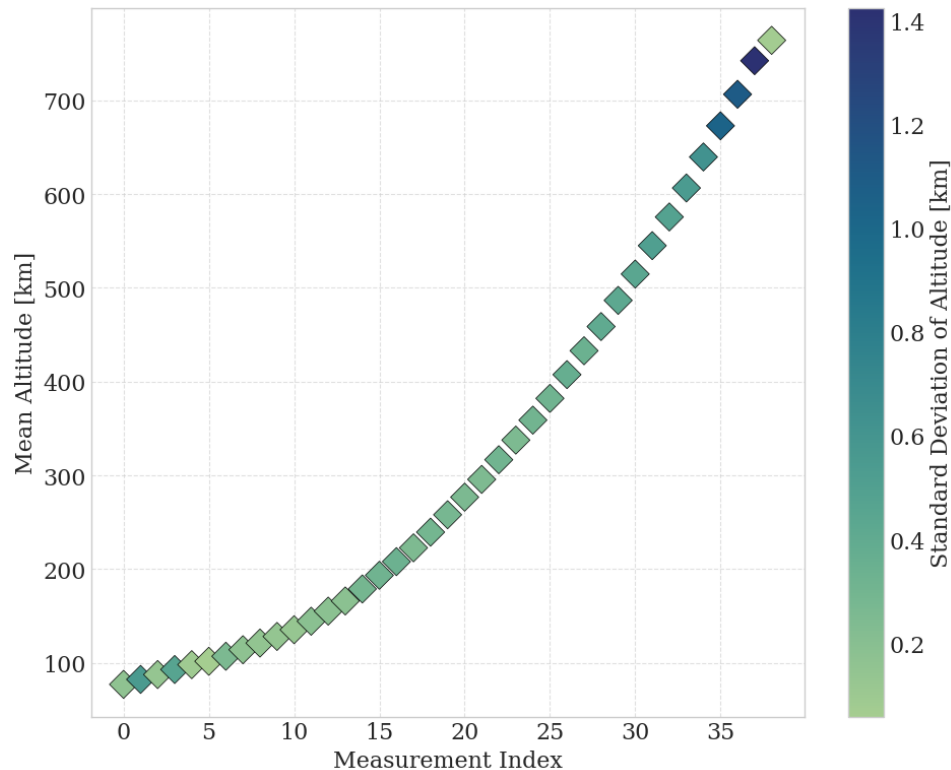


Figure A.15: Mean and standard deviation of altitude for each of the 39 range gates in the standard VHF profile.

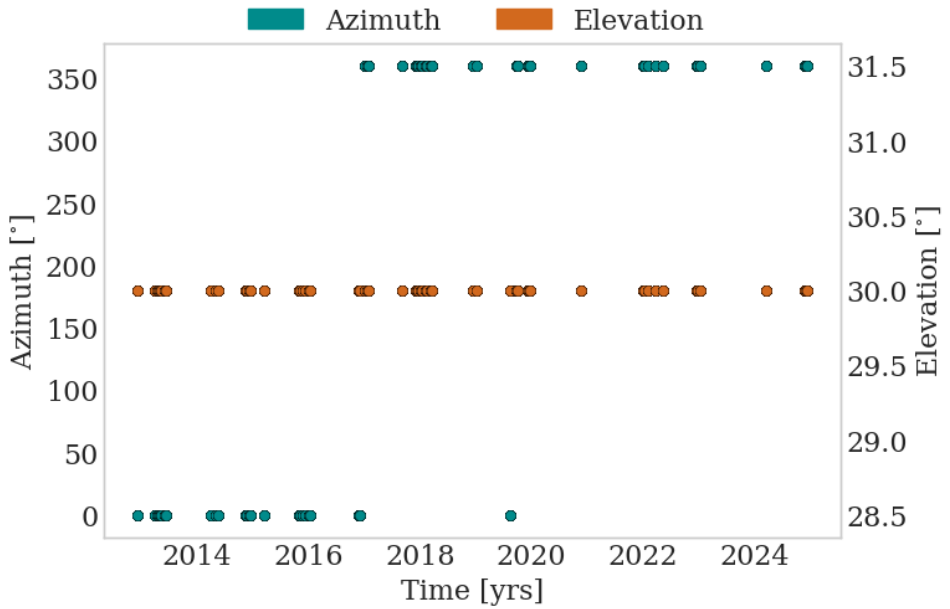


Figure A.16: Distribution of VHF radar azimuth (blue, left axis) and elevation (orange, right axis) angles.

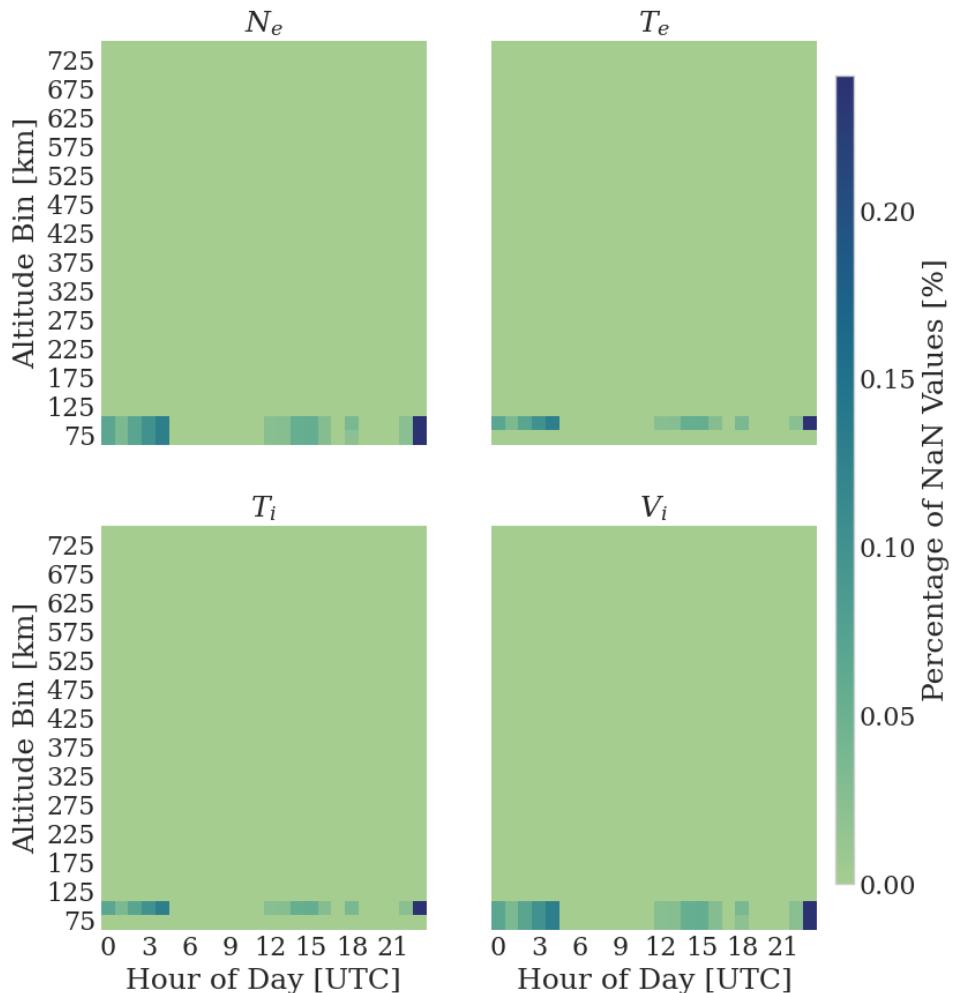


Figure A.17: Heatmap of NaN-value frequency for VHF parameters (N_e , T_e , T_i , V_{LOS}) vs. Hour of Day and Binned Altitude.

A.0.3 Geo Analysis

The study utilizes the following geophysical indices: AE, AL, SYM/H, PCN, A_p , and F10.7. The full time series for the period 2004-2024 are presented in Figure A.18.

Figure A.19 displays the statistical distributions of these parameters. The histograms indicate that most parameters are heavy-tailed, with significant outliers that compress the visual representation of the range.

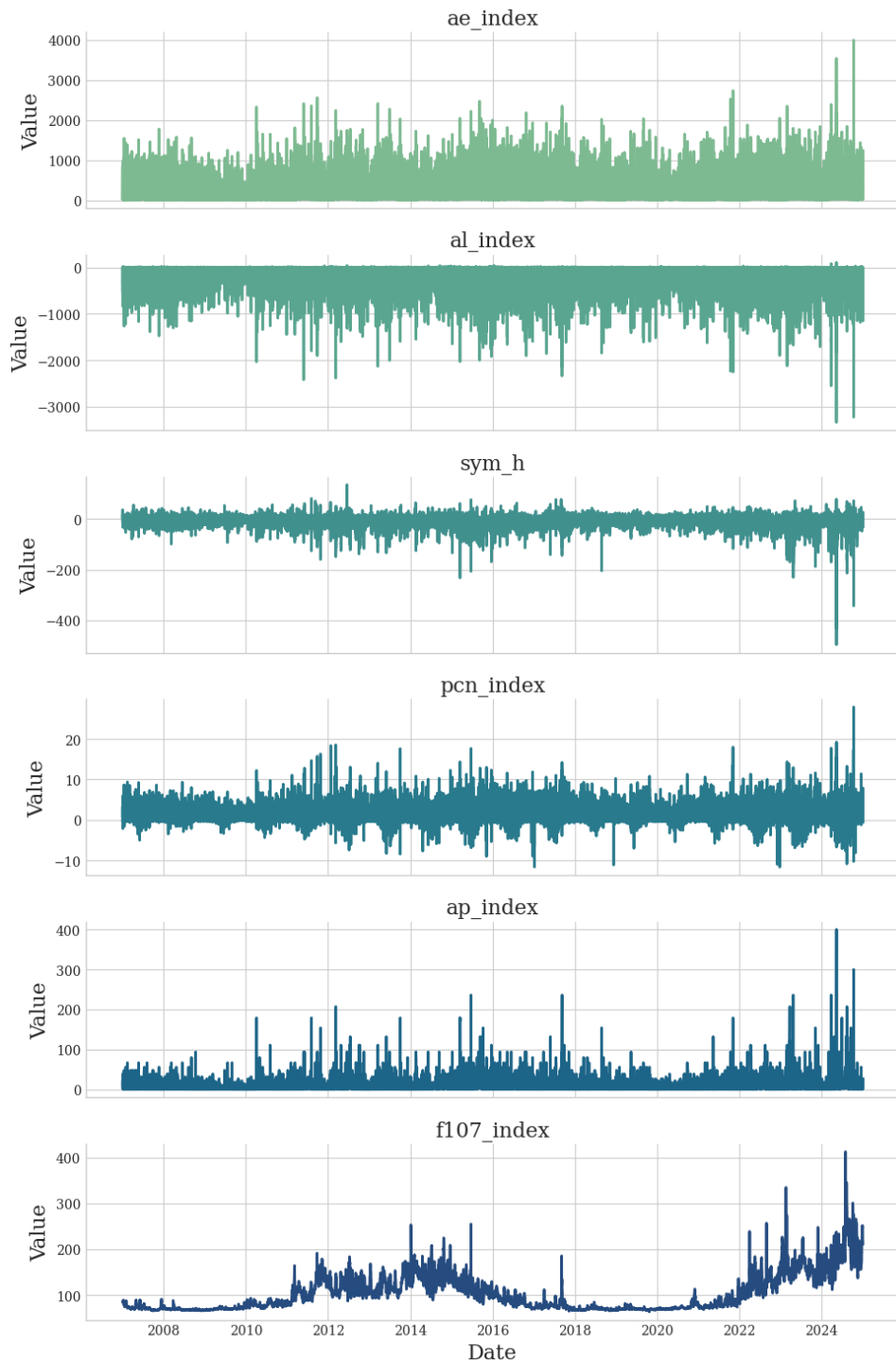


Figure A.18: Plot of the time series of the geophysical parameters. From top to bottom: AE , AL , SYM/H , PCN , A_p and $F10.7$ indices.

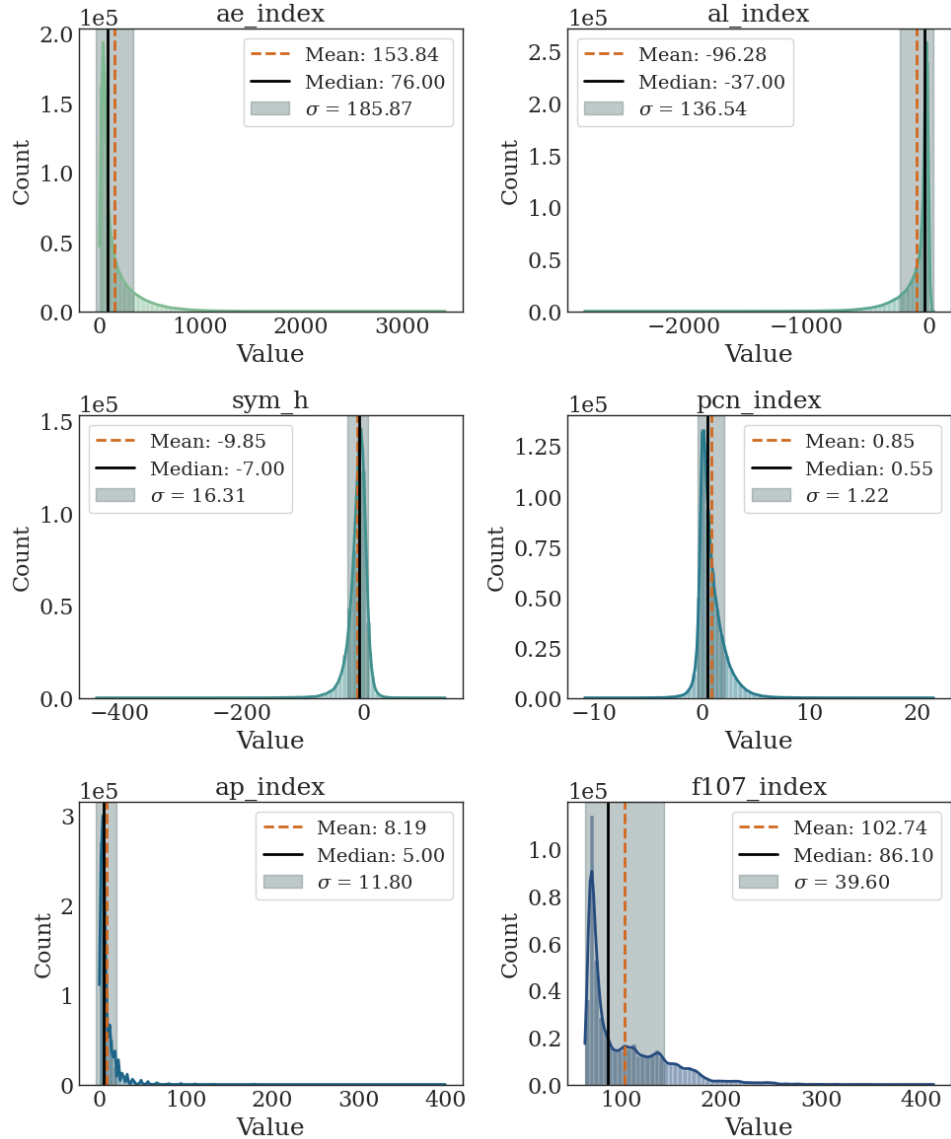


Figure A.19: Distribution of the geophysical parameters, with mean, median and standard deviation.

A.o.4 Dataset Merging

To construct the training dataset, we interpolate the geophysical state parameters onto the timestamps of the UHF dataset. In addition to the native ISR parameters (including measurement altitude), we engineer several auxiliary features to provide the network with temporal and solar context:

- Solar Zenith Angle (SZA)
- Cyclical time features: $\sin(\text{TOD})$, $\cos(\text{TOD})$, $\sin(\text{DOY})$, and $\cos(\text{DOY})$.

These features are critical for capturing the solar-driven ionization variations. The correlation matrix for the features in the UHF training set is presented in Figure A.20.

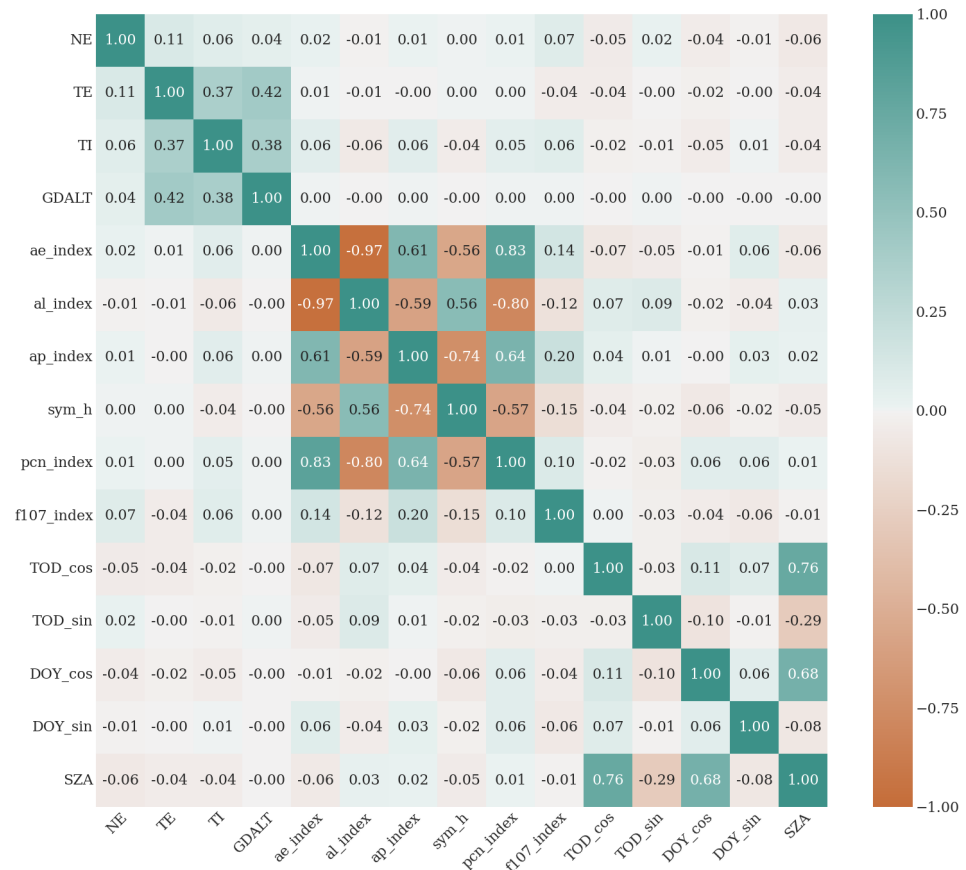


Figure A.20: Correlation heatmap of the input features in the merged dataset.

To facilitate the case studies described later in the thesis, we apply an identical merging procedure to the VHF dataset. The geophysical parameters are interpolated onto the VHF timestamps, and the same set of auxiliary features are generated. This ensures that the VHF input data is structurally identical to the UHF training data, which is a prerequisite for valid model inference.

The resulting UHF dataset serves as the input for the training pipeline, while the merged VHF dataset is reserved for the testing and application phases

described in Section 6.1.



B

Collision Frequency

Non-resonant ion-neutral collision frequency coefficients C_{in} , in units of $10^{-10} \text{ cm}^3 \text{ s}^{-1}$, for ions O^+ , O_2^+ , N_2^+ and NO^+ are found in Table B.1. Ion-neutral and electron-neutral momentum transfer collision frequencies are displayed in Table B.1 and Table B.3, respectively.

Table B.1: Ion-neutral collision frequency coefficients C_{in} , in units of $10^{-10} \text{ cm}^3 \text{ s}^{-1}$, for ions O^+ , O_2^+ , N_2^+ and NO^+ . R indicates resonant interaction. Coefficients obtained from table 4.4 in (Schunk and Nagy, 2009a).

Ion	Neutral		
	O	O_2	N_2
O^+	R	6.64	6.82
O_2^+	2.31	R	4.13
N_2^+	2.58	4.49	R
NO^+	2.44	4.27	4.34

Table B.2: Resonant ion-neutral momentum transfer collision frequencies ν_{in} for ions O^+ , O_2^+ , N_2^+ and NO^+ . Densities are in cm^{-3} . Reduced temperature $T_r = \frac{T_i+T_n}{2}$. Expressions obtained from table 4.5 in (Schunk and Nagy, 2009a).

Species	Temperature Range [K]	Expression for ν_{in} [s^{-1}]
O^+ , O	$T_r > 235$	$3.67 \times 10^{-11} n_O T_r^{\frac{1}{2}} (1 - 0.064 \log_{10} T_r)^2$
O_2^+ , O_2	$T_r > 800$	$2.59 \times 10^{-11} n_{O_2} T_r^{\frac{1}{2}} (1 - 0.073 \log_{10} T_r)^2$
N_2^+ , N_2	$T_r > 170$	$5.14 \times 10^{-11} n_{N_2} T_r^{\frac{1}{2}} (1 - 0.069 \log_{10} T_r)^2$

Table B.3: Momentum transfer collision frequencies ν_{en} for electron-neutral interactions. Densities are in cm^{-3} . Expressions obtained from table 4.6 in (Schunk and Nagy, 2009a).

Species	Expression for ν_{en} [s^{-1}]
O	$8.9 \times 10^{-11} n_O (1 + 5.7 \times 10^{-4} T_e) T_e^{\frac{1}{2}}$
O_2	$1.82 \times 10^{-10} n_{O_2} (1 + 3.6 \times 10^{-2} T_e^{\frac{1}{2}}) T_e^{\frac{1}{2}}$
N_2	$2.33 \times 10^{-11} n_{N_2} (1 + 1.21 \times 10^{-4} T_e) T_e$

